Cathodoluminescence plasmon microscopy

Ph.D. Thesis Utrecht University, March 2009
Cathodoluminescence plasmon microscopy
Martin Kuttge

ISBN 978-90-77209-32-5

A digital version of this thesis can be downloaded from http://www.amolf.nl.

Cathodoluminescence plasmon microscopy

Kathodeluminescentie plasmon microscopie
(met een samenvatting in het Nederlands)

Proefschrift

ter verkrijging van de graad van doctor aan de Universiteit Utrecht
op gezag van de rector magnificus, prof.dr. J.C. Stoof,
ingevolge het besluit van het college voor promoties
in het openbaar te verdedigen
op woensdag 25 maart 2009 des middags te 4.15 uur

door

Martin Kuttge

geboren op 27 oktober 1978 te Hamm (Duitsland)

Promotoren: Prof. dr. A. Polman
Prof. dr. F. J. García de Abajo

This work is part of the research programme of the 'Stichting voor Fundamenteel Onderzoek der Materie (FOM)', which is financially supported by the 'Nederlandse Organisatie voor Wetenschappelijk Onderzoek (NWO)'.

Contents

1 Introduction

1.1 Surface plasmon polaritons

Surface plasmon polaritons (SPPs) are electromagnetic waves that are strongly coupled to the collective oscillation of free electrons at an interface between a dielectric and a metal [1]. They are transverse magnetic wave solutions of Maxwell's equations that propagate along the metal/dielectric interface and decay evanescently perpendicular to the interface into the metal and the dielectric (see inset Fig. 1.1). The decay length into the metal is comparable to the skin depth, while the decay into the dielectric is on the order of 100 nm in the visible. Therefore, the electromagnetic energy of SPPs is strongly localized in the vicinity to the surface, allowing the confinement of optical waves to the nanoscale.

The strong coupling between the conduction electrons and the electromagnetic wave leads to a dispersion relation that differs from that for light in a dielectric. For a single interface between a metal and a dielectric the dispersion relation can be derived from Maxwell's equations and boundary conditions.

$$k_{SPP}(\omega) = k_0 \sqrt{\frac{\epsilon_d(\omega)\epsilon_m(\omega)}{\epsilon_d(\omega) + \epsilon_m(\omega)}}, \tag{1.1}$$

with $\epsilon_m(\omega)$ and $\epsilon_d(\omega)$ being the permittivity of the metal and the dielectric, respectively. The dispersion relation for SPPs propagating at the interface between a Drude metal and a dielectric is shown in Fig. 1.1 together with the dispersion of light in the dielectric ("light line"). Since metals have a negative permittivity ($\epsilon_m < 0$) in the visible wavelength range, the SPP wavevector is larger than for light in the dielectric ($\epsilon_d > 0$) and the dispersion relation lies right to the light line. For low frequencies SPPs have a very photon-like character and the dispersion relation lies close to the light line. For higher frequencies, the SPP dispersion deviates further

from the light line towards larger wavevectors and shorter SPP wavelengths. The largest wavevectors are found at the surface plasmon resonance ω_{SPP} which for a Drude metal is located at $\omega_{SPP} = \omega_p/\sqrt{1+\epsilon_d}$ with ω_p the plasmon resonance. For noble metals the surface plasmon resonance lies in the visible. The dependence of the SPP dispersion on the permittivity of the dielectric allows effective engineering of the dispersion relation.

As is clear from the dispersion relation, the SPP wavevector is always larger than that for light in the dielectric. To excite SPPs by light a coupling technique is required that provides the wavevector mismatch. Coupling using a subwavelength scatterer or a periodic grating are commonly used techniques to provide the additional momentum [1]. Attenuated total reflection to couple evanescent field components to SPPs is also being used [2, 3]. A less popular but very interesting method to excite SPPs is by electron irradiation [4, 5], which is the topic of this thesis.

The large tunability of the dispersion that can be achieved with SPPs comes at the price of higher propagation loss. As part of the SPP field propagates in the metal, it is attenuated by Ohmic losses in the metal, an effect that is largest for wavelengths close to the surface plasmon resonance. The propagation length is given by

$$L_{SPP} = \frac{1}{2\mathrm{I}m(k_{SPP})}. \tag{1.2}$$

For noble metals SPPs can propagate in the order of 100 μm in the near-infrared, but close to the SPP resonance L_{SPP} decreases to values as short as 100 nm [6].

1.2 Plasmonics - opportunities and challenges

The possibility to confine light to the nanoscale and the ability to tune the dispersion relation of light has raised large interest and led to rapid growth of the field of plasmonic research. The parallel development of nanoscale fabrication techniques like electron beam lithography or focused ion beam milling, has opened up new ways to structure metals surfaces and control SPP propagation and dispersion at the nanoscale.

The large field enhancement of SPPs localized at the metal surface makes SPPs very sensitive to changes in the permittivity of the adjacent dielectric. By functionalizing the metal surface, biological molecules or chemicals can be selectively bound to the surface, shifting the wavelength of the SPP resonance [7, 8, 9]. Research in this field is far advanced and sensors relying on the effect of the surface plasmon resonance shift are commercially available.

Similarly, SPPs can be used to efficiently couple sunlight into waveguide modes of thin semiconductor layers. The strong field enhancement and guiding properties of SPPs increase in this case the light absorption and thereby the efficiency of thin-film semiconductor solar cells [10].

As the SPP wavelength for a given energy is shorter than in the dielectric, SPPs can be employed to overcome the classical diffraction limit and to shrink optical

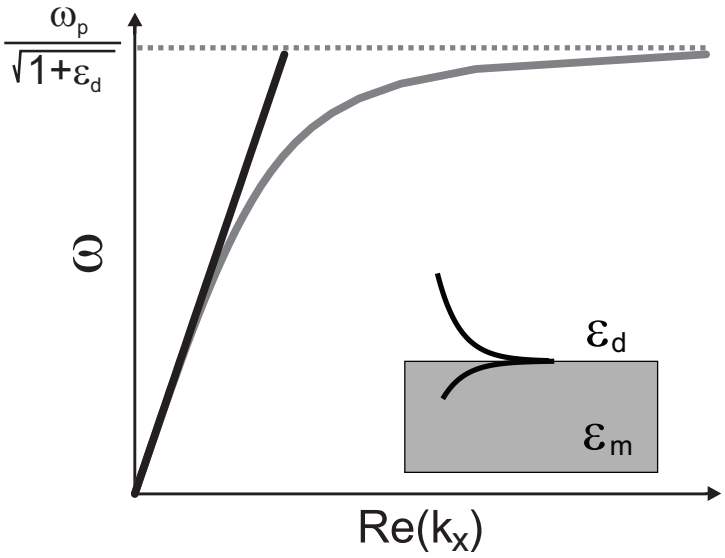

Figure 1.1: *Dispersion relation for surface plasmon polaritons propagating at the interface between a dielectric and a Drude metal. The light line in vacuum is drawn in black. Inset: Schematic of the electric field intensity associated to a SPP propagating at the interface between a dielectric and a metal.*

integrated circuits. Several studies have shown guiding of SPPs in thin metal stripe waveguides [11] or grooves in metal surfaces [12] and the first optical circuits have been demonstrated [13]. By structuring metal stripe waveguides the propagation speed of SPPs can be reduced well below the speed of light [14]. Tapering of planar waveguides allows the concentration of SPPs to hot spots with length scales of only a fraction of the SPP wavelength [15, 16].

While metal stripe geometries allow efficient guiding of SPPs, the SPP field around such waveguides extends far into the dielectric. Metal-insulator-metal (MIM) geometries, in which SPPs propagating on the two interfaces are coupled, allow confinement of the SPP field to the thin dielectric gap between the metal layers. The strong interaction of the two coupled SPP waves allows further design of the dispersion relation. By reducing the size of the dielectric layer extremely short wavelengths can be achieved at optical frequencies. Indeed, MIM plasmons with wavelengths as short as 58 nm have been demonstrated at optical frequencies [17]. For certain geometries MIM waveguides exhibit a negative refractive index for the guided plasmons. Two-dimensional negative refraction of plasmons has been demonstrated in the visible [18], and was also confirmed theoretically [19].

Despite these advances in the field of plasmonics, several important open questions

and problems remain. For example: how can plasmons be efficiently excited with nanoscale resolution? So far, the excitation of SPPs is mostly performed using far-field optical techniques which have a resolution that is larger than plasmonic phenomena under investigation. However, for true nanoscale plasmonic studies a SPP point source with nanoscale dimensions is required. Another important question is: what are the fundamental processes that determine the losses of SPPs? Practical plasmon experiments are performed on poly-crystalline surfaces, and the limits to the losses due to e.g. surface roughness and grain boundaries are not known.

To manipulate SPPs on a surface, reflectors are needed. So far, macroscopic Bragg reflectors structured into the surface have been used. For true nanoscale integration, nanoscale SPP mirrors are required and a question is, how these can be made. Once these are realized, nanoscale cavities to confine SPPs can also be designed. The limits to the plasmonic cavity mode volumes and quality factor are not yet known.

And finally, the use of a particle beam rather than a light beam to excite SPP raises questions and novel opportunities regarding the selectivity with which surface plasmon modes with different symmetry can be excited.

1.3 Outline of this thesis

This thesis focuses on acquiring fundamental understanding of the generation and confinement of SPPs using electron beam irradiation.

- In chapter 2, we give an introduction into cathodoluminescence spectroscopy and describe the measurement setup that we are using. We present the derivation of the generation rates for transition radiation and SPPs that are used in the analysis of the following chapters and compare these to experiments. Chapter 2 also contains a short description of the two-dimensional boundary-element-method that is used to calculate the electromagnetic fields arising from the electron impact. We describe the basic concepts used and how they are numerically implemented.

- An electron beam impinging onto a gold surface coherently generates transition radiation and surface plasmon polaritons which interfere in the far-field. The interference leads to oscillations of the CL intensity in front of a grating as is observed in measurements that are presented in chapter 3. We show that we can model our measurements using the analytical generation rates derived in chapter 2. Further modeling allows us to establish a connection between the measured CL signal and the local density of states for SPPs.

- In chapter 4, we present measurement of the propagation length of SPPs on gold surfaces. The observed losses are higher than expected for Ohmic losses solely and depend strongly on the grain characteristics of the gold interfaces. By comparing different gold films grain boundary scattering is identified as an important loss factor for plasmon propagation.

- Chapter 5 describes how we can use grooves structured into a gold surface to confine SPPs. We show CL measurements of the mode structure between two parallel grooves that act as Fabry-Perot resonators. We determine the quality factor of those cavities, which shows a maximum for a certain groove depth. We present finite-difference time domain (FDTD) calculations for the reflectivity that confirm our measurement results.

- In chapter 6, we present numerical results for the SPP reflectivity of single linear grooves. We use FDTD and a boundary-element-method (BEM) to determine the reflectivity and investigate the near field of grooves with varying geometrical parameters. We show that single grooves have resonances of high reflectivity, which can be attributed to the coupling of propagating SPPs to resonant localized groove modes.

- Chapter 7 presents CL measurements of SPPs confined to boxes bounded by grooves in a gold surface. Two-dimensional standing SPP modes are observed in those boxes. We model the measurements with a two-dimensional image source model.

- In chapter 8, we present results on the excitation of metal-insulator-metal plasmons in a $Ag/SiO_2/Ag$ structure with cathodoluminescence. We use resonator structures to determine the MIM plasmon wavelengths which we find to be as short as 227 nm. Measurements of MIM disk resonators show modes with mode volumes as small as $0.04\lambda^3$. The dependence of the excitation probability of MIM modes due to phase retardation effects resulting from the finite electron velocity is discussed.

This thesis gives an overview of the opportunities that cathodoluminescence imaging spectroscopy provides for the field of plasmonics. The presented results show that an electron beam can be used as a point source for SPPs to study basic plasmonic properties in a quantitative manner. Our work provides insight in the physical mechanisms determining excitation, propagation, reflection and confinement of surface plasmon polaritons. These insights can lead to novel applications of surface plasmons in (bio-)sensing, nanoscale optical integrated circuits, opto-electronic integration and photovoltaics.

2

Cathodoluminescence

In this chapter we introduce the different sources of cathodoluminescence (CL). We present the theoretical derivation of the CL emission probability for an electron crossing the interface between two media. We calculate the emission probabilities for surface plasmon polaritons and transition radiation. A description of the experimental setup as well as some basic measurements will be presented.

2.1 Introduction

Cathodoluminescence (CL) was first discovered in the mid-nineteenth century as the light emission stemming from cathode electron rays hitting a glass substrate. The CL spectra are very material specific, and CL is now routinely used as a material characterization technique in mineralogy, semiconductor physics, and many other fields. CL found extensive application as the emission source in cathode-ray-tube computer monitors and televisions.

The main direct emission processes involved in CL are Cherenkov radiation and transition radiation. Both of them are coherent with the external field of the incoming electron as their fields are described by the same set of Maxwell's equations. The generation of surface plasmon polaritons can be considered as an indirect emission process, but also falls into the group of coherent emission. As we will see later, the coherence between the different radiation sources can result in interference detected in the far-field.

Incoherent emission is generally associated with the highly localized creation of electron-hole pairs which subsequently recombine and emit radiation. In metals electronic relaxation channels are much faster than radiative recombination, so that incoherent radiation is only a minor contribution to CL.

A charged particle like an electron passing through a transparent medium will emit Cherenkov radiation if its speed v is faster than the phase velocity of light in that medium, i.e. $v > c/n$ where n is the refractive index of the medium. This effect is *e.g.* the source of the blue glow in the water coolant bath of nuclear reactors and is commonly used in particle physics to detect and trace charged particles [20]. Cherenkov radiation is mainly observed in dielectrics and not in metals, and will not be considered in the context of this thesis.

Transition radiation is emitted if a charged particle passes through a boundary between two media with different dielectric constants. It is created by the time dependent variation and eventual collapse of the dipole moment formed by the incident electron and its image charge in the dielectric. This effect was first predicted by Ginzburg and Frank [21] and observed by Goldsmith and Jelly [22] for metals. It is employed in crystallography to identify and characterize materials [23].

For metals bombarded with electron beams the excitation of bulk or surface plasmons can occur when the moving charge couples to the free electrons in the metal. This effect was observed first in electron energy loss spectroscopy and provided a first proof of the excitation of bulk and surface plasmons [4]. First observations of light emission from SPPs, excited by electrons and coupled out using gratings, were done by Teng and Stern [24]. Heitmann used electron excitation of SPPs to map their dispersion relation on silver gratings [5]. Yamamoto *et al.* first reported the use of electron irradiation to determine the spatially-resolved mode distribution of plasmons localized in silver nanoparticles [25]. More recently, the imaging of localized SPP modes in Au nanowires using electron irradiation was demonstrated [26] and the propagation and scattering of SPPs on metal surfaces have recently been directly resolved [6, 27, 28].

In this chapter we will derive the excitation probabilitiy for emission for an electron passing through the boundary between a metal and a dielectric from Maxwell's equations. We will focus on surface plasmon generation and transition generation as these are the most important contributions in the context of this thesis. The results of these derivation will be discussed. We will describe the used experimental setup and present initial measurements, that are compared to theoretical results.

2.2 Theory

An electron in uniform motion in a straight line in free space does not emit radiation. If the electron is incident from vacuum onto the boundary of a material it perturbs the electrons in the uppermost layers due to its external field and creates a polarization charge. This charge together with the incoming electron can be considered as an effective dipole. In case of a metal substrate the dipole can decay into two channels: direct emission into the far field (transition radiation) and generation of surface plasmons.

2.2.1 Transition radiation

The first predictions of transition radiation date from a paper by Ginzburg and Frank [21] and more detailed studies were done by Ter-Mikaelian [29]. We will follow a derivation which can be found in textbooks [30, 31].

We consider an electron, with charge $-e$ and constant velocity v along the z-axis. The electron is incident from the lower half space $z < 0$ taken to be vacuum ($\epsilon_1 = 1$) and crosses the interface with the upper half space filled with a dielectric of permittivity $\epsilon_2 = \epsilon$ at $z = 0$ and time $t = 0$. The dielectric can be either a metal ($Re(\epsilon) < 0$) or dielectric ($Re(\epsilon) > 0$). The electromagnetic fields $\mathbf{E}(\mathbf{r},t)$ and $\mathbf{H}(\mathbf{r},t)$ in each medium j satisfy Maxwell's equations:

$$\nabla \cdot \mathbf{H} = 0\,, \tag{2.1}$$

$$\nabla \times \mathbf{E} = -\frac{1}{c}\frac{\partial \mathbf{H}}{\partial t}\,, \tag{2.2}$$

$$\nabla \cdot \epsilon_j \mathbf{E} = 4\pi\rho\,, \tag{2.3}$$

$$\nabla \times \mathbf{H} = -\frac{1}{c}\frac{\epsilon_j \partial \mathbf{E}}{\partial t} + \frac{4\pi}{c}\mathbf{j}\,, \tag{2.4}$$

with c the speed of light and ρ and $\mathbf{j}$ the charge and current density associated with the moving electron. More precisely,

$$\rho(z,t) = -e\delta(z - vt)\,, \tag{2.5}$$

$$\mathbf{j}(z,t) = -e\mathbf{v}\delta(z - vt)\,. \tag{2.6}$$

The solution of Maxwell's equations for this problem can be most readily found in the frequency and momentum domain. Therefore, we Fourier transform the electric

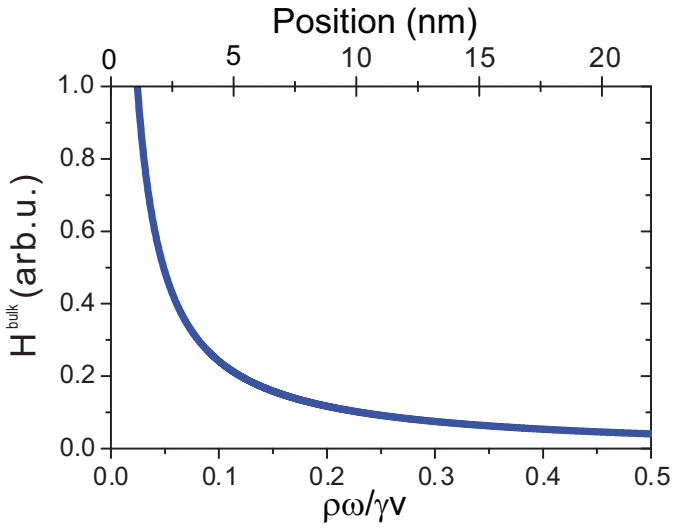

Figure 2.1: *External magnetic field* $\mathbf{H}^{bulk}$ *from Eqn. 2.11 as a function of radial distance from the electron trajectory. The top horizontal axis plots the corresponding positions for 30 keV electrons and a wavelength of 800 nm.*

and magnetic fields $\mathbf{E}(\mathbf{r},t)$ and $\mathbf{H}(\mathbf{r},t)$:

$$\mathbf{H}(\mathbf{r},t) = \frac{1}{(2\pi)^4}\int d\omega e^{-i\omega t}\int d^3\mathbf{q}\,\mathbf{H}(\mathbf{q},z,\omega)e^{i\mathbf{q}\cdot\mathbf{r}}\,. \tag{2.7}$$

The Fourier transforms of the source distributions can be readily found to be:

$$\rho(\mathbf{k},\omega) = -\frac{e}{2\pi}\delta(\omega-\mathbf{k}\cdot\mathbf{v})\,, \tag{2.8}$$

$$j(\mathbf{k},\omega) = \mathbf{v}\rho(\mathbf{k},\omega)\,. \tag{2.9}$$

We decompose the fields $\mathbf{H}$ in each region into a part describing the field in a bulk medium $\mathbf{H}_j^{bulk}$ and the induced field $\mathbf{H}_j^{ind}$ that is used to match the boundary conditions at the interfaces. The bulk part can be found solving Maxwell's equations for an homogeneous medium of permittivity ϵ_j:

$$\mathbf{H}_j^{bulk}(Q,z,\omega) = \frac{4\pi ieQ}{c}e^{i\omega z/v}\frac{\hat{\mathbf{t}}}{k_j^2-q^2}\,, \tag{2.10}$$

$j=1,2$ referring to vacuum and the metal, respectively, k_j is the wave vector in each medium, $\hat{\mathbf{t}}=\hat{\mathbf{z}}\times\hat{\mathbf{Q}}$, and $\mathbf{Q}$ is the in-plane momentum vector obtained after integration of the z-component of the momentum leading to $\mathbf{q}=(\mathbf{Q},\omega/v)$.

Performing the **q**-integral in Eqn. 2.7 and transforming the fields into real space, we find for the field of the moving electron

$$\mathbf{H}_j^{bulk}(\mathbf{r},\omega) = -\frac{2e\omega}{vc\gamma} e^{i\omega z/v} K_1\left(\frac{\omega\rho}{\gamma v}\right)\hat{\phi}\,, \tag{2.11}$$

where ρ is the distance from the electron trajectory, $\gamma = 1/\sqrt{1-v^2/c^2}$ is the Lorentz contraction factor, where $\hat{\phi}$ is the azimuthal unit vector, and K_1 is the modified Bessel-function of the second kind . We see that the moving electron acts as a broadband source of electromagnetic field with the frequency components of the field moving with velocity v along the electron trajectory. The field decays away from the electron trajectory with the Bessel function with its argument inversely proportional to the velocity v.

Interestingly, the external field of the electron (Eqn. 2.11) diverges at the position of the trajectory (see Fig. 2.1), resulting in a theoretically infinite resolution. This means that the actual resolution of experiments is only limited by the finite size of the beam spot. In practice, the delocalized character of the material response must be also considered: an upper limit of the resolution is given by the distance of exponential decay ($v\gamma/2\omega$) of the K_1 function in the external field intensity. For example, $v\gamma/2\omega =$ 13 nm for 30 keV electrons and excitations of wavelength $\lambda = 800$ nm.

When the electron approaches an interface it can induce a polarization charge which in turn generates an induced field given by:

$$\mathbf{H}_j^{ind}(Q,z,\omega) \;=\; 2\pi e k_j s_j e^{ik_{zj}|z|}\alpha_j \hat{\mathbf{t}}\,, \tag{2.12}$$

where $k_{zj} = \sqrt{k_j^2 - Q^2}$, $s_1 = -1$, $s_2 = 1$, and α_j are boundary coefficients that are determined by applying the boundary conditions for the electromagnetic field at the interface $z = 0$. The continuity of the parallel component of the electric and magnetic fields leads to a set of linear equations which can be solved for the coefficients, resulting in

$$\alpha_1(Q) \;=\; \frac{2Qi/c}{k_{z1}\epsilon_2 + k_{z2}\epsilon_1}\left[\frac{-\omega/v\epsilon_2 + k_{z2}\epsilon_1}{q^2-k_1^2} - \frac{-\omega/v\epsilon_1 + k_{z2}\epsilon_1}{q^2-k_2^2}\right], \tag{2.13}$$

$$\alpha_2(Q) \;=\; \frac{2Qi/c}{k_{z1}\epsilon_2 + k_{z2}\epsilon_1}\left[\frac{\omega/v\epsilon_2 + k_{z1}\epsilon_2}{q^2-k_1^2} - \frac{\omega/v\epsilon_1 + k_{z1}\epsilon_2}{q^2-k_2^2}\right]. \tag{2.14}$$

To obtain the induced field at the interface we insert these coefficients into Eqn. 2.7 and perform the integral. The fields are azimuthally symmetric so we can integrate over the azimuthal angle of **Q**

$$\mathbf{H}_1^{ind}(\mathbf{r},\omega) = -i\hat{\phi} e s_j \int_0^\infty Q dQ \alpha_j e^{ik_{zi}|z|} J_1(QR)\,, \tag{2.15}$$

R is the radial distance from the electron trajectory, and J_1 is the first order Bessel function.

In our experiment we observe the CL signal in the far field, far away from the actual impact position of the electron. As apparent from Eqn. 2.11 the field directly emitted by the moving electron decays exponentially away from the electron trajectory as K_1. The CL emission observed in the far-field must thus arise from the induced fields at the boundary. Therefore, we perform an asymptotic analysis for $r \to \infty$ for the induced field (Eqn. 2.12) to obtain the far-field, which we write as $\mathbf{H}_{ind} \to \mathbf{f}(\theta, \omega)e^{ikr}/r$, with $f(\theta, \omega)$ the emission amplitude

$$\mathbf{f}(\theta, \omega) = -ike\alpha_1(k \sin\theta) \cos\theta \hat{\phi}\,, \tag{2.16}$$

with θ the zenith angle with respect to the surface normal. To obtain the emission probability $P(\omega)$ as a function of frequency, we calculate the emission intensity I which is related to $P(\omega)$ by $I = \int_0^\infty d\omega P(\omega)$. The intensity I equals the flux of the Poynting-vector $S = E \times H^*$ integrated over the vacuum hemisphere. Inserting the results for the electromagnetic fields leads us to an expression for the transition radiation intensity P_{TR} which we will use in the following chapters.

$$P_{TR}(\omega) = \frac{1}{\hbar k} \int_{\pi/2}^{0} d\theta |\mathbf{f}(\theta, \omega)|^2\,. \tag{2.17}$$

2.2.2 Surface plasmons

In the previous section we derived the solutions of Maxwell's equations for transition radiation. An electron incident onto a metal surface also excites SPPs. We can derive the plasmon generation rate from the results of the previous section. The wave vector condition describing SPPs can be identified as the pole of the boundary coefficients α_j (Eqs. 2.13 and 2.14) corresponding to the SPP dispersion relation:

$$k_{z1}\epsilon_2 + k_{z2}\epsilon_1 = 0 \tag{2.18}$$

Note, that Eqn. 2.18 implies directly the commonly know form of the SPP dispersion relation Eqn. 1.1 [1]. A Taylor expansion of Eqn. 2.18 to first order around the plasmon wave vector Q_p allows us to determine the fields by avoiding the plasmon pole [32]. The integration of the wave vector in the complex plane is determined by the contribution of the pole (Cauchy's integral theorem). By separating the Bessel function into Hankel functions $J_1 = 1/2(H_1^{(1)} + H_1^{(2)})$ we can determine the electromagnetic fields of the plasmons.

$$\mathbf{H}_j^{ind}(\omega) = \pi e Q_p A_j e^{-ik_{zi}|z|} H_1^{(1)}(Q_p R)\hat{\phi}\,, \tag{2.19}$$

with $\alpha_j = A_j/(Q - Q_p)$ and assuming for the imaginary part of the wave vector $\mathrm{Im}Q_p > 0$. As in the case of transition radiation the plasmon emission probability can be calculated from the flux of the Poynting vector over a surface. In the case for plasmons we have to consider both contributions $j = 1, 2$ into the air and into the

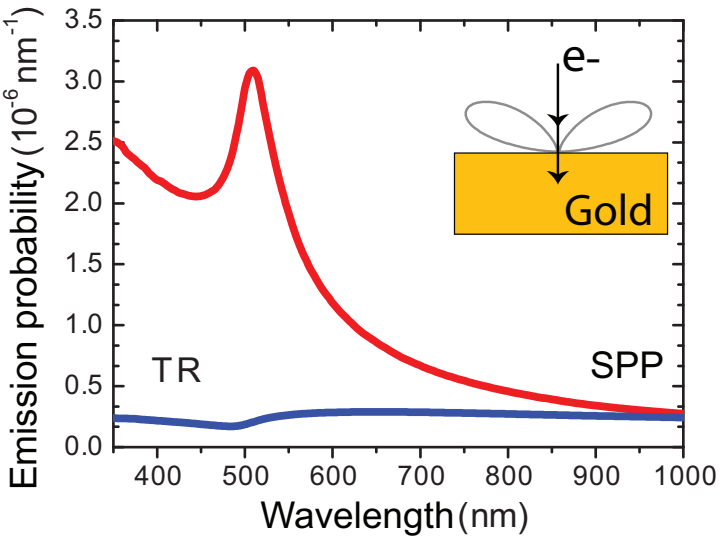

Figure 2.2: *Generation rate of transition radiation (blue) and surface plasmons (red) as a function of wavelength per incoming electron. The rates are calculated for 30 keV electrons incident on a gold surface. Inset: Angular distribution of transition radiation with a wavelength of 700 nm for an incoming 30 keV electron.*

metal as SPP fields extend to both sides of the interface. As a result we obtain the excitation probability for SPPs by the electron:

$$P_{SPP}(\omega) = \sum_j \frac{|A_j|^2 e^2}{2\hbar k^2 \mathrm{Im}(k_{zi})} e^{-2\mathrm{Im}(Q)R} \mathrm{Re}\left(\frac{Q|Q|}{\epsilon_j}\right) . \tag{2.20}$$

2.2.3 Discussion

Using equations 2.17 and 2.20 we can calculate the emission probability for transition radiation and surface plasmons, respectively. In Fig. 2.2 we show the excitation probability as a function of wavelength for 30 keV electrons incident onto a gold surface, experimental conditions similar to those in the following chapters. The transition radiation was integrated over the full upper half space.

The emission rate for transition radiation increases with wavelength but stays below the plasmon generation rate over the observed wavelength range. The generation rate of surface plasmons increases for shorter wavelengths and shows a strong maximum close to the plasmon resonance around 520 nm. Integrating over the wavelength range of 500-1000 nm approximately 0.005 transition radiation photons and 0.002 plasmons are produced per incident electron.

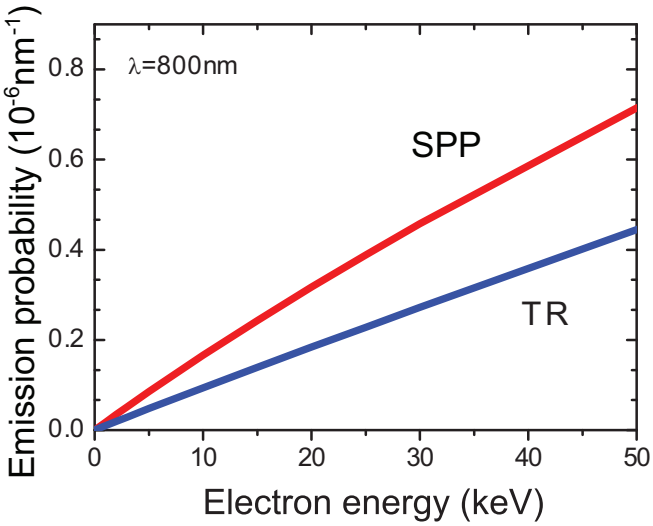

Figure 2.3: *Generation rate of transition radiation(blue) and surface plasmons (red) as a function of electron energy. The rates are calculated for a wavelength of 800 nm for electrons incident from vacuum onto a gold surface.*

Note that these spectra show only the excitation rate. The measured emission will differ and depend on the efficiency of collection and detection system. Since the bound SPPs have to be coupled to light to be detected, the SPP related emission will also depend strongly on the scattering coefficients of the coupling structures.

The inset of Fig. 2.2 shows the angular distribution of the emission rate for transition radiation at a wavelength of 700 nm. The observed emission pattern resembles that of a classical dipole placed infinitesimally close to a planar metal surface. The shape of the pattern can be understood from the transition radiation amplitude $\mathbf{f}$ (Eqn. 2.16) which has an angular dependence of $\sin\theta\cos\theta$.

In Fig.2.3 we show the emission rate for TR and SPPs as a function of electron energy for a free-space wavelength of 800 nm. Both contributions increase with electron energy. As we have seen in the previous section, the external field for an electron (Eqn. 2.11) extends further for higher electron energies. Therefore, the coupling to the material is increased, leading to a larger polarization charge and stronger emission in response.

2.3 Cathodoluminescence imaging spectroscopy

Cathodoluminescence measurements rely on the detection of radiation that is emitted as a sample is bombarded by an electron beam. To perform spectroscopy the emitted

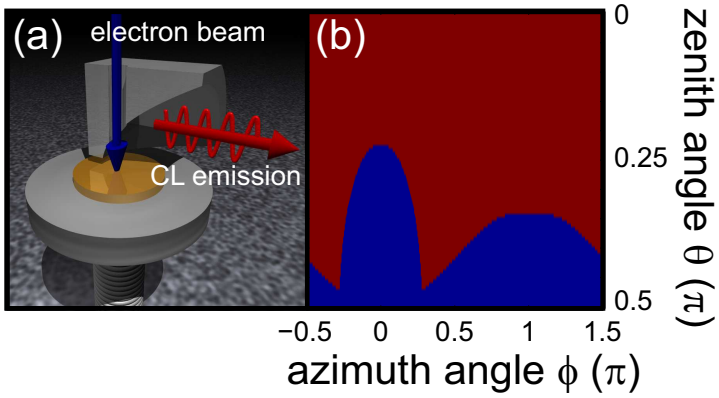

Figure 2.4: *(a) Schematic of the CL mirror position above the sample. Distances and sizes are to scale. (b) Acceptance of the CL mirror as a function of azimuth and zenith angle. The red area is within, the blue area outside the acceptance angles.*

radiation has to be spectrally resolved. Imaging requires the possibility to spatially resolve the position where the emission originates. Contrary to many commonly used spectroscopic techniques, in CL the spatial resolution is determined by the excitation source and not the detection.

For excitation we use the focused electron beam of an FEI SFEG-XL30 scanning electron microscope (SEM) which is equipped with a field emission tip. The acceleration voltage of the electron beam can be tuned between 1 and 30 keV. The beam current depends both on aperture/spot size and voltage and can be varied between several pA and approximately 40 nA. The latter corresponds to an electron impact on average every 5 ps, which is $\sim$ 2500 times longer than an optical cycle in the visible spectral range and $\sim$ 100 longer than the typical electronic relaxation times in gold [33]. Therefore, we can neglect electron-electron interactions and calculate the emission using single electron excitations. The beam diameter for a 30 keV electron beam at a current of 30 nA is approximately 10 nm on the sample surface. Accurate positioning of the electron beam over the sample is achieved using the electrostatic beam controls of the SEM.

The emitted light is detected using a Gatan MonoCL system. The light is collected using a parabolic aluminum mirror which is placed 1 mm above the sample so that its focal point coincides with the sample surface (see schematic Fig. 2.4(a)). The size of the focus is approximately 10 μm across. The mirror has a large acceptance angle covering, $1.42\,\pi$ sr of the full 2π of the upper half sphere. The angular range of acceptance angles is shown in Fig. 2.4 for the azimuth angle ϕ ($\phi = 0$ towards the wave guide) and zenith angle θ. As can be seen in the plot a large fraction of the radiation emitted with $\phi = 0$ is lost. Emission at large zenith angles towards the surface passes underneath the mirror edge and is not detected either. The hole in

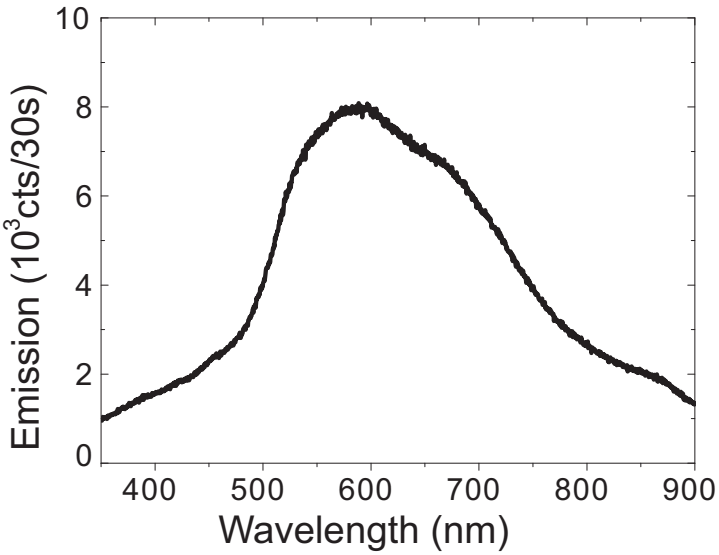

Figure 2.5: *Transition radiation spectrum measured for 30 keV electrons incident on gold for a beam current of 30 nA.*

the mirror through which the electron beam passes will not allow any detection for $\theta < 2°$, an effect that is not taken into account in the calculation.

The light collected from the focal point is reflected as a parallel beam through a hollow waveguide tube and focused onto the entrance slits of a monochromator. The light is spectrally resolved using a 150 lines/mm grating which is blazed for a wavelength of 500 nm. The light is dispersed and detected using a liquid-nitrogen cooled, front-illuminated CCD array detector with 1340x100 pixels. For the 150 lines/mm grating the bandwidth of detection is 560 nm with a resolution of approximately 10 nm for a typically used slit width of 2 mm. The dark count rate of the CCD was approximately 100 counts/s and was subtracted from the measurements.

2.4 Measurements

We have measured the TR emission as a function of electron energy for single crystalline gold. The electron beam was positioned far away from any structures on the flat surface so that no scattered SPPs would contribute to the CL signal. A typical spectrum for transition radiation measured for 30 keV electrons for a beam current of 30 nA is shown in Fig. 2.5. The emission has a broad spectrum covering the entire sensitivity range of our detector from around 350 to 900 nm and peaks around 600 nm, close to the surface plasmon resonance for Au at 540 nm.

To determine the beam energy dependence of emission intensity we have measured

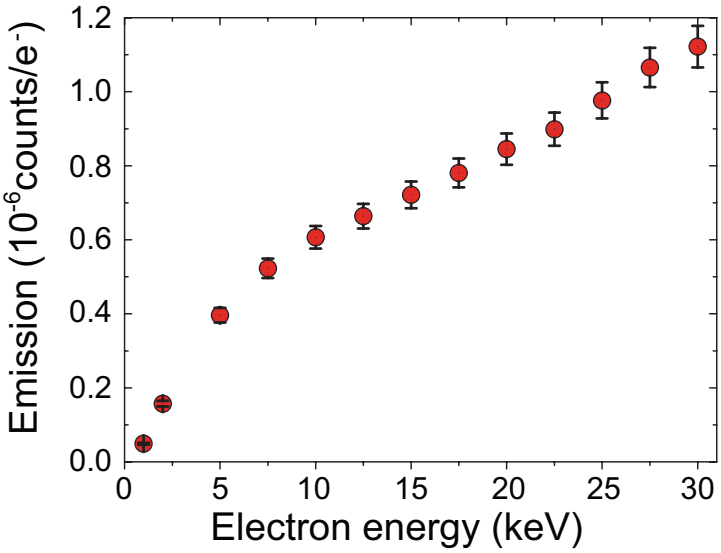

Figure 2.6: *Transition radiation as a function of electron energy for electrons incident on a single crystalline gold surface. The emission was integrated over the detector range from 350 nm to 900 nm. The data were normalized by the beam current.*

the transition radiation spectrum for energies from 1-30 keV. The measured emission spectrum was integrated over the range of the detector from 350-900 nm. The beam current was measured before and after our measurements using a Faraday cup and averaged. The beam current variation for a given energy is approximately 5 %. The TR emission was normalized by the beam current. The normalized TR intensity as a function of electron energy is shown in Fig. 2.6. A clear increase of the integrated emission with electron energy is observed, in agreement with theory (see in Fig. 2.3).

2.5 Measurement of the system response

The spectrum in Fig. 2.5 was not corrected for the spectral sensitivity of the CL system. While the sensitivity of the CCD detector is known, an accurate independent determination of the system response, including wavelength dependent mirror reflectivity, grating reflection efficiency and spectrometer throughput, is difficult. However, by measuring the transition radiation spectrum and comparing it to the theoretical emission spectrum we can obtain the system response [34]. This procedure allows to compare further measurements to electromagnetic calculations on absolute scales.

To do so, we measured the TR spectrum for 30 keV electrons with known beam current on a known material, in our case gold. The theoretical TR spectrum can

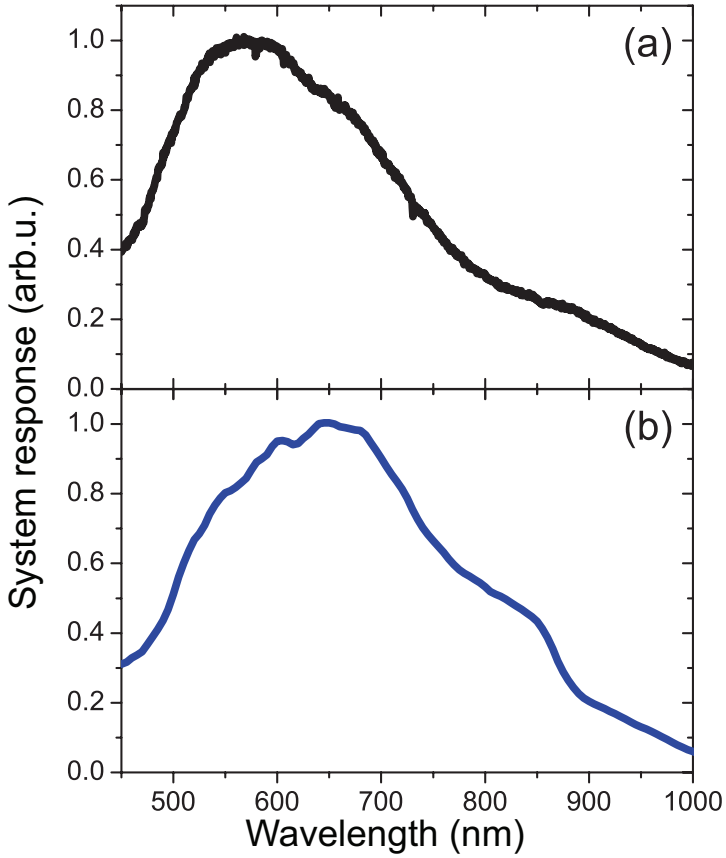

Figure 2.7: *(a) Normalized system response of the CL setup calculated by dividing a transition radiation spectrum for 30 keV electrons on gold through the calculated emission spectrum. (b) Normalized spectral response of the spectrometer grating and the CCD measured using a halogen lamp.*

be calculated for gold from the excitation probability integrated over the known acceptance angle of the CL mirror (Fig. 2.4). Dividing the measured curve over the calculated one results in a system response for the CL setup which can be used in further measurements.

In Fig. 2.7(a) we show the CL system response obtained in the described way. It increases with wavelength up to a maximum around 570 nm and decreases again for longer wavelengths. For comparison, the known normalized response of the spectrometer and the CCD array is shown in Fig. 2.7(b). It shows a similar behavior but does peak at a higher wavelength. As it was measured by inserting a halogen lamp behind the entrance slit of the spectrometer, it does neither include effects the wavelength

dependent outcoupling from the mirror nor the transmittivity of the vacuum windows in the beam path.

2.6 Boundary element method

In section 2.2 we have derived the excitation rates for transition radiation and surface plasmons for electrons incident onto the interface between a dielectric and a metal. For the simple case of planar, infinite media analytical solutions of Maxwell's equations can be derived. For more complex geometries like structured surfaces more elaborate calculation techniques are required.

In the course of this thesis we will use the retarded boundary-element-method (BEM) to calculate fields induced by an incident electron. Generally, in BEM the fields inside each homogeneous region are expressed in terms of boundary charges and currents that are calculated by imposing electromagnetic boundary conditions on the interfaces.

First calculations using nonretarded BEM were introduced by Fuchs [35] to compute optical properties of small, dielectric nanoparticles. Later, BEM has been used to calculate plasmonic modes inside channels cut into otherwise planar surfaces [36]. More recently, electron energy loss spectroscopy results were simulated using BEM for several particle structures [37].

We will show the derivation of BEM from Maxwell's equations as outlined by García de Abajo and Howie [38, 39]. The resulting equations can be used to calculate cathodoluminescence emission for structures with translationally or rotationally invariant interfaces.

2.6.1 Derivation of the basic elements of BEM

The basis for the BEM calculations are Maxwell's equations in the frequency domain. For media described by a position and frequency dependent dielectric function $\epsilon(\mathbf{r}, \omega)$ and assuming a non-magnetic material ($\mu = 1$), Maxwell's equations are given by Eqs. (2.1-2.4). The charge distribution ρ and current $\mathbf{j}$ for the incoming electron are given by Eqs. (2.5 and 2.6).

We rewrite Maxwell's equations by expressing the electric and magnetic fields in terms of scalar and vector potentials ϕ and $\mathbf{A}$.

$$\mathbf{E} = ik\mathbf{A} - \nabla\phi\,, \tag{2.21}$$

$$\mathbf{H} = \frac{1}{\mu}\nabla \times \mathbf{A}\,. \tag{2.22}$$

Using the Lorenz gauge

$$\nabla \cdot \mathbf{A} = ik\epsilon\mu\phi, \tag{2.23}$$

Maxwell's equations take the following form for the potentials:

$$(\nabla^2 + k^2\epsilon\mu)\phi = -4\pi\left(\frac{\rho}{\epsilon} + \sigma_s\right), \tag{2.24}$$

$$(\nabla^2 + k^2\epsilon\mu)\mathbf{A} = -\frac{4\pi}{c}(\mu\mathbf{j} + \mathbf{m}). \tag{2.25}$$

The quantities σ_s and $\mathbf{m}$ are proportional to the gradient in the dielectric and magnetic constants and take nonzero values only at the interfaces. Therefore, they can be understood as additional charges and currents introduced by the boundary. They do not represent physical quantities and are only related but not equal to any real boundary charges or currents. For the further derivation we will introduce surface charges σ_j and currents $\mathbf{h}_j$ that are determined by the boundary conditions for the electromagnetic fields at the interface between two materials. The general solutions for the potentials that vanish in each medium j at infinity can be written as:

$$\phi(\mathbf{r}) = \frac{1}{\epsilon_j(\omega)}\int d\mathbf{r}' G_j(|\mathbf{r}-\mathbf{r}'|)\rho(\mathbf{r}') + \int_{S_j} d\mathbf{s} G_j(|\mathbf{r}-\mathbf{r}'|)\sigma_j(\mathbf{s}), \tag{2.26}$$

$$\mathbf{A}(\mathbf{r}) = \frac{\mu_j(\omega)}{c}\int d\mathbf{r}' G_j(|\mathbf{r}-\mathbf{r}'|)\mathbf{j}(\mathbf{r}') + \int_{S_j} d\mathbf{s} G_j(|\mathbf{r}-\mathbf{r}'|)\mathbf{h}_j(\mathbf{s}), \tag{2.27}$$

where S_j refers to the boundary of each medium and

$$G_j(r) = \frac{e^{ik_j r}}{r} \tag{2.28}$$

is the Green's function which is a solution of the the scalar wave equation

$$[\nabla^2 + k_j^2]G_j(r) = -4\pi\delta(r). \tag{2.29}$$

The solutions for the potentials (Eqs. 2.26 and 2.27) are composed of two parts, where the first integral satisfies Eqn. 2.24 and 2.25 outside the interfaces for $\sigma_s = 0$ and $\mathbf{m} = 0$. The surface integral includes the effects of σ_s and $\mathbf{m}$ at the boundaries.

To find the solutions of Eqs. 2.24 and 2.25 we choose the boundary charges σ_j and currents $\mathbf{h}_j$ such that the electromagnetic fields satisfy the boundary conditions. The continuity of the tangential electric field and the normal magnetic field, lead together with the Lorentz gauge to the continuity of the potentials ϕ and $\mathbf{A}$. With Eqs. 2.26 and 2.27 the the boundary conditions can be rewritten as:

$$G_1\sigma_1 - G_2\sigma_2 = \phi_2^e - \phi_1^e, \tag{2.30}$$

$$G_1\mathbf{h}_1 - G_2\mathbf{h}_2 = \mathbf{A}_2^e - \mathbf{A}_1^e. \tag{2.31}$$

In Eqs. 2.30 and 2.31 we use a matrix form of the integrals, so that coordinates are used as matrix and vector indices, and matrix-vector products involve integration over the surface. The values ϕ_j^e and $\mathbf{A}_j^e$ are equivalent boundary sources that represent the respective surface integrals in Eqs. 2.26 and 2.27. These boundary sources are

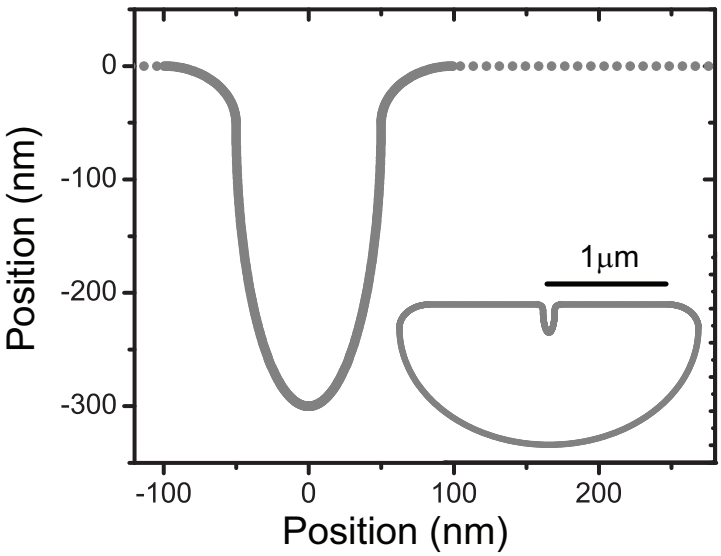

Figure 2.8: *Example of part of the discretized interface curve for BEM calculations. The boundary points on the flat areas are spaced by 10 nm, along the groove surface the step size is 5 nm. The inset shows the complete closed structure.*

potentials that would, in case of a homogeneous space filled with medium j, be created at the interface by the external charges and currents and scale linearly with those perturbations.

The continuity of the tangential magnetic field and the vector potential imply that the tangential derivatives of all components of the vector potential and the normal derivative of the normal vector potential are continuous. Using this, together with the Lorenz gauge we find:

$$H_1\mathbf{h}_1 - H_2\mathbf{h}_2 - ik\mathbf{n}_s(G_1\epsilon_1\mu_1\sigma_1 - G_2\epsilon_2\mu_2\sigma_2) = \alpha\,, \tag{2.32}$$

with $\alpha = (\mathbf{n}_2\cdot\nabla_s)(\mathbf{A}_2^e - \mathbf{A}_1^e) + ik\mathbf{n}_s(\epsilon_1\mu_1\phi_1^e - \epsilon_2\mu_2\phi_2^e)$, $\mathbf{n}_s$ the surface normal, and H_j the normal derivative of the Green's function G_j.

The continuity of the normal dielectric displacement leads to another equation:

$$H_1\epsilon_1\sigma_1 - H_2\epsilon_2\sigma_2 - ik\mathbf{n}_s\cdot(G_1\epsilon_1\mathbf{h}_1 - G_1\epsilon_1\mathbf{h}_1) = D^e\,, \tag{2.33}$$

where $D^e = \mathbf{n}_s\cdot[\epsilon_1(ik\mathbf{A}_1^e - \nabla\phi_1^e) - \epsilon_2(ik\mathbf{A}_2^e - \nabla\phi_2^e)]$ is the difference in normal displacement, that would be created at the interface by the external sources for an homogeneous space filled with the respective medium.

From Eqs. 2.30-2.33 the boundary charges σ_j and currents $\mathbf{h}_j$ can be self-consistently calculated. The incoming electron is introduced as an external charge via the

inhomogeneous terms. Using Eqs. 2.24 and 2.25 one finds the solutions to Maxwell's equations that vanish at infinity and satisfy the boundary conditions at the interfaces.

2.6.2 Numerical procedure

Equations (2.30 - 2.33) in the previous section constitute a set of linear surface-integral equations with σ_j and $\mathbf{h}_j$ being the unknown complex functions. To solve the set of equations we discretize the interface integrals by evaluating the spatial dependence of each quantity to a number of N surface points along the interface. The interface itself is discretized into a set of of interface elements that cover the surface and are chosen small enough so that the unknown boundary charges σ_j and currents $\mathbf{h}_j$ can be assumed constant over each element.

With this discretization we can approximate the operators in Eqs. 2.30 - 2.33 by $N \times N$ matrices and the interface charges and currents by complex vectors of dimension N. The resulting discretized system comprises of $8N$ linear equations with $8N$ complex variables that must be solved. For interfaces that are translationally invariant along one direction the number of points can be considerably reduced by working in Fourier space. In Fig. 2.8 we show a typical discretization of the boundary between two media. While small structures like the pictured groove must be discretized with a small step size of typically 2-5 nm, the step size for flat areas can increased to 10 nm due to the slowly varying fields in those regions.

The solutions of the numerical procedure for σ_j and $\mathbf{h}_j$ can be further used to determine the near-field close to the structure, the far field emission, the local density of states and the energy loss experienced by a passing electron.

3

Local density of states, spectrum and far-field interference

The surface plasmons polariton (SPP) field intensity in the vicinity of gratings patterned in an otherwise planar gold surface is spatially resolved using cathodoluminescence (CL). A detailed theoretical analysis is presented that successfully explains the measured CL signal based upon interference of transition radiation directly generated by electron impact and SPPs launched by the electron and outcoupled by the grating. The measured spectral dependence of the SPP yield per incoming electron is in excellent agreement with rigorous electromagnetic calculations. The CL emission is shown to be similar to that of a dipole oriented perpendicular to the surface and situated at the point of electron impact, which allows us to establish a solid connection between the CL signal and the photonic local density of states associated to the SPP.

3.1 Introduction

Surface plasmon polaritons (SPPs) are electromagnetic waves bound to the interface between a metal and a dielectric [1]. The strong coupling between optical radiation and the collective plasmon oscillations of the conduction electrons near the metal surface leads to a complex SPP dispersion behavior that can give rise to large field enhancements [15], negative refraction [18], and many other interesting phenomena resulting from sub-100 nm optics intrinsic to SPPs at visible and near-infrared frequencies.

A major bottleneck in nearly all studies on the fundamental properties of SPPs is the limited spatial resolution by which plasmonic phenomena can be measured. Optical microscopy suffers from the diffraction limit, whereas near-field microscopy has a resolution limited by the tip aperture to typically 100 nm. In contrast, SPPs can also be excited using high-energy electron irradiation, with the electron beam focused to a nanometer size spot, thus enabling the excitation of SPPs with nanoscale resolution. Only a few studies of electron-beam irradiation of plasmonic structures have been reported, mainly focusing on measurements of the mode distribution of plasmons in nanoparticles [25, 26, 40] or plasmon losses in planar surfaces [27, 28]. However, no detailed analysis of the different emission components and their interaction has been presented and no connection of the emission to the plasmonic density of states has been established.

In this chapter, we use electron-beam irradiation to study fundamental properties of SPPs propagating on a two-dimensional substrate. In particular, we use the electron beam of a scanning electron microscope (SEM) impinging on a single-crystalline Au substrate as a nanoscale source of SPPs with a broad spectral range. Our key findings are as follows: (1) We have developed a model of cathodoluminescence emission which includes the excitation of SPPs, eventually outcoupled from the Au surface, and transition radiation (TR) [22, 34], as well as the interference of the two components; (2) Extensive CL measurements performed over the visible spectrum and at distances up to a few microns from the grating are well reproduced by this model; (3) We measure the SPP generation yield per electron and find it to be in excellent agreement with rigorous electromagnetic calculations of this quantity; (4) The CL emission is found to be similar to that of a dipole positioned at the position of electron impact; (5) This similarity allows us to establish a solid connection beteween the CL signal and the photonic local density of states (LDOS) associated to SPPs.

3.2 Experimental

In our experiments, we use spatially-resolved cathodoluminescence spectroscopy (CL), a technique that combines scanning electron microscopy with the detection of optical radiation which is emitted from the sample. As described in chapter 2 the incident electron serves as a source of SPPs [32]. The SPPs propagate until they interact with a grating structured into the surface, where they are decoupled from the surface

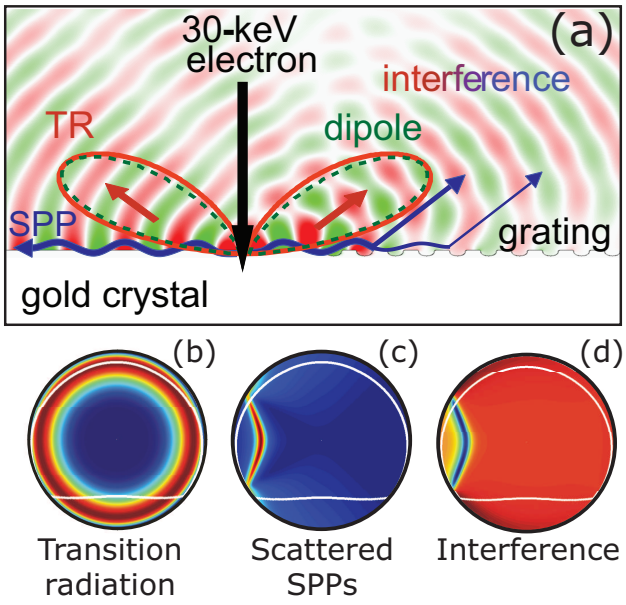

Figure 3.1: *(a) Schematic of an electron impinging on a gold surface generating surface plasmons (SPP) and transition radiation (TR) (all calculations are done for a wavelength of 700 nm and th electron incident 1000 nm away from the grating). The colored background shows the two-dimensional interference pattern of SPPs outcoupled by a grating with 400 nm period and TR calculated using the boundary element method. The calculated angular dependence of the emitted TR intensity is shown as a polar plot curve in red; the angular dependence of the emission of a dipole placed close to the metal is shown in dashed green. Azimuthal projection of calculated TR (b), radiation from scattered SPPs (c), and interference of TR and SPPs in the far field (d). All plots are normalized to their maximum value. The white contours reflect the collection range of the mirror. The grating is oriented vertically and its edge is located at the center of the plots.*

as light that can be detected in far field [see schematic Fig. 3.1(a)]. The impinging electron also produces TR [22, 34], the angular dependence of which is shown in Fig. 3.1(a). The angular emission pattern for TR resembles very much that of a classical dipole placed infinitesimally close above a planar metal surface, also shown in Fig. 3.1(a). The SPP and TR components of the emission are mutually coherent, so they produce interference in the far field where the CL detection takes place. To illustrate the interference, the colored background of Fig. 3.1(a) shows the two-dimensional near-field intensity distribution calculated using a two-dimensional boundary element

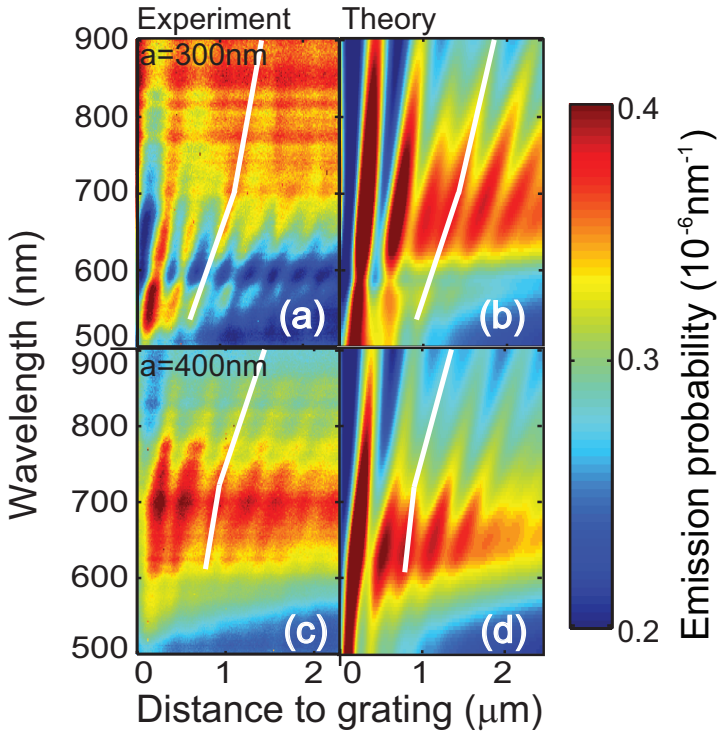

Figure 3.2: *Cathodoluminescence intensity for 30 keV electrons incident on single-crystalline Au, plotted as a function of detection wavelength and distance to the grating of Fig. 3.1. The grating period is 300 nm in (a) and (b), and 400 nm in (c) and (d). (a) and (c) are measurements for gratings carved in a single-crystal gold sample. (b) and (d) are calculations. The experimental data were corrected for system response.*

method [39] for an electron incident on a Au surface. The induced electric field is calculated for a geometry that is translational invariant along the direction perpendicular to the page and for wavevector components only in the plane of the page. The separate emission components from TR and outcoupled SPPs, as well as their interference, are easily identified.

In our experiments the sample consists of a single-crystal Au pellet of 1 mm thickness of which the surface was chemically polished down to nanometer roughness. Linear grating structures were milled into the surface with a 30 keV Ga^+ focused ion beam. Gratings consisting of 10 grooves were carved with periods a =300 nm, 400 nm, and 500 nm, respectively, groove width $\approx a/2$, depth $\approx$ 50 nm, and length

50 μm. Spatially-resolved CL spectroscopy was performed in a SEM using a 30 keV electron beam from a field-emission source focused onto the sample to a $\sim$ 10 nm diameter spot. A parabolic mirror, positioned above the sample, collects light emitted above it. Light is then spectrally resolved using a CCD array detector (bandwidth $\approx$ 10 nm) after passing a monochromator. The mirror acceptance solid angle is 1.4π. Spectra were corrected for system response, which was determined by normalizing measured raw data from a planar Au sample (no grating) to the calculated TR spectrum for Au [34]. This normalization allows us to compare the measured data to calculations on absolute scales and to compensate for the spectral response of our measurement system.

Figures 3.2(a,c) show the measured CL intensity, plotted as a function of wavelength and distance to the grating, for grating periods of $a = 300$ nm and $a = 400$ nm, respectively. Several characteristic features are clearly resolved in these plots:

(i) For wavelengths below 600 nm the CL intensity decays with distance from the grating. This is attributed to the strong damping of SPPs due to Ohmic losses in this wavelength range close to the SPP resonance at 540 nm. The observed CL decay with distance corresponds well to the decay length calculated using the dielectric constant for Au. At longer wavelengths, the SPP propagation distance is calculated to be larger than the scan range in Fig. 3.2, and only a weak decay is observed [27, 28]. These data confirm that a large portion of the CL intensity in Fig. 3.2 is due to outscattered SPPs.

(ii) Superimposed on the decay, we observe a periodic modulation of the CL intensity with distance with a period of about half the detection wavelength. This is clear evidence of the noted interference between TR and SPPs contributions to the emission, which can be either constructive or destructive depending on the phase difference ϕ [see Eq. (3.1)], increasing linearly with d.

(iii) For the longer wavelengths the amplitude of the oscillations decreases with distance roughly as $1/\sqrt{d}$, which is consistent with the distance dependence exhibited by any planar surface excitation originating in a point source, and in particular the SPP waves launched at the position of the electron beam [41].

3.3 Analysis

To model our experiment we have calculated the emission probability into SPPs and TR for an electron incident on a gold surface using the equation shown in chapter 2. Figures 3.1(b-d) show the calculated angle-resolved maps of the light intensity distribution due to outcoupled SPPs (b), TR (c), and their interference (d), respectively, all calculated for 30 keV electrons on Au at a wavelength of 600 nm. The TR is clearly isotropic in the azimuthal plane, while the scattered SPP distribution is highly anisotropic due to the presence of the grating. The solid angle of the parabolic mirror used to collect the CL is indicated by the white contours in Figs. 3.1(b-d).

The experimentally collected CL intensity corresponds to the integral over the emission angles Ω of the interference within the collection solid angles of the CL

mirror:

$$I_{CL} = \int_{mirror} d\Omega \ \left| A_{SPP}\mathbf{S}(\Omega)e^{i\phi} + \mathbf{f}_{TR}(\Omega) \right|^2, \tag{3.1}$$

where A_{SPP} is the SPP-excitation amplitude, $\mathbf{S}$ is the normalized far-field amplitude of a SPP scattered by the grating, $\mathbf{f}_{TR}$ is the far-field amplitude of TR, and ϕ is the phase difference between the SPP and TR emission components. This expression is exact at large distances d between the beam spot and the grating, and in particular, the TR field decays as $1/d$, whereas the SPP field becomes dominant near the grating, since it dies off only as $1/\sqrt{d}$ so that TR scattering by the grating is negligible for d above a few hundred nanometers. In our calculations, we have used rigorous, analytical solutions of Maxwell's equations for A_{SPP} [42] and $\mathbf{f}_{TR}$ [30] that are presented in chapter 2. In particular, A_{SPP} is obtained from the plasmon-pole contribution to the field produced by the electron crossing a semi-infinite metal-vacuum boundary. The dependence of I_{CL} on the separation d between electron beam and grating comes exclusively through the relative phase of SPP and TR contributions, $\phi \propto d$. The grating scattering factor is approximated as $\mathbf{S}(\Omega) = S_0/(k_x - 2\pi/a - i\Gamma/2)$, where k_x is the projection of the emitted photon momentum along the surface direction perpendicular to the grating, a is the grating period, and $\Gamma = 1/(N \cdot a)$ accounts for inelastic and radiative damping in the grating. We assume a mean free path of $N = 5$ periods, and a typical scattering efficiency $S_0 = 40\%$ [43]. These two constants are the only adjustable parameters in our model.

The calculated CL emission for two gratings of periods of 300 nm and 400 nm is shown in Figs. 3.2(b,d). We observe overall good agreement between measurements and calculated CL signal. Both the overall intensity as well as the periodic oscillations are very well resolved. Additionally, the period of the oscillations is a non-linear function of wavelength and depends on the pitch of the grating. This becomes clear by comparing the data with the white lines in Fig. 3.2, which are intended to guide the eye through a range of interference maxima. These curves both show a kink near a wavelength of 700 nm and quite different slopes above 700 nm, both in experiment and theory. Indeed, for the 400 nm grating the first-order grating coupling mode for SPPs with a wavelength longer than 700 nm lies outside the acceptance range of the mirror. This provides further evidence for coherent interaction between SPPs scattered from the grating and TR. From the good agreement of experiment and theory we conclude that far-field emission measurements are well described by the model of Eq. (3.1).

In a next step, we have extracted from the spatially resolved CL data in Fig. 3.2 the spectral distribution of SPPs generated by the electron beam. At each wavelength the CL intensity was integrated over the distance range of Fig. 3.2 correcting for the (measured) decay (thereby averaging out the oscillations). The obtained spectrum was then corrected for TR acquired at a position far away from the grating. Fig. 3.3(a) shows the result of this analysis for three different values of the grating pitch (symbols). A quite similar spectral shape is observed for all gratings, consistent with the fact that the generated SPP spectrum is independent of grating pitch. Fig. 3.3(a) also shows the calculated SPP spectrum under 30 keV electron excitation as well as

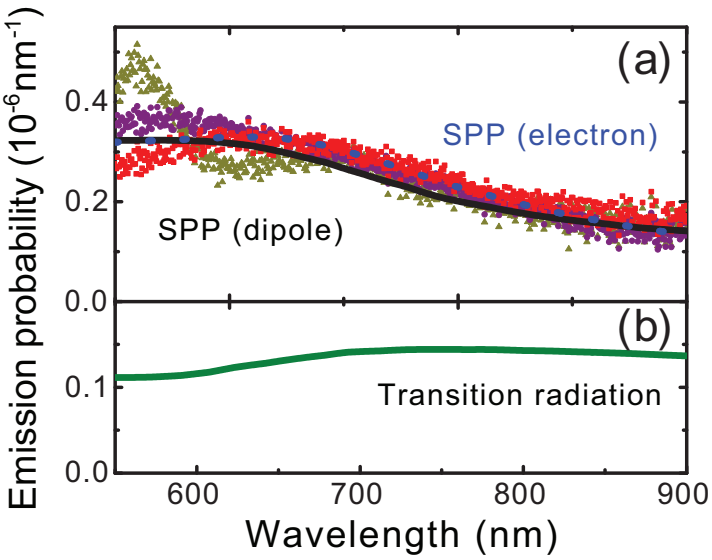

Figure 3.3: *(a) Spectrum of surface plasmon polaritons on single-crystal gold excited by 30 keV electrons and integrated over a line next to gratings with three different grating pitches [a =300 nm - yellow triangles, 400 nm - violet dots, 500 nm - red squares]. The solid lines show calculated spectra for SPPs generated by a 30 keV electron impinging on the surface (blue, dashed) and by a dipole positioned at the surface (black,solid). (b) Calculated transition radiation spectrum for 30 keV electrons on Au.*

the spectrum of SPPs that would be excited by a point dipole positioned at the metal surface. The dipole strength is taken as frequency independent in our calculations. These two calculations are analytical, rigorous solutions of Maxwell's equations [42]. The SPP emission rate of the dipole is plotted by normalizing the spectral integral of TR and the far-field dipole radiation. The small difference between these two calculated SPP spectra is attributed to the fact that the electron excites SPPs as it travels along its path, while the modeled point dipole is stationary. For comparison, Fig. 3.3(b) shows the calculated transition radiation spectrum which amounts to 30% of the SPP signal. The calculated spectra in Fig. 3.3(a) agree well with the experimentally determined spectra for longer wavelengths. The variations of the measured spectra for shorter wavelengths are ascribed to differences in coupling characteristics of the gratings and uncertainties in the correction for the SPP decay close to the SPP resonance.

The oscillations with distance in Fig. 3.2 are reminiscent of experiments performed by Drexhage, who studied the spontaneous emission of a rare earth complex in front

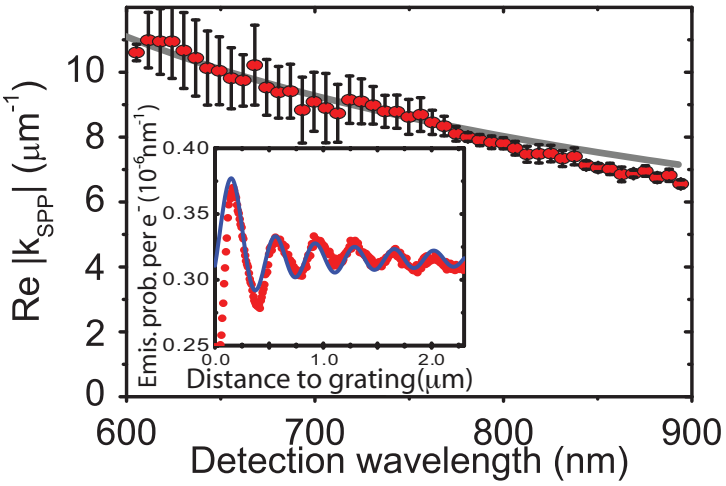

Figure 3.4: *The main figure shows the real part of the wave vector as a function of free space wavelength for surface plasmon polaritons excited on single-crystal gold. The red symbols are results of fitting a LDOS model to the measurements. The solid gray line is the calculated dispersion expected from optical constants. The inset shows the measured CL intensity (red symbols) as a function of distance for a wavelength of 750 nm. The solid blue line is calculated from the LDOS model of Eq. (3.2) with R adjusted to fit the experimental data.*

of a metal mirror [44]. It is well known that the spontaneous emission rate of optical emitters is proportional to the LDOS, as first experimentally demonstrated by Drexhage. Now, this allows us to construct an intuitive picture of the radiation generated by an impinging electron, which was shown to have an angular TR emission distribution (Fig. 3.1) and spectral coupling to SPPs similar to that of a point dipole[Fig. 3.3(a)]. The decay of this effective dipole into SPPs and TR is governed by the LDOS. The total decay rate is related to the LDOS ρ through the dipole decay rate $\Gamma = (4\pi^2\omega D^2/\hbar)\rho$ [45], where ω is the emission frequency and D is the dipole strength. The LDOS can be obtained from the projected field induced by the dipole on itself $E_\perp^{\mathrm{ind}}$ as [46]

$$\rho = \frac{\omega^2}{3\pi^2 c^3} + \frac{1}{2\pi^2\omega}\mathrm{Im}\left\{E_\perp^{\mathrm{ind}}/D\right\}, \tag{3.2}$$

where the first term on the right hand side is the vacuum LDOS. The normal induced field $E_\perp^{\mathrm{ind}}$ has a component due to the interaction of the dipole with the infinite planar surface and a distance dependent contribution arising from reflection of SPPs at the

grating:

$$E_{\perp}^{\mathrm{ind}} = E_{\perp}^{0}\left[1 + \frac{1}{\sqrt{2k_{SPP}d}} R e^{2ik_{SPP}d}\right], \tag{3.3}$$

where k_{SPP} is the momentum of the SPP and R is the reflection coefficient of the grating. Equation (3.3) predicts oscillations with distance d of period equal to half the SPP wavelength, in good agreement with our measurements.

We have calculated the local density of states from Eq. (3.2) under the approximation of Eq. (3.3) and adjusted R to fit the data in Fig. 3.2. The inset of Fig. 3.4 shows the experimental CL intensity as a function of position from Fig. 3.2(a) for a wavelength of 750 nm together with the calculated relative LDOS from our model. The used fit parameters were the reflectivity of the grating and the SPP wave vector. Good agreement between model and measurements is achieved without any convolution with a spatial resolution, proving the high resolution of the CL imaging technique. The main panel of Fig. 3.4 shows the real part of the SPP wave-vector extracted from these fits to the measurements for each wavelength. The experimentally determined SPP wave vectors agree well with the calculated dispersion using the dielectric function obtained from spectroscopic ellipsometry measurements of single-crystal gold. It should be noted that the present experiment probes the radiative part of (and not the absolute) LDOS, as (i) SPPs exhibit losses, in particular those incident to the grating at glancing incidence, and (ii) in the present geometry only SPPs in one two-dimensional half space (i.e., those launched towards the grating) are collected and interfere with the full TR contribution.

3.4 Conclusions

In conclusion, we have shown that spatially resolved cathodoluminescence spectroscopy on single-crystalline gold shows oscillations in CL emission with distance from a grating. These oscillations are ascribed to the interference between outcoupled SPPs and transition radiation. This interference holds great potential for exploring absolute phase changes during SPP scattering in nanostructured surfaces and provides a direct measure for the photonic local density of states associated to SPPs. Due to the nanoscale resolution of the exciting electron beam, cathodoluminescence yields information on basic plasmon properties that is not accessible to any other technique. The current measurement of the photonic LDOS with unprecedented resolution is of fundamental interest in photonics, as the LDOS controls the efficiency of several useful phenomena involving light absorption and emission.

4

Loss mechanisms of surface plasmon polaritons on gold

We use cathodoluminescence imaging spectroscopy to excite surface plasmon polaritons and measure their decay length on single-crystal and polycrystalline gold surfaces. The surface plasmon polaritons are excited on a gold surface by a nanoscale focused electron beam and are coupled into free space radiation by gratings fabricated into the surface. By scanning the electron beam on a line perpendicular to the gratings the propagation length is determined. Data for single-crystal gold are in agreement with calculations based on dielectric constants. For poly-crystalline films grain boundary scattering is identified as additional loss mechanism, with a scattering coefficient $S_G = 0.2\%$.

4.1 Introduction

Surface plasmon polaritions (SPPs) are electromagnetic waves bound to the interface between a metal and a dielectric [1]. They are being intensively investigated due to their possible application in nanophotonic integrated circuits, sensors, solar cells and other devices that take advantage of the strong optical field confinement at the metal/dielectric interface. SPPs decay by Ohmic losses in the metal which are largest for wavelengths close to the surface plasmon resonance. In addition, scattering from surface roughness, grain boundaries, and other imperfections causes losses. Ohmic losses can be readily calculated from optical constants that can be measured independently. In practice, experimental loss rates are often much higher than the calculated Ohmic loss [47]. Calculation of scattering processes is difficult because they depend on minute details in the structure. Therefore, experimental techniques are required to identify the loss processes for SPPs. If these mechanisms are known, metal fabrication techniques can be optimized so that metal structures with longer SPP propagation lengths can be made.

In this chapter we use cathodoluminescence imaging spectroscopy to measure the SPP decay [27, 28, 48] and present a detailed study of the propagation length of SPPs on gold surfaces. We compare a single-crystalline gold surface with poly-crystalline gold films with different grain sizes. We measure the SPP decay close to the plasmon resonance with nanometer resolution and extract the decay constants for a broad range of wavelengths. We show that losses are determined both by Ohmic losses and scattering at grain boundaries, and that surface scattering plays only a minor role.

4.2 Experimental

In cathodoluminescence (CL) an electron beam impinges onto the gold surface to create a perturbation in the density of conduction electrons. The corresponding effective dipole oscillation is the source for cathodoluminescence. The dipole decays by emitting into the far-field (transition radiation [34]) and by exciting SPPs [32, 41]. In our experiment the excited SPPs propagate over the surface and are coupled to the far-field using a grating structured into the metal surface. By measuring the amount of light coupled out from the grating as a function of distance between excitation point and grating the SPPs propagation length can be determined.

We prepared three different samples for our measurements. One sample consists of a single-crystalline gold pellet with a thickness of 1 mm. The surface was polished via chemical-mechanical polishing to sub-nanometer roughness as confirmed by atomic force microscopy (AFM). Two more samples were produced by electron-beam evaporation of a 120 nm thick gold film on a silicon substrate. Before the evaporation, the silicon substrates were cleaned in vacuum with a 300 eV argon ion beam. The films were evaporated at a rate of 0.05 nm/s under a pressure of 3×10^{-7}mbar. To achieve different grain sizes for the films one sample substrate was cooled during evaporation to liquid nitrogen temperature while the other was kept at room temperature. To

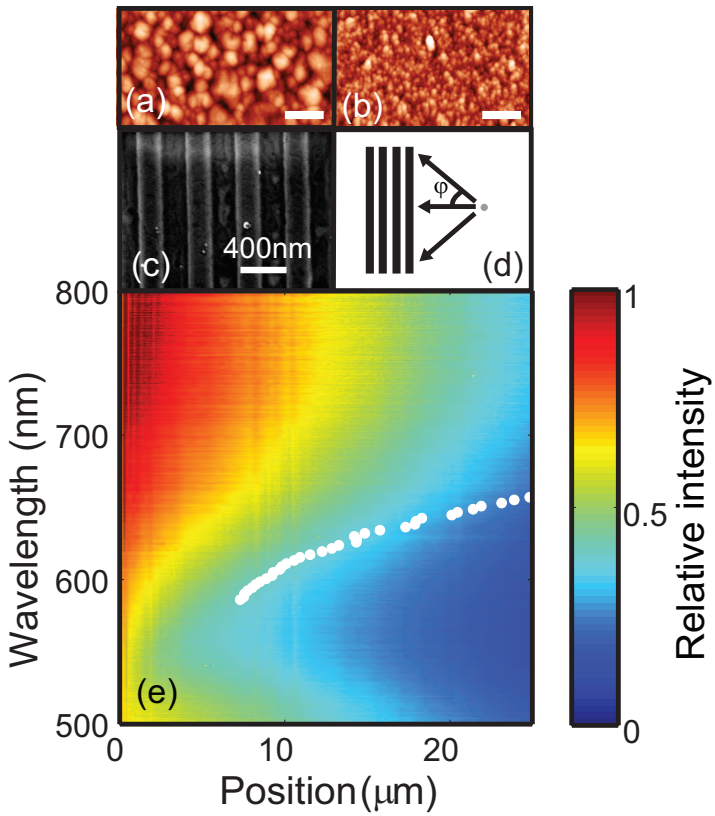

Figure 4.1: *(a,b) Atomic force microscope images of gold films evaporated at room temperature (a) and onto a cooled substrate (b). The scale bar is 100nm and the height variation is 1nm. (c) Scanning electron micrograph image of a grating fabricated in the single-crystal gold substrate. (d) Schematic drawing of SPPs propagating from the source to the grating over broad angular range. (e) Cathodoluminescence intensity as a function of detection wavelength and distance to a grating in a single crystalline gold surface. The edge of the grating at zero distance and the CL intensity was normalized to the intensity at zero distance for each wavelength. The white dot shows the fitted SPP propagation length, L_{SPP}, for this sample.*

reduce surface roughness of the evaporated metal both samples were irradiated with 300 eV argon ions at the last 30 s of the evaporation [49]. The two-dimensional surface profiles of the evaporated films, measured with AFM are shown in Figs. 4.1(a,b). Grain boundaries were easily identified in AFM and the average grain diameter was

determined to be $d = 80\,nm$ for the film deposited at room temperature (a) and $d = 20\,nm$ for the film deposited onto a cooled substrate (b).The root-mean-square surface roughness was 1.6 nm and 1.3 nm for the room-temperature and cooled deposition, respectively. Grating structures were milled into the surfaces of the metal with a 30 keV focused ion beam from a liquid gallium source. The gratings consisted of 10 grooves with a period of 400 nm and a groove depth of 50 nm (Fig. 4.1(c)). The single-crystalline gold sample will be referred as x-Au, the poly-crystalline sample as poly-LN and poly-RT for the cooled and the room temperature evaporated film, respectively.

We used the 30 kV electron beam of FEI XL-30 scanning-electron-microscope (SEM) using a field-emission source focused to a beam diameter of approximately 10 nm to excite SPPs on the gold surfaces. The scanning electron beam passes through a 1 mm-diameter hole in a parabolic mirror that is positioned above the sample. The light coming from the sample was collected using the parabolic mirror with an acceptance angle of about 1.4π sr. The collected light was sent through a monochromator and spectrally resolved with a CCD array detector with a resolution of approximately 10 nm.

4.3 Results and analyis

We measured the CL intensity as a function of position on a line normal to the grating up to a distance of 25 μm from the grating. The electron beam was scanned with a step size of 100 nm and at each position a spectrum was measured with an integration time of 10 s. The measured emission spectrum ranges from around 500 nm to the near-infrared region and peaks around 600 nm. The measured spectrum due to SPPs for a fixed position is determined by the excitation spectrum of SPPs by the electron beam, the propagation losses, the wavelength dependent outcoupling efficiency of the grating and the spectral response of the CL system. Since we are interested in the relative decay of the CL intensity, for each wavelength the measured CL signal was normalized to the intensity measured at the edge of the grating.

Figure 4.1(e) shows the normalized CL intensity for a line scan close to the grating as a function of position and detection wavelength for the single-crystalline gold sample. The edge of the grating is located on the left side at zero distance. As can be seen, for every wavelength the CL intensity decreases for increasing distance. For wavelengths above 550 nm the decrease in CL intensity is weaker for longer wavelengths, corresponding to a larger propagation for longer wavelengths. For 550 nm a minimum of the propagation length is observed; for shorter wavelengths the propagation length appears increased, as will be discussed.

The CL intensity $I(x)$ for the electron beam at a distance x away from the grating is given by the initial SPP generation rate $I_0(\lambda, \phi)$, the SPP decay length $L_{SPP}(\lambda)$ and the grating outcoupling efficiency $\alpha(\lambda, \phi)$, which depends on the incident angle ϕ

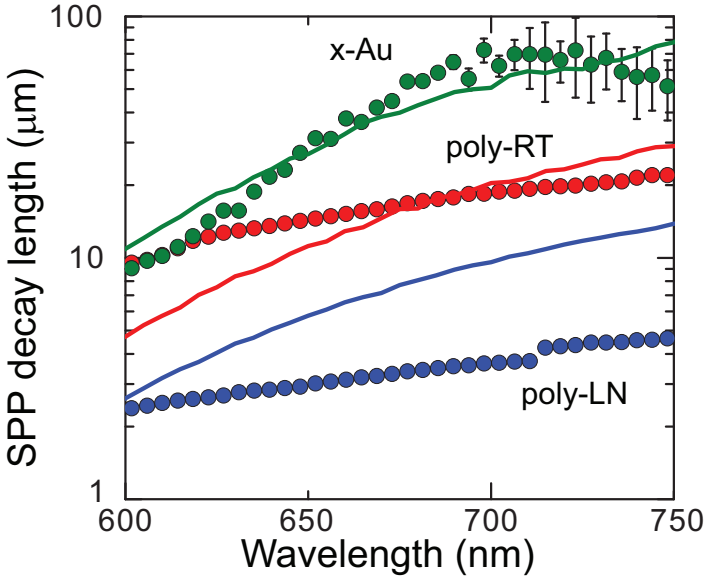

Figure 4.2: *Surface plasmon polariton propagation length as a function of wavelengths for three different samples from fits to measurements as in Fig.4.1(e). The green dots are for single-crystalline gold (x-Au), the blue and red dots are for poly-crystalline gold films deposited at room-temperature (poly-RT) and liquid-nitrogen temperature (poly-LN), respectively. The solid lines are propagation lengths calculated from the dielectric constants measured for the respective samples.*

relative to the grating normal (see schematic in Fig. 4.1(d)):

$$I(x) = I_{TR} + \frac{1}{2\pi}\int_{-\pi/2}^{\pi/2} \alpha(\lambda,\phi) I_0(\lambda,\phi) \exp\left(\frac{-x}{L_{SPP}(\lambda)\cos(\phi)}\right) d\phi \qquad (4.1)$$

Eqn. (4.1) also includes a constant background, I_{TR}, to account for transition radiation. To obtain the plasmon propagation length $L_{SPP}(\lambda)$ we fitted Eqn. (4.1) for each wavelength in the data set of Fig. 4.1(e) assuming an angle-independent coupling efficiency $a(\lambda,\phi) = 1$. The results of the fits for L_{SPP} are shown in Fig. 4.1(e) as white dots. We have plotted the values for L_{SPP} only above 600 nm. In this region, we observe an increase of propagation length with wavelength as expected.

Interestingly, as can be seen in Fig. 4.1(e) for wavelengths shorter than 600 nm we observe CL intensity farther away from the grating. This would mean that the SPP propagation length seems to increase with decreasing wavelength. In this wavelength range SPPs are not purely bound to the surface, as their real part of the normal wavevector component k_z increases strongly with decreasing wavelength. The result-

ing radiative loss causes a strong decrease in propagation of bound SPPs. However, in the present experiment, the effect of this loss process, radiation, is collected by the detection system. As Eqn. 4.1 does not account for this effect, these data are not further analyzed here.

A similar analysis as in Fig. 4.1(e) for the single crystalline sample was done for the two poly-crystalline samples. Figure 4.2 (symbols) shows the fitted propagation lengths for the three different samples. The spread in data extracted from different measurements for the same sample was approximately 10-20%. For fitted propagation lengths that are longer than the scan range of 50 μm we have added error bars. The longest propagation lengths are found for the single crystalline gold sample. The shortest propagation lengths are found for the poly-crystalline samples with the smallest grain size.

Considering only Ohmic losses the SPP propagation length can be calculated from the imaginary part of the SPP wave vector k_x

$$L_\Omega = \frac{1}{2\mathrm{Im}k_x} \tag{4.2}$$

For a semi-infinite metal in air the wavevector is given by $k_x = \lambda/(2\pi)\sqrt{\epsilon/(\epsilon+1)}$ with ϵ the dielectric constant of gold and λ the free-space wavelength. For a thin film on a substrate leakage radiation must also be taken into account. We have calculated the dispersion relation for the three-layer system of a gold film in air on a silicon substrate and derived L_Ω from k_x as in Eqn. (4.2) for the poly-crystalline films. The dielectric constants of the three different samples were measured by ellipsometry.

The drawn lines in Fig. 4.2 show the propagation lengths for SPPs on our three samples calculated from these dielectric constants. Note that these include no free parameters. Already the calculated propagation lengths differ for the studied samples by an order of magnitude mainly due to different dielectric constants. The large variation of dielectric constants can be explained by a reduction of the mean free path for electrons by introduction of grain boundaries, voids and roughness [50]. For single-crystalline gold, for wavelengths longer than 600 nm the measured values of propagation length are in good agreement with the calculations. For the large-grain poly-crystalline (poly-RT) sample data and calculation are in reasonable agreement for longer wavelengths. For the small grain size sample the experimental data lie well below the calculation for larger wavelengths. This indicates that additional loss mechanisms are involved which decrease the SPP propagation length and can not be described by Ohmic losses.

One possible additional loss mechanism is scattering at surface roughness of the metal. However, given the small surface roughness of our samples as measured using AFM this effect is negligible [51]. With the given geometrical parameters of our samples the contribution of scattering at roughness can be estimated to be a factor of 500 smaller than the Ohmic losses. Even more, as the roughness values for all our samples are very similar the effect of scattering at roughness should be similar for all samples. Therefore, we can not explain the deviations in SPPs propagation length by surface roughness.

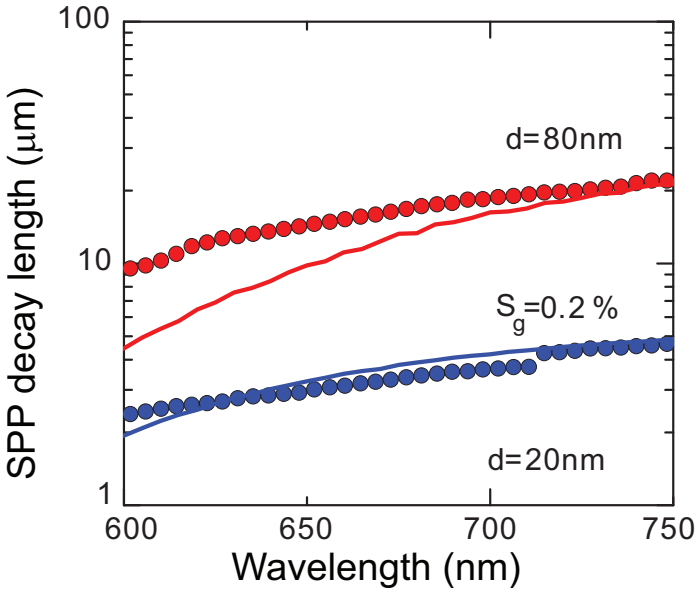

Figure 4.3: *Surface plasmon polariton propagation length as a function of wavelengths for two different grain sizes. The symbols are the decay lengths as obtained from measurements. The drawn curves are calculated including grain boundary scattering for grain sizes of 20 and 80 nm, respectively and a grain boundary scattering coefficient* $S_G = 0.2\%$.

Next, we consider grain boundary scattering of SPPs. In few other studies the effect of grain boundary scattering has been considered as a loss mechanism for both bulk and surface plasmons [52, 53]. The proposed reason for the scattering lies mainly in inhomogeneities of the free-electron gas due to grain boundaries. As far as we know, no quantitative studies on the effect of grain boundary scattering of SPPs have been published. In a simple model for grain boundary scattering the effective propagation length equals $L_G = d/S_G$, with S_G the grain boundary scattering coefficient and d the average grain diameter (for $d \ll L_G$). Adding this loss term to the Ohmic losses, we fitted our data for $\lambda \gg 600\ nm$ for the two poly-crystalline samples, with d taken from AFM measurements and S_G as a free parameter, but identical for both samples. We find a reasonable fit of the calculation with both data sets assuming $S_G = 0.2\%$. The results of our calculations are plotted as lines in Fig. 4.3 together with the measured curves for the polycrystalline films. So far, a model for Ohmic and scattering losses is found that fits well the data for all three samples in the wavelength range above 600 nm.

4.4 Conclusions

In conclusion, we have performed cathodoluminescence imaging spectroscopy to measure the propagation length of surface plasmon polariton propagation on single-crystalline and poly-crystalline gold surfaces. From the measurements we have determined the SPP decay lengths as a function of wavelength in the 600-750 nm range. Largest propagation lengths (10-80 μm), in agreement with optical constants, are found for single-crystalline Au. Much reduced propagation lengths are found for polycrystalline films. We find that grain boundary scattering is an important plasmon loss mechanism in polycrystalline thin films. The data is consistently fitted using a grain boundary scattering coefficient of 0.2%.

5

Fabry-Perot resonators for surface plasmon polaritons

Surface plasmon polariton Fabry-Perot resonators were made in single-crystalline gold by focused ion beam milling of two parallel 100 nm deep grooves. The plasmonic cavity modes were spatially and spectrally resolved using cathodoluminescence spectroscopy. Mode numbers up to $n = 10$ were observed. The cavity quality factor Q depends strongly on groove depth; the highest $Q = 21$ was found for groove depth of 100 nm at $\lambda = 690\,nm$. The data are consistent with finite-difference time domain calculations that show that the wavelength of maximum reflectivity is strongly correlated to groove depth.

5.1 Introduction

Surface plasmon polaritons (SPPs) are electromagnetic waves bound to the interface between a metal and a dielectric [1]. The strong coupling between optical radiation and the collective plasmon oscillations of the conduction electrons near the metal surface leads to large field enhancements at the interface. At frequencies close to the plasmon resonance, SPPs possess large wave vectors, enabling sub-100 nm optics at optical frequencies. By varying the metal thickness, the SPP dispersion can be further tailored. SPPs thus enable two-dimensional optics in which optical information can be guided and processed at the nanoscale. While the propagation of SPPs has been well studied [6, 27, 28, 54], a next challenge is to obtain control over the confinement of SPPs.

So far, reflectors composed of arrays of nanoparticles [55] and Bragg cavities [56] composed of arrays of very shallow grooves or ridges have been studied to achieve SPP confinement. Weeber *et al.* showed that two parallel ridge gratings can act as Bragg-mirrors and can confine plasmons between the mirrors. Because of the narrowband reflection of these gratings the field enhancement was only observed for a small wavelength range. Kuzmin *et al.* measured standing SPPs modes generated between two slits in a gold film in a transmission configuration [57].

In this chapter, we use a single deep groove in the surface of single crystalline gold as an effective mirror for surface plasmons. By placing two parallel grooves on the surface we construct a Fabry-Perot resonator for SPPs. We use cathodoluminescence imaging spectroscopy [27, 28] to excite the resonators and determine the spatially resolved cavity field profile. From the observed field profile we determine the mode numbers and cavity quality factor. Studies of the quality factor as a function of groove depth show a maximum of $Q = 21$ at a groove depth of 100 nm. Finite-difference time domain (FDTD) calculations of the groove reflectivity show an increase of reflectivity for these depths, supporting the experimental observations.

5.2 Experimental

Experiments were performed on a single-crystal Au pellet of 1 mm thickness (effectively semi-infinite for optical fields) of which the surface was chemically polished down to nanometer roughness. Two parallel linear grooves were milled into the surface with a 30 keV Ga^+ focused ion beam (see schematic in Fig. 5.1 (a)). The groove separation w was 3000 nm, the depth d was 100 nm, and the groove width was 50 nm full width at half maximum(FWHM). The groove shape and geometry were determined from scanning electron microscopy (SEM) images of a cross-section of a groove pair (see Fig. 5.1(b)). To fabricate the cross-section a box was milled into the surface next to the grooves. To achieve the proper contrast to image the gold profile, platinum was first deposited over the grooves with focused-ion beam assisted deposition.

Spatially-resolved cathodoluminescence (CL) spectroscopy was performed in a SEM using a 30 keV electron beam from a field-emission source focused onto the

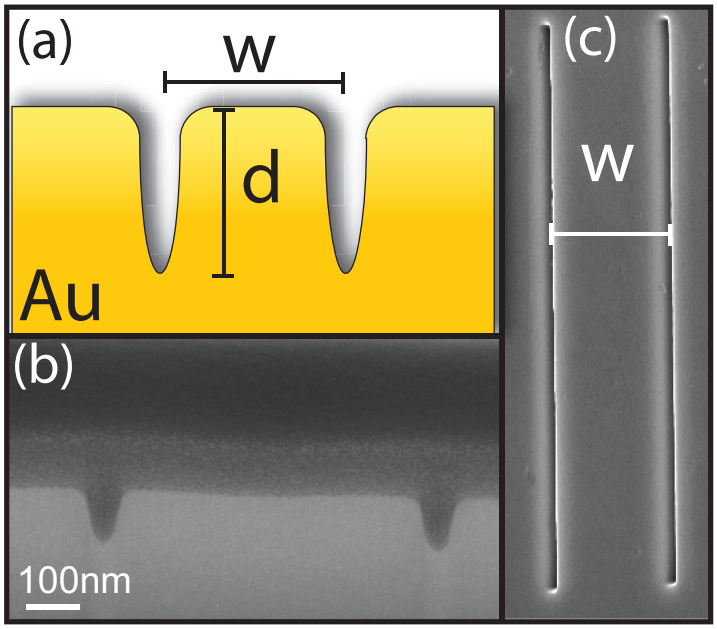

Figure 5.1: *(a) Schematic of the double-groove Fabry-Perot cavity in a gold surface. (b) Cross-section SEM image of the double groove structure. The grooves were filled with platinum and then a box was structured to allow side view. (c) SEM top-view of the double groove structure. w indicates the center-to-center groove spacing.*

sample to a $\sim$ 10 nm diameter spot. The electron beam effectively acts as a point source for SPPs with a broadband spectrum ranging from the SPP resonance at 550 nm well into the infrared [27, 28]. The scanning electron beam passes through a hole in a parabolic mirror that is positioned above the sample. The mirror collects light emitted from the sample, that is then focused on the entrance slit of a monochromator and spectrally resolved using a CCD array detector (bandwidth $\approx$ 10 nm). The mirror acceptance solid angle is 1.42π. The measured CL spectra were corrected for system response, which was determined by normalizing the measured raw data from a planar Au sample (no grating) to the calculated transition radiation spectrum for 30 keV electron-irradiated Au [34]. The experimental count rate was 100-500 counts per second per wavelength channel at an electron beam current of 28 nA.

We measured the CL spectra as a function of electron beam position along line scans perpendicular to the groove pairs with a step size of 5 nm and integration time of 1 s. Figure 5.2 shows the CL intensity for line scans over the double grooves for three different wavelengths (650 nm, 765 nm, and 840 nm). The peaks in the CL intensity coincide with the position of the grooves. Between the grooves a periodic pattern of the CL emission is observed for all wavelengths. The period of the oscillation equals

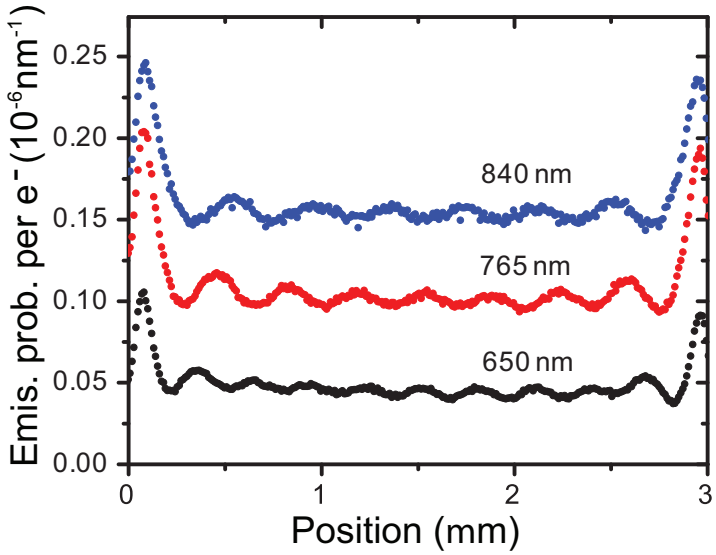

Figure 5.2: *Cathodoluminescence line scans (30 keV electron beam) over a double groove structure (w=3000 nm, d=100 nm) for wavelengths of 650 nm (black symbols), 765 nm (red symbols), and 840 nm (blue symbols). The grooves are located at 0 and 3 μm. The curves are shifted vertically by 0.05 (765 nm) and 0.1 (840 nm) for clarity.*

approximately half the free-space wavelength for all three studied wavelengths.

The oscillations in the CL intensity are consistent with a standing SPP wave between the two grooves of the structure. The double-groove structure thus acts as a Fabry-Perot resonator with the grooves acting as SPP reflectors. The interference condition for the SPP Fabry-Perot cavity is given by $2dk_{SPP} + 2\phi = 2\pi n$ with d the cavity length, k_{SPP} the SPP wave vector, ϕ a phase shift upon reflection and n the mode number. Note that in CL spectroscopy the spatial resolution results from the known profile of the exciting electron beam. The oscillations in the radiation that are observed in the far-field are due to the fact that the electron preferentially excites SPPs at positions of maximal electric field amplitude *i.e.* the antinodes in the standing wave pattern.

Figure 5.2 also shows that the visibility of the interference fringes increases with increasing wavelength. This is consistent with the larger SPP propagation length for larger wavelengths. For the shortest wavelengths the amplitude of the oscillations increases closer to the grooves again consistent with the shorter propagation length. Indeed, the SPP propagation length at 650 nm is a factor five shorter than at 840 nm [6].

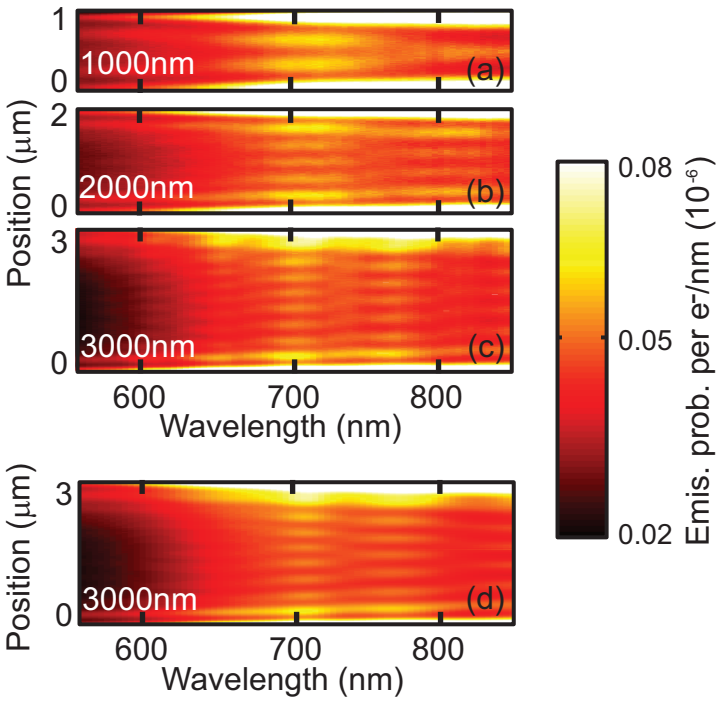

Figure 5.3: *Cathodoluminescence as a function of position and wavelength for line scans across three SPP Fabry-Perot resonators with different center-to-center groove separation ((a) w =1000, (b) 2000, and (c) 3000 nm). Multimode spectra with $n = 2 - 10$ are observed. (d) Reconstruction of the data in (c) using a factor analysis method.*

5.3 Mode numbers

To further study the Fabry-Perot interference condition, we structured groove pairs with different groove separations into the gold surface, keeping the groove depth and width constant. Figure 5.3 (a-c) shows the measured CL intensity as a function of position and wavelength for three groove separations of 1000, 2000, and 3000 nm, respectively. As can be seen, for wavelengths above 600 nm the measurements clearly show the standing wave pattern in the CL intensity. In the region below 600 nm the CL intensity decreases as a function of distance to the grooves showing only weak oscillations in particular for the largest cavity. In this region the SPP propagation length is shorter than the cavity length and no standing waves can form.

From the intensity maxima observed in Fig. 5.3 the resonant modes can be identified. For example, for the 1000 nm wide resonator two maxima are observed in the standing wave pattern at 700 nm, corresponding to a $n = 3$ mode. Similarly, $n = 6$

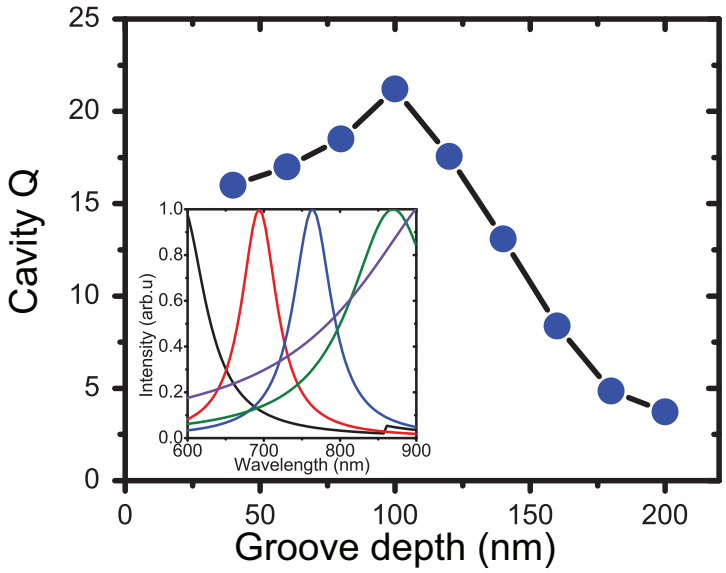

Figure 5.4: *Quality factor for groove resonators for the resonance at 690 nm as a function of groove depth, extracted from cathodoluminescence line scans. The inset shows the resonance spectra at 640 nm, 690 nm, 765 nm, 870 nm, and 980 nm derived from CL data for a resonator with 100 nm deep grooves ($w = 3000$ nm, last panel in Fig. 3*

and $n = 9$ modes are observed for the 2000 nm and 3000 nm wide resonators. Due to the smaller free spectral range for the 3000 nm wide cavity a wide distribution of modes is observed around 700 nm ranging from $n = 7 - 11$.

It is interesting to note that a $n = 3$ mode at 700 nm would correspond to a resonator width of 1020 nm (taking into account the dispersion of SPPs at 700 nm) which is 20 nm wider than the center-to-center spacing of the grooves. This implies that the effective cavity length is larger than the center-to-center spacing. This is consistent with the fact that the SPPs 'probe' the depth of the grooves in their reflection. In this model the effective cavity length offset should be identical (20 nm) for all cavity lengths. Indeed, the $n = 6$ and $n = 9$ modes shift to slightly shorter wavelengths for the 2000 nm and 3000 nm resonators. Note that this analysis assumes no phase shift upon reflection from the grooves.

5.4 Analysis of the quality factor

Next, we determined the quality factor of the resonators. To do so, we have structured a range of resonators into the single-crystal gold surface for which we varied the groove depth and thereby the reflectivity. The depth was varied in the range of 20 nm to 200

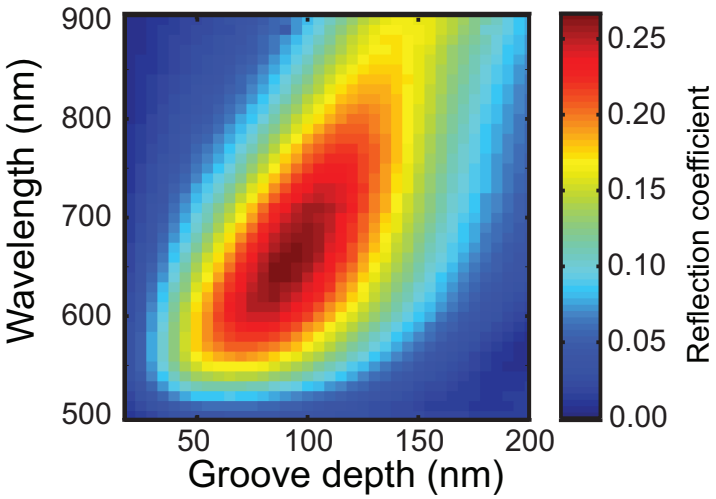

Figure 5.5: *Reflection coefficient for SPPs at a single 50 nm wide groove in gold as a function of groove depth and SPP wavelength, as determined from FDTD calculations.*

nm keeping the width approximately constant to 50 nm FWHM. The CL intensity was measured on a line perpendicular to the grooves with a step size of 10 nm. The CL line scans show interference fringes as in Fig. 5.2 for all wavelengths but with different degrees of visibility. The visibility increases with increasing depth for groove depths up to 100-120 nm. For deeper grooves the visibility decreases.

To determine the quality factors we performed a factor analysis [58] on the spectral CL line scan for a groove depth of 100 nm and width of 3000 nm (see Fig. 5.2(c)) to determine the resonance spectra. Five significant resonances at wavelengths of 640 nm ($n = 10$), 690 nm ($n = 9$), 765 nm ($n = 8$), 870 nm ($n = 7$), and 980 nm ($n = 6$) were found to represent the data well. We reconstructed the experimental data from the resonances by fitting their line width and spatial position. The reconstructed data is shown in Fig. 5.3(d) and shows very good agreement with the data. The inset of Fig. 5.4 shows the five resonance spectra. The quality factor for each resonance is given by the resonance wavelength divided by the line width. The smallest line widths are observed for the central modes at 695 and 740 nm. Lower quality factors are observed for the 640 as well as the 870 and 890 nm modes.

The quality factor of the resonator is determined by propagation losses and the reflectivity of the mirrors. For the shortest wavelength (640 nm), propagation losses dominate, as was also apparent from Fig. 5.2 and a larger line width is observed (see inset Fig. 5.4). To determine the reflectivity of a single groove for SPPs we have performed FDTD calculations. We used a two-dimensional simulation with the groove profile modeled according to the SEM images of the cross cuts. The SPP mode was generated at a distance of 2 μm away from the groove. Reflection and transmission of

the groove were monitored using field monitors past the groove and behind the source. Figure 5.5 shows the calculated groove reflectivity as a function of wavelength and groove depth. For each wavelength a maximum of the reflection coefficient is observed for a certain groove depth. The wavelength of the maximum increases with groove depth. The maximum reflection coefficient for 100 nm deep grooves is observed in the range of 650-700 nm. This is consistent with the smaller line width observed for the modes in that wavelength range in the inset of Fig. 5.4 or, correspondingly, the fact that the highest visibility resonances in Fig. 5.3 are observed around 700 nm.

We have performed the factor analysis for the line scans of the other depths (20-200 nm). Figure 5.4 shows the quality factor for the resonance near 690 nm as a function of groove depth. The quality factor increases for increasing groove depth reaching a maximum of $Q = 21$ at 100 nm, and decreases for for larger groove depths. This is again consistent with Fig. 5.5.

5.5 Conclusions

In conclusion, we have investigated Fabry-Perot resonators for surface plasmon polaritons consisting of two parallel grooves. Cathodoluminescence allowed direct imaging of the field profile inside the cavities and determine mode numbers up to $n = 10$. The cavity quality factor was found to depend strongly on groove depth and wavelength, showing a maximum of $Q = 21$ at 700 nm for a groove depth of 100 nm. Further work will focus on achieving understanding of the details of the groove reflection of SPPs, taking into account localized modes inside the groove cavities [59].

6

How grooves reflect and absorb surface plasmon polaritons

The reflection of surface plasmon polaritons by deep linear grooves structured into gold surfaces is investigated with numerical finite-difference-in-time-domain as well as boundary-element-method calculations. Groove widths of 25 and 100 nm are studied, with depths as large as 500 nm. The reflection depends strongly on wavelength, groove depth and width. By systematically varying these parameters and studying the field profiles in the grooves as well as dispersion, we relate the resonances of the reflectivity to resonant coupling of propagating planar plasmon modes to cavity modes inside the grooves. By careful design of the groove width and depth the reflectivity can be tuned to values up to at least 30% for either a narrow or wide band of wavelengths.

6.1 Introduction

Recent advances in nanoscale structuring have opened up new possibilities in the field of nanophotonics. Surface plasmon polaritons (SPPs) [1] can be employed as a way to improve the performance and reduce the size of photonic circuits. The two-dimensional character of SPPs makes it possible to confine electromagnetic radiation below the diffraction limit, offering unprecedented possibilities for subwavelength photonics [12].

Reflectors for SPPs are important elements in plasmonic integrated circuits, as they allow guiding and steering of SPPs and constitute basic building blocks for plasmonic resonators. Grating-like Bragg reflectors consisting of arrays of parallel shallow grooves or ridges are widely used as reflecting components and much research has been devoted to their optimization [60]. Reflectivities almost up to 100 % have been reported experimentally for reflectors spanning tens of grating periods [61]. Single grooves structured into the the surface can also act as a reflector for SPPs and have much smaller size.

While the theoretical work on the reflectivity of Bragg reflectors is extensive [62, 63, 64], the reflectivity of single grooves has not been investigated in much detail. Moreover, a restricted range of groove geometries have been studied. Existing studies are mainly restricted to shallow grooves due to the used perturbation approach. Recently, Nikitin *et al.* [65] reported on the reflectivity and scattering coefficients of shallow grooves for normal in-plane incidence. Further work on grooves in metal surfaces focused mainly on the absorption properties of light by grooved surfaces rather than SPP reflection [66, 67, 68].

In this chapter we investigate the possibility of using single grooves as efficient reflectors for surface plasmons. We show that suitably designed deep single grooves can perform as efficient and broadband reflectors for SPPs. We have used finite-difference-in-time-domain as well as boundary-element-method calculations to determine the reflectivity for grooves with varying geometrical parameters. We show that the observed high reflectivity is a result of efficient coupling of propagating planar modes to resonant groove modes.

6.2 Reflectivity of single grooves

We used two-dimensional finite-difference-time-domain (FDTD) calculations to obtain the reflection coefficient of surface plasmons incident onto a groove structured in an otherwise planar gold surface. The system was modeled as an infinite box with the optical constants of gold taken from Palik [69]. A groove was structured with a profile similar to the ones used in experimental studies . In particular, the groove profile is composed of two quarter-circles with radius $r = 50$ nm and a half-ellipse with minor radius a equal to half the groove width and the major radius equal to $b = d - r$, with d the groove depth (see inset Fig. 6.1(a)). A surface plasmon was launched at a distance of 1 μm from the groove edge under normal incidence. The transmission through the

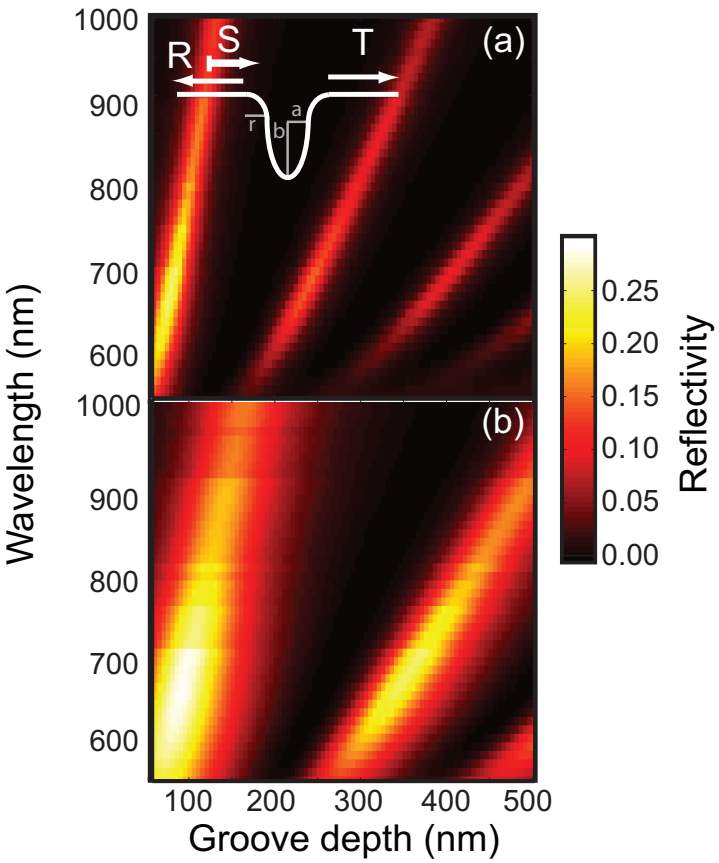

Figure 6.1: *Reflectivity for surface plasmons incident perpendicularly onto a groove structured into a gold surface as a function of groove depth and wavelength calculated using FDTD. Groove width: (a) 25 nm; (b) 100 nm. The inset shows a schematic of the groove shape.*

groove was monitored with a frequency domain monitor positioned at the far side of the groove while the reflection was recorded with a monitor behind the source. The grid size for the calculations was 3 nm and was refined around the surface layer and the groove to 0.9 nm. The simulation region was bound by perfectly matched layers (PMLs) to absorb SPPs leaving the region of interest. The reflectivity of the PML was found to be smaller than 0.1% and did therefore not significantly influence our results.

In Figure 6.1 we show the reflectivity of the groove as a function of groove depth and wavelength for groove widths (a) $d = 25$ nm and (b) $d = 100$ nm, respectively. For both widths we observe maxima of the reflectivity that depend on wavelength and

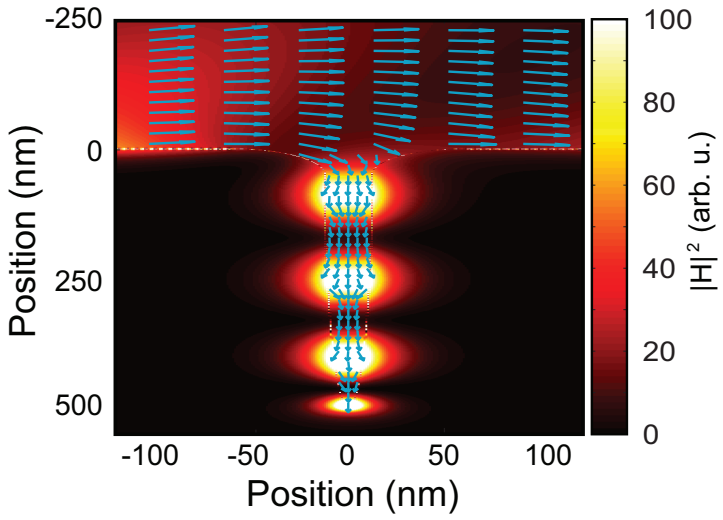

Figure 6.2: *Magnetic field intensity calculated with the boundary element method for a 500 nm deep groove at a wavelength of 640 nm. The SPP was launched by an incoming electron impacting 2900 nm to the left of the groove. The blue arrows denote the Poynting vector.*

groove depth. The highest reflectivity (29%) is observed for the 100 nm wide grooves and appears for groove depths of 100-120 nm at wavelengths between 600 and 750 nm. For the 25 nm wide groove a nearly as high reflectivity maximum (25%) is found in the same wavelength range, for slightly smaller groove depth. The reflectivity maxima in Fig. 6.1 roughly show a linear trend with increasing groove depth. The narrower groves (a) are much more dispersive than the wider ones (b) as more maxima are observed for the same wavelength. Moreover, maxima for deeper grooves show a narrower width of the reflectivity resonances.

6.3 Reflectivity and field enhancement

To gain insight into the origin of the reflectivity maxima, we have computed the local field inside a 25 nm wide, 500 nm deep groove at the wavelength of maximum reflectivity (640 nm). We used the boundary element method (BEM) to calculate the local magnetic field [39]. The magnetic near-field intensity calculated for a plasmon incident from the left onto the groove is shown in Fig. 6.2. Inside the groove a standing wave pattern can be observed and the maximum field intensity is a factor of three higher than for the incoming plasmon. The arrows in Fig. 6.2 represent the Poynting vector, which shows the energy flux in the system. Away from the groove the energy flows from left to right, the direction of SPP propagation. Near the groove,

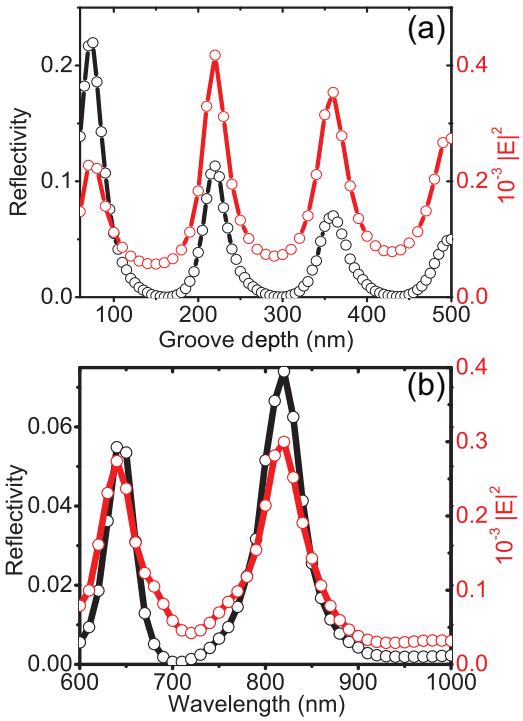

Figure 6.3: *FDTD calculations (black) of the reflectivity for surface plasmons incident perpendicularly onto a groove structured into a gold surface as a function of groove depth. Electric field intensity integrated over the area A of the groove as calculated from BEM (red). (a) Calculations as a function of groove depth at a free-space wavelength of 640 nm for a 25 nm wide groove; (b) Calculations as a function of wavelength for a 500 nm deep, 25 nm wide groove.*

the Poynting vector is directed towards the groove and energy is transmitted into the groove. This is a clear sign of coupling of planar surface plasmons to a localized mode confined in the groove.

To further investigate the relation between enhanced reflectivity and coupling of SPPs to groove modes, we have compared the field inside the groove to the reflectivity. Figure 6.3(a) shows the reflectivity as a function of groove depth at a free-space wavelength of 640 nm (a horizontal cross-cut in Fig. 6.1). Also plotted is the electric field intensity integrated over the area of the groove and then normalized to the groove area. As can be seen, maximum reflectivity and maximum field intensity are observed at the same groove depth. In Fig. 6.3(b) we show reflectivity and average field intensity for a fixed groove depth of 500 nm as a function of wavelength for a 25 nm wide groove. Here too, the the calculated wavelengths of the maximum in both

curves agree very well. From the data in Fig. 6.3 we can conclude that the increased reflectivity is related to efficient coupling of the incident planar SPPs to resonant groove modes.

On resonance, surface plasmons are coupled into the groove to excite the localized groove mode. The re-radiation of the energy stored in the groove cavity into forward and backward emission is observed as transmission and reflection, respectively. In this model, the coupling of the incident plasmon wave with the resonant groove mode is similar to Rayleigh scattering of a plane wave with a point dipole, that leads to forward and backward radiation. In the limit of complete coupling of the incident SPP into a small groove, and no groove cavity losses, a maximum reflection of 50% would be observed.

The phase difference between the SPPs transmitted trough the groove and the directly transmitted SPPs is determined by the groove geometry. If the groove geometry could be designed such that those two parts are equal in magnitude but are out of phase, the transmission will vanish and full reflection will be observed. This condition is similar to critical coupling observed for optical microcavities [70].

6.4 Coupling to groove modes

The coupling between the propagating plasmon and the localized groove mode becomes more clear when we investigate the depth-profile of the observed groove mode field. In Fig. 6.4 we plot the electric field intensity profile along a line in the center of the groove (a vertical cross-cut through Fig. 6.2) for different wavelengths and as a function of position. The groove depth was 500 nm, the groove width 25 nm, and the field was normalized to its maximum value for each wavelength. The wavelengths of maximum groove reflectivity (see Fig. 6.3) are marked as dashed lines in the graph. For each wavelength a standing wave pattern is observed with the position of high field intensity moving upwards for increasing wavelength. For the marked wavelengths of maximum reflectivity, a maximum of the electric field intensity reaches the upper end of the grooves. The increased field at the groove opening enables efficient coupling of incident SPPs to the standing groove mode. The higher intensity at the bottom of the grooves for all wavelengths is due to the stronger confinement of the plasmons as the grooves becomes narrower (see Fig. 6.1).

Propagating plasmon modes inside narrow grooves are known as channel plasmon polaritons (CPPs) [12, 71]. The standing groove modes observed here are the special case of CPPs for $k_z = 0$, where k_z is the wavevector along the propagation direction along the length of the groove (i.e. normal to the plane of the cross section in Fig. 6.2). Using BEM calculations we determined the local density of states (LDOS) as a function of wave vector and frequency inside the groove. A groove mode appears as a maximum in the LDOS. We have determined the wavelength of maximum LDOS for each wavevector to obtain the groove mode dispersion relation. In Fig. 6.5(a) we show the dispersion relation for 300 nm and 500 nm deep grooves with a width of 25 nm. Also plotted is the planar SPP dispersion and the light line in air. We observe flat

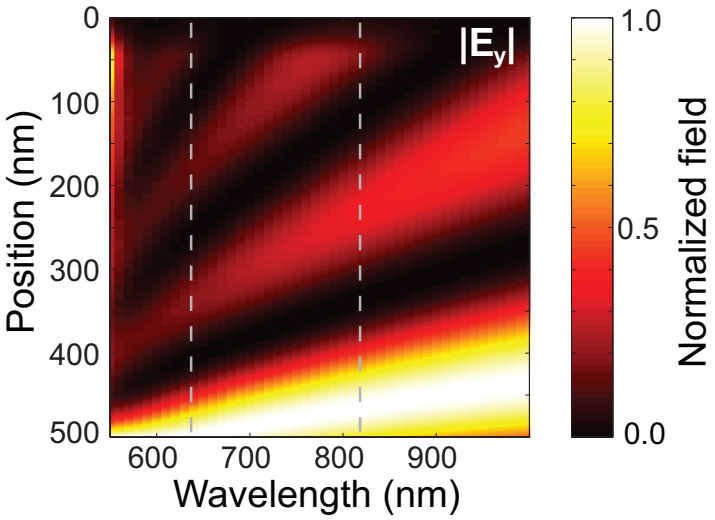

Figure 6.4: *Calculated electric field along a line in the center of a groove as a function of wavelength and position for a 500 nm deep, 25 nm wide groove in gold. For each wavelength the field was normalized to its maximum. The dashed lines indicate the wavelengths of maximum reflectivity from Fig. 6.3(b).*

dispersion bands starting at $k = 0$ and crossing the light line. While the low energy branches of the dispersion relation for the two depths overlap, higher-order-mode branches are well separated.

In the Fig. 6.5(b) we plot the reflectivity for the same groove depths as a function of wavelength. The crossings of the dispersion relation branches with the origin $k_z = 0$ agree very well with the observed maxima in reflectivity, indicating that for normal incidence the incoming plasmon is indeed coupled to a standing $k_z = 0$ wave inside the groove. Note that for non-normal incidence the plasmon can couple to a channel plasmon propagating along the groove. This case is not studied here.

The electric field intensity profile associated to each wavelength of maximum reflection is shown in Fig. 6.5(c) and (d). We observe the standing wave pattern for each mode with increasing mode number for decreasing wavelength.

6.5 Grooves as MIM cavities

The spectral width of the reflectivity maxima in Fig. 6.1 depends on the groove width. Broad- or narrow-band reflection can thus be obtained by tuning the groove width. To investigate the relation between groove width and resonance line width, we have modeled the grooves as cavities of metal-insulator-metal (MIM) plasmons. The

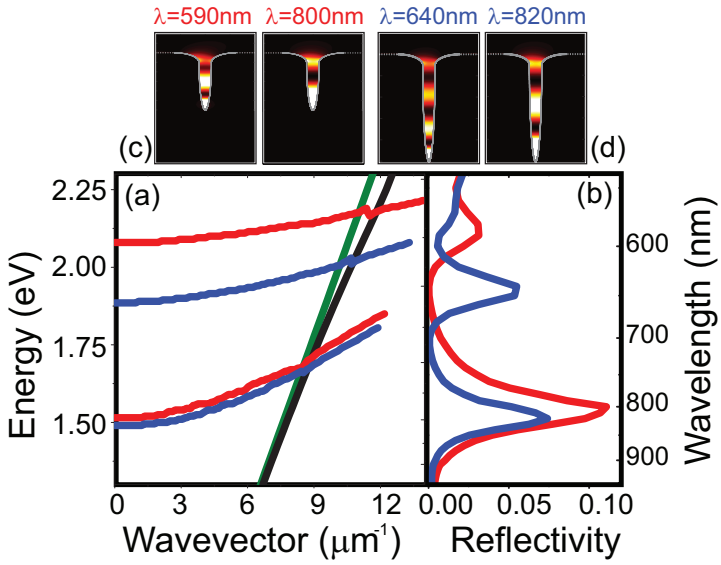

Figure 6.5: *(a) Dispersion relation for plasmons propagating in 300 nm (red line) and 500 nm (blue line) deep grooves with a width of 25 nm calculated using BEM. Light line in air (green) and single Au/air interface SPP dispersion (black). (b) FDTD calculations of the reflectivity as a function of wavelength for SPPs incident perpendicular onto a 300 nm (red line) and 500 nm (blue line) groove. (c) Electric field intensity inside a 300 nm deep groove at wavelengths of maximum reflectivity (590 and 800 nm) . (d) Electric field intensity inside a 500 nm deep groove a wavelengths of maximum reflectivity (640 and 820 nm).*

width of the observed resonances is determined by the cavity quality factor Q which describes the cavity losses. The cavity losses can be separated into losses which occur due to non-unity reflectivity at the cavity ends and due to the propagation loss of a plasmon inside the cavity due to Ohmic losses.

To determine the propagation losses we have used the analytical solution for the MIM dispersion relation [72]. The propagation loss was calculated from the imaginary part k_i of the wave vector. As expected, for the same frequency we observe a larger real part of the wave vector and higher losses for the 25 nm wide waveguide than for the 100 nm wide waveguide. To determine the reflectivity of the open and closed end of the groove we have performed FDTD calculations. For each groove width an MIM plasmon mode was injected into a MIM waveguide, with the spacing between the metal interfaces equal to the groove width. The MIM waveguide was terminated either with an open or closed end with equal shape as the groove ends, and the reflection from the end was monitored. While at the closed end a higher value of reflectivity is

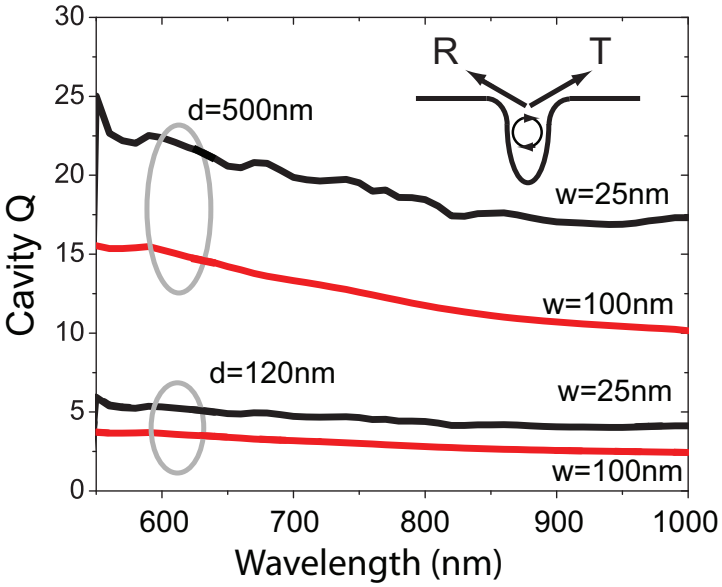

Figure 6.6: *Cavity quality factor Q for 25 nm (black) and 100 nm (red) wide grooves with depths of 120 nm and 500 nm. Q was calculated from FDTD calculations of the groove end reflection coefficients and propagation losses for MIM plasmons.*

found for the 100 nm waveguide ($\sim 91\%$) compared to the 25 nm waveguide($\sim 72\%$), at the open end the reflectivity is higher for the 25 nm waveguide ($\sim 51\%$) compared to ($\sim 21\%$) for 100 nm.

The quality factor of the cavity Q is defined by the ratio between the energy stored in the cavity and the energy loss per optical cycle. Equivalently, the quality factor is determined by the round trip time and the fractional energy loss per cavity round trip. The energy loss ΔI per cavity round trip for a groove with depth d can be estimated as $\Delta I = I_0(1 - R_o R_c exp(-4k_i d))$, where R_o and R_c are the reflectivity at the open and closed ends, respectively. With the calculated propagation and reflection losses we have determined the theoretical Q for cavities with depths of 100 nm and 500 nm and widths of 25 nm and 100 nm; the results are shown in Fig. 6.6 as a function wavelength. The highest cavity quality factor $Q = 25$ is observed for 25 nm wide and 500 nm deep grooves. The fact that for the same width a higher Q is observed for deeper grooves indicates that the cavity losses are dominated by the reflectivity losses. The values of the cavity Q for 25 nm wide and 500 nm deep grooves agree reasonably well with the line width observed in Fig. 6.3(b). The higher calculated Q for the narrower cavity is in good agreement with the observed smaller resonance width in the reflectivity plots of Fig. 6.1 and is thus related to the higher cavity mode reflectivity for narrower cavities.

6.6 Conclusions

In conclusion, we have shown that single linear grooves in a planar gold surface can exhibit high reflectivity for incoming surface plasmon polaritons. The observed reflectivity shows resonances depending strongly on wavelength, groove depth and width and a maximum reflectivity of 29% is observed. The observed resonances in reflectivity can be attributed to coupling with localized SPP modes inside the groove cavity. The highest cavity quality factor Q for the studied geometries is $Q = 25$. By engineering the coupling phase between incoming SPP and the groove resonance higher reflectivity may be obtained. These results are important to design suitable grooves acting as efficient reflectors for surface plasmons.

7

Surface plasmon in a box

Surface plasmon polaritons (SPPs) on gold were confined to rectangular plateaus bounded by grooves. We used cathodoluminescence spectroscopy to image the SPP modes of the plateaus. Measurements were reproduced using a two-dimensional image source model for the local density of states.

7.1 Introduction

The first images of the electronic local density of states inside a quantum corral raised great interest in scanning tunneling microscopy [73]. This was followed shortly after by the predictions [74] and measurements [75] of a similar effect for light in optical corrals. Surface plasmons polaritons (SPPs) are light waves bound to the interface between a metal and a dielectric [1]. They are collective oscillations of the conduction electrons in the metal that oscillate in unison with the electromagnetic field.

One-dimensional confinement of SPPs in Fabry-Perot type resonators has been demonstrated using two parallel Bragg-gratings [56] or grooves (chapter 5) as reflectors. Surface plasmons are confined in these structures only if their path is perpendicular to the mirror plane, they can escape on paths with components parallel to the reflectors. Drezet *et al.* used arrays of nanoparticles to confine SPPs to elliptical corrals, thereby, completely restricting the SPP propagation in the plane [55]. Due to the size of the ellipses and the used observation techniques SPPs but no confined plasmon modes were observed in their experiments.

In this chapter, we use grooves structured into the surface of a single-crystalline gold substrate to confine SPPs in two dimension, using box-shaped plateaus. We use cathodoluminescence imaging spectroscopy [27, 28] to excite SPPs in the boxes and spatially resolve the mode profiles. The observed SPP modes are similar to those of a two-dimensional particle-in-a-box and are formed by SPPs reflected at the boundaries. We find good agreement with calculations of the two-dimensional local density of states for SPPs inside the boxes.

7.2 Experimental

We used a single-crystal Au pellet of 1 mm thickness (effectively semi-infinite for optical fields) as substrate. The surface of the gold pellet was chemically polished down to nanometer roughness. Into the surface we structured rectangular and square boxes bounded by grooves using a 30 keV Ga^+ focused ion beam. The grooves were 120 nm deep and 100 nm wide as was determined from cross-sections made using focused ion beam milling and imaged by scanning electron microscopy (SEM). This groove geometry leads to optimum SPP reflectivity due to the resonant excitation of localized groove modes as described in chapter 6. The side length of the boxes was varied in the range from 0.5-2.0 μm. In Fig. 7.1(a) a schematic of the samples is depicted and in (b) a SEM image of a 1×1 μm box is shown.

We used spatially-resolved cathodoluminescence spectroscopy to image the modes of the boxes. We have measured the emission generated by the 30 keV electron beam from a field-emission source focused in a SEM onto the sample. The scanning electron beam passes through a hole in a parabolic mirror that is positioned above the sample and is focused onto the sample to a ~ 5 nm diameter spot. The electron beam is a point source for SPPs in a broad spectral range. The mirror collects light emitted from the sample with an acceptance solid angle of 1.42 π. The light is then focused

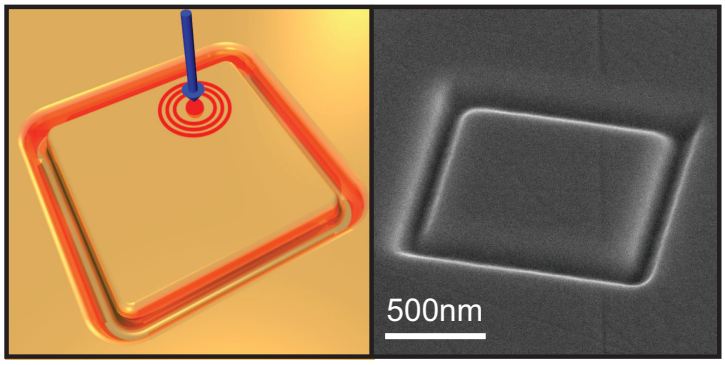

Figure 7.1: *(a) Schematic of of the structure under investigation. The electron beam is shown as a blue arrow that excites surface plasmons (b) Top-view SEM image of a* 1×1 *µm box bounded by 120 nm deep grooves structured into the surface of a single-crystal gold pellet.*

onto the entrance slit of a monochromator and spectrally resolved using a CCD array detector (bandwidth $\approx$ 10 nm). The uncorrected experimental count rate was 100-2000 counts per second per wavelength channel at an electron beam current of 30 nA. We corrected the measured spectra for system response using a calibration spectrum determined by dividing the transition radiation spectrum collected from a planar Au sample (no grooves) by the calculated transition radiation spectrum for 30 keV electron-irradiated Au [34].

CL spectra were measured as a function of electron beam position in a square grid with a step size of 30 nm and 1 s integration time. Figure 7.2(a) shows the CL spectrum integrated over the entire box area for a scan of a box with dimensions of $1 \times 1\mu$m. The spectrum shows broad emission spanning the wavelength range from the SPP resonance around 540 nm to the near-infrared. Two main peaks are observed, a broad peak at approximately 590 nm with a small shoulder at slightly lower wavelength and a clear peak at 670 nm. Additionally, the faint shoulders are observed around 800 nm, 850 nm and 900 nm.

In Fig. 7.2(b) we show the spatially resolved CL signal for the wavelengths of 550 nm, 670 nm, and 850 nm. At each position the spectra were binned 5 nm around the central wavelength. The grooves bounding the box are clearly visible for all wavelengths as lines of reduced CL emission. Inside the box on the plateau we see a pattern of minima and maxima of the CL emission. For 550 nm three maxima in x- and y-direction can be observed. The number of maxima decreases to two in each direction for 660 nm and to one in the center for 850 nm. The observed higher intensity in the lower part of the images is probably due to the asymmetry in the detection system.

The observed patterns show that SPP modes, which are confined by the grooves, are excited on the plateau. The reflection of SPPs on the grooves leads to a standing

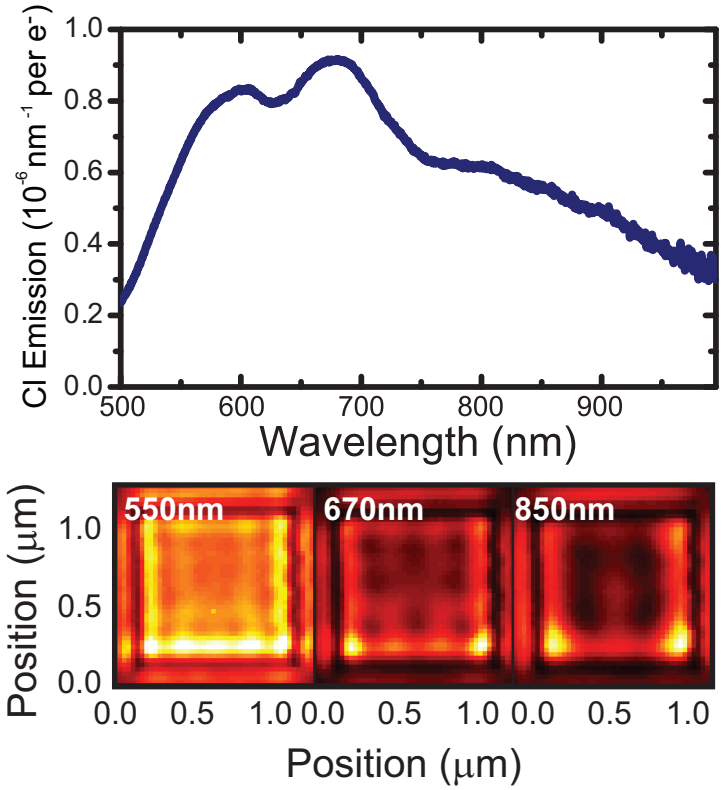

Figure 7.2: *(a) Spectrum of cathodoluminescence detected from the plateau of a* $1 \times 1\,\mu m$ *box, bounded by 120 nm deep and 100 nm wide grooves, integrated over the box. The data was corrected for the system response. (b) Cathodoluminescence images (30 keV electrons) of a* $1 \times 1\,\mu m$ *box (groove width 100 nm, groove depth 120 nm) for four wavelengths of 550, 670, and 850 nm.*

wave pattern if the condition for constructive interference is fulfilled: $2L_{x,y}k_{SPP} + 2\phi = 2\pi n_{x,y}$ with $L_{x,y}$ the cavity length in x,y direction, k_{SPP} the SPP wave vector, ϕ a phase shift upon reflection and $n_{x,y}$ the mode numbers in each direction. We assigned mode numbers to the wavelengths for which a pattern was observed. Assuming $\phi = 0$, we find $n_{x,y} = (4,4)$ for 550 nm, $n_{x,y} = (3,3)$ for 670 nm, and $n_{x,y} = (2,2)$ for 850 nm. Note, that the spatial resolution in CL spectroscopy results from the known profile of the exciting electron beam. The intensity variations in the radiation that are observed in the far-field are due to the fact that the electron preferentially excites SPPs at positions of maximal electric field amplitude *i.e.* the antinodes of the mode pattern.

Due to symmetry the mode numbers for square boxes are equal for the axis. For

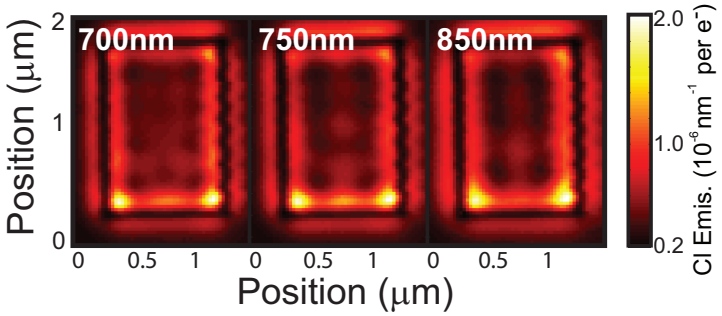

Figure 7.3: *Cathodoluminescence images (30 keV electrons) of a rectangular plateau with dimensions of* 1.0×1.5 μm. *The CL images are taken for wavelengths of 700, 750, and 850 nm.*

an asymmetric box the number of maxima along each axis and therefore the mode numbers will differ between the short and long axis. To show this we have performed CL measurements on a rectangular box with dimensions of 1.0×1.5 μm. In Fig. 7.3 we show the CL emission maps at wavelengths of 700 nm, 750 nm, and 850 nm. For a wavelength of 700 nm we observe two antinodes along the horizontal axis and three along the vertical axis equivalent to mode numbers of $n_{x,y} = (3, 4)$. For the 750 nm emission the mode number in horizontal direction decreases and only a single maximum is observed: $n_{x,y} = (2, 4)$. For the 850 nm CL emission only two maxima are observed along the vertical axes: $n_{x,y} = (2, 3)$.

7.3 LDOS model

To model our results we use a two-dimensional model of the local density of states (LDOS). The generation of SPPs by the electron beam is modeled with a point source. The reflections at the grooves are represented by image sources with relative strengths corresponding to the reflectivity of the groove. In the image source model the reflectivity is angle-independent, while in the experiment the reflectivity is angle-dependent due to coupling to metal-insulator-metal modes propagating along the V-grooves (see chapter 6). Figure 7.4 shows the wavelength dependent reflectivity for a 120 nm deep and 100 nm wide groove determined using finite-difference-in-time-domain calculations for a plasmon at normal incidence (see chapter 6). The reflectivity for this groove depth is maximum for a wavelength at 670 nm. This is in agreement with the observation that the visibility of resonances in Fig. 7.2(a) is most pronounced around 700 nm.

To determine the LDOS we evaluate the Green's function $G(\mathbf{r}, k)$ of the original source at the position $\mathbf{r} = (x, y)$ and four image sources located at $\mathbf{r_1} = (L_x - x, y)$, $\mathbf{r_2} = (-L_x - x, y)$, $\mathbf{r_3} = (x, L_y - y)$, and $\mathbf{r_4} = (x, -L_y - y)$. The Green's function for a SPP point source in two dimensions is given by $G(\mathbf{r}, k) = -1/(2\pi)K_0(ik_{SPP}|r - r'|)$,

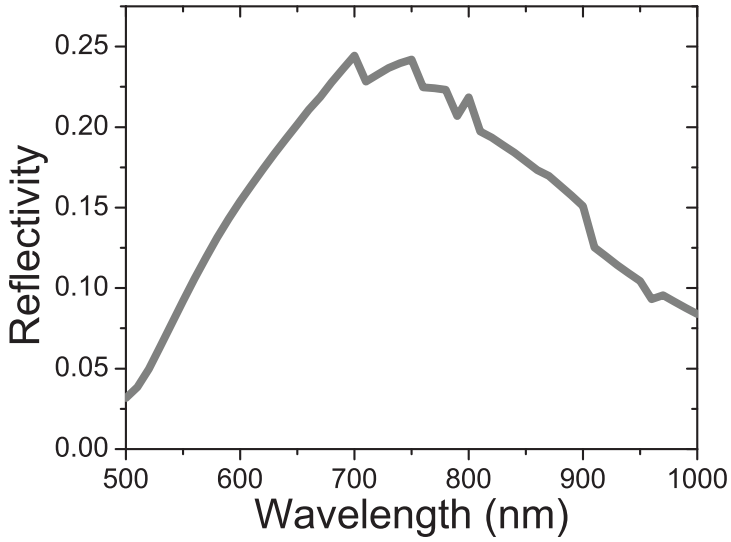

Figure 7.4: *Reflectivity as a function of wavelength for surface plasmons incident perpendicularly onto a groove structured into a gold surface from FDTD calculations. The groove depth was 120 nm and the groove width was 100 nm.*

with K_0 the modified Bessel function of second kind. We determine the Green's function of the entire system by summing up the terms for the image sources and the original source. Taking the imaginary part of the Green's function then gives the LDOS for the system.

In Fig. 7.5 we show the calculated LDOS inside a 1×1 μm box for the three wavelengths at which the CL images in Fig. 7.2(b) were taken. For 550, 670, and 850 nm we observe good overall agreement of the LDOS model and the measured pattern. The number of anti-nodes in each direction is well reproduced. The fact that a lower visibility of the mode pattern is observed in experiment may be due to the limitation that a angle-independent groove reflectivity was not taken into account.

We have also calculated the LDOS for a rectangular box with dimensions of 1×1.5 μm. The results are shown in Fig. 7.6 for wavelengths of 700, 750, and 850 nm. For all wavelengths the calculations reproduce the overall pattern observed in the measurements shown in Fig. 7.3.

7.4 Conclusions

In conclusion, we have determined the modal distribution of surface plasmon polaritons confined by grooves to square and rectangular plateaus in single-crystalline gold using cathodoluminescence imaging spectroscopy. The confined SPPs form standing

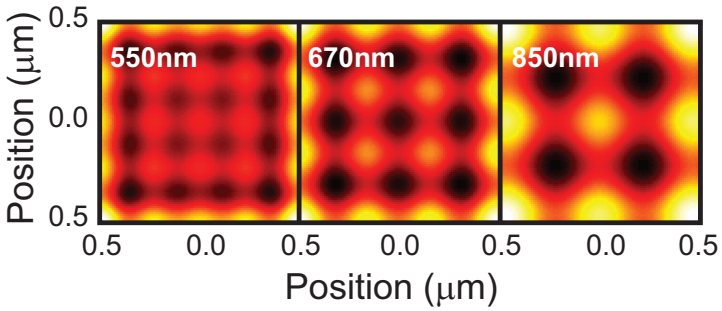

Figure 7.5: *Local density of states for surface plasmon polaritons on a* 1.0×1.0 *μm sized, square plateau in gold as a function of position. The LDOS was calculated using a two-dimensional image source model for the wavelengths of 550, 670, and 850 nm.*

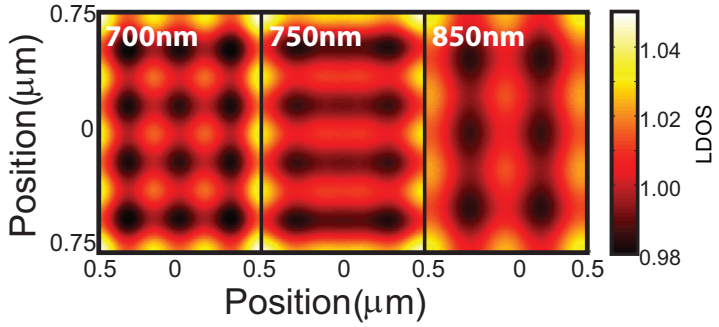

Figure 7.6: *Local density of states for surface plasmon polaritons for a* 1×1.5 *μm sized, rectangular plateau in gold as a function of position. The LDOS was calculated using a two-dimensionl image source model for the wavelengths of 700, 750, and 850 nm.*

wave patterns that are well reproduced by a two-dimensional image source model that relates the CL intensity to the local density of states. The data demonstrate that two-dimensional confinement of surface plasmon polaritons can be achieved in these cavities with a high degree of control over the localization of the field intensity by tuning the wavelength.

8

Cathodoluminescence imaging spectroscopy of plasmonic metal-insulator-metal modes

Cathodoluminecence imaging spectroscopy is used to excite and characterize the resonant modes of Fabry-Perot resonators for surface plasmon polaritons confined in a metal-insulator-metal geometry. From the observed mode pattern we derive the MIM plasmon wavelength which is found to be 227 nm in cavities with a 30 nm SiO_2 layer for a free-space wavelength of 600 nm. The measured wavelength agrees well with values from analytical dispersion relation calculations. We also present measurements of MIM plasmon modes confined to disc resonators with mode volumes as small as $V = 0.04\lambda_0^3$. Calculations of the excitation probability show that resonant excitation of MIM plasmons depends strongly on the electron energy due to phase retardation effects resulting from the finite electron velocity.

8.1 Introduction

Surface plasmon polaritions (SPPs) are electromagnetic waves that propagate at the surface of a metal. Their evanescent field tail typically extends several 100 nm into the dielectric. Near the surface plasmon resonance, SPPs are highly dispersive enabling short plasmon wavelengths at optical frequencies.

The dispersion of plasmons can be further enhanced in metal-insulator-metal (MIM) geometries, in which the plasmon field is confined in a 10-100 nm dielectric gap between two metal layers. Due to the coupling of plasmons at both metal-dielectric interfaces, plasmon modes with symmetric and antisymmetric magnetic field distribution exist, of which the latter show the largest dispersion and highest loss [72].

Due to their unique properties, MIM plasmons are currently a research topic of great interest. The propagation of MIM modes in waveguides was measured in the far-field [76] and the dispersion was determined using near-field microscopy [77]. Two-dimensional negative refraction of plasmons has been demonstrated in the visible [18], and was also confirmed theoretically [19]. In these studies, MIM plasmons were excited by an external light source using incoupling through slits in one of the metal cladding layers.

In this chapter, we present cathodoluminescence spectroscopy measurements of MIM plasmon modes. We use the electron beam of an SEM that travels through the layer stack to directly excite MIM plasmons confined in resonator structures. Measurements of the mode structure in Fabry-Perot and disc resonators allow us to determine the MIM plasmon wavevector. The found wave vectors agree well with analytical calculations of the dispersion relation.

8.2 Experimental

The MIM samples were prepared using physical vapor deposition from a thermal evaporation source onto a cleaned silicon substrate. The layer stack consisted of subsequent layers of 10 nm chromium, 100 nm silver, 30 or 50 nm silica, 100 nm silver and 10 nm chromium. A control sample was evaporated at the same time and shielded by a shutter during the silica evaporation leaving it without the SiO_2 layer.

The 30 keV Ga^+ beam of a focused ion beam system was used to structure outcoupling and resonator structures into the MIM stack. The focused ion beam (beam current 48 nA) etched through the entire layer stack and approximately 200 nm into the underlying silicon substrate. Figure 8.1(a) shows a SEM image of a Fabry-Perot resonator structured into a layer stack with a 50 nm SiO_2 layer imaged under an angle of 52° off the surface normal. The one-dimensional cavity is formed by two parallel grooves of 1000 nm width that are spaced by a distance of 2000 nm. The groove length is 5000 nm. The silicon substrate, the metal layers and the silica can be easily identified. The contrast between silver and chromium is too small to see in the image. Figure 8.1(b) shows the SEM image of a circular resonator bounded by a 1000 nm wide groove, with a cavity plateau diameter of 2000 nm.

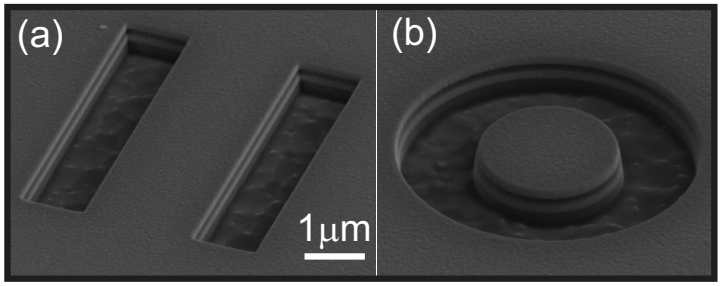

Figure 8.1: *(a) Scanning electron microscopy (SEM) image of a one-dimensional Fabry-Perot resonator in a MIM structure. The grooves were structured using focused-ion-beam milling and were 1000 nm wide and 5000 nm long. The spacing between the grooves is 2000 nm. (b) SEM image of a MIM disc resonator bounded by a 1000 nm wide groove. The disc diameter was 2000 nm.*

We used spatially-resolved cathodoluminescence imaging spectroscopy to excite plasmon modes in the MIM structures and measure the emission in the farfield. The samples were excited by the 30 keV electron beam of an SEM which was focused to a 10 nm spot onto the sample surface. Due to electron scattering in the upper metal layers the beam diameter is increased as it penetrates into the layer stack. Figure 8.2 shows the result of a Monte-Carlo simulation of the electron beam profile assuming a 10 nm diameter incident beam, determined at the center of the SiO_2 layer. As can be seen, the beam diameter is approximately 50 nm. A parabolic mirror (acceptance angle 1.4 π *sr*) placed above the sample collects the light emitted from the sample and guides it to a spectrometer. In the spectrometer the light is spectrally resolved and detected using a liquid-nitrogen cooled CCD array. The detected spectra were corrected for system response as described in chapter 2 by measuring the transition radiation spectrum for a known gold sample and normalizing it to the calculated transition radiation spectrum.

8.3 Fabry-Perot resonators

Figure 8.3 shows the CL emission as a function of wavelength and electron beam position for a line scan across three Fabry-Perot resonator structures: (a) the control sample without silica layer, (b) the MIM stack with 50 nm SiO_2 layer, and (c) the stack with 30 nm SiO_2 layer. In all three scans the grooves are clearly resolved at top and bottom of the image as areas of low emission. The emission is typically a factor of two higher if the beam is pointed onto the area between the grooves.

For the control sample in Fig. 8.3(a) a very weak periodic pattern of emission is observed between the grooves which is symmetric around the center of the plateau. The amplitude of the oscillation decreases away from the grooves towards the center

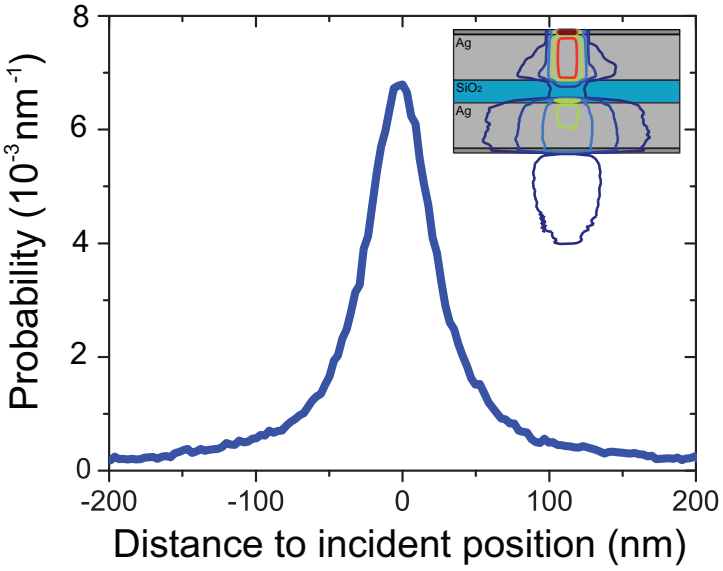

Figure 8.2: *Electron probability as a function of position for 30 keV electrons in the center of the silica layer of the MIM structure. The electron distribution was calculated using a Monte-Carlo simulation. The inset shows a contour plot of the lateral electron straggle (5%, 10%, 25%, 50% 75%, and 90% intensity contours).*

and close to the center only a diffuse pattern is observed. The period of the oscillations increases linearly with increasing wavelength and is approximately half the measurement wavelength.

The measurement of the MIM sample with 50 nm silica layer (Fig. 8.3(b)) shows an intenser oscillatory pattern. Seven bands of higher emission are observed for wavelengths of 610 nm, 640 nm, 680 nm, 730 nm, 780 nm, 850 nm and 920 nm. The emission from the center of the resonator at these wavelengths shows oscillations with a period that is much shorter than the detection wavelength. The amplitude and visibility of the oscillations in each wavelength band strongly decrease for shorter detection wavelength. Near the edges, a larger-period oscillation is observed as was vaguely visible in Fig. 8.3(a).

The MIM sample with 30 nm silica layer (Fig. 8.3(c)) shows eight bands of high emission at 600 nm, 630 nm, 660 nm, 695 nm, 740 nm, 790 nm, 850 nm, and 920 nm. The period of the oscillations for these wavelength bands is slightly shorter than for the 50 nm structure.

The observed CL emission of the measured samples stems from three sources that have to be taken into account: transition radiation, radiation from SPPs propagating at the Ag/Cr interface, and radiation from MIM plasmons.

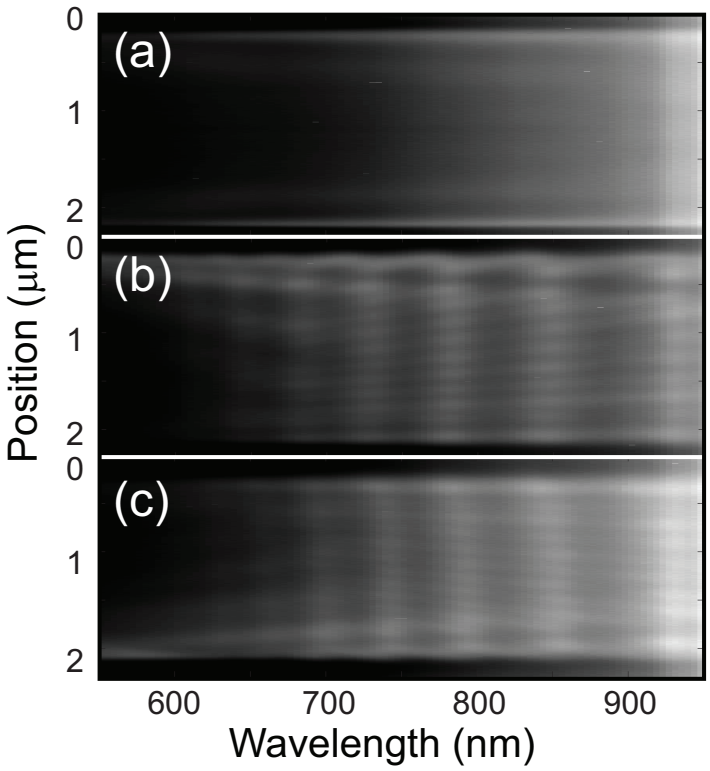

Figure 8.3: *Cathodoluminescence intensity as a function of position and wavelength for line scans across three $Ag/SiO_2/Ag$ MIM Fabry-Perot resonators with 2000 nm groove separation. The grooves were 1000 nm wide. (a) control sample without silica layer, (b) MIM structure with 50 nm silica layer, and (c) MIM structure with 30 nm silica layer.*

The transition radiation contribution was determined by measuring the CL emission at a sample position where no structures are present that could scatter plasmons. The transition radiation spectrum is very similar for all three samples showing that it is mainly influenced by the uppermost layer.

As we have shown in chapter 3, SPPs that are excited on the surface by the electron beam and are scattered out by a groove, will interfere with the coherently generated transition radiation. This leads to oscillations in the CL emission that dampen out for increasing distance from the groove.

To damp out single-interface SPPs propagating at the surface the chromium layers were deposited. Figure 8.4 shows the propagation length as a function of wavelength for the two MIM modes in comparison to the SPP mode propagating on the top interface calculated using a vectorial finite-difference mode solver included in a com-

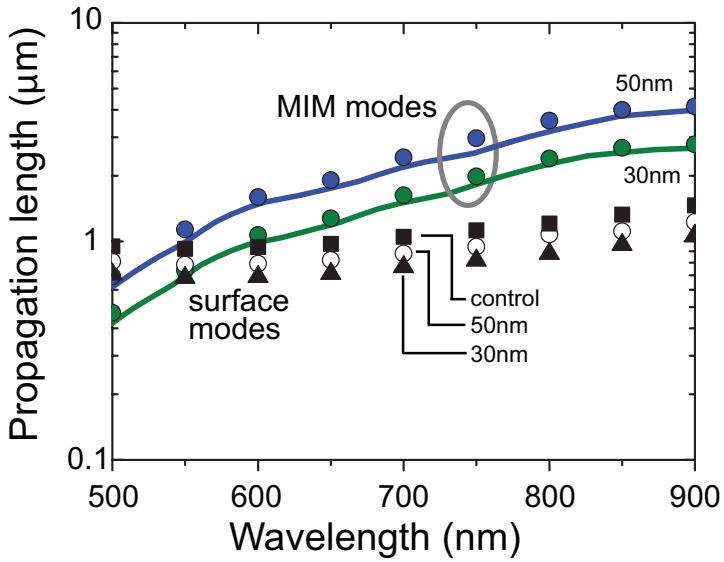

Figure 8.4: *Calculated propagation length as a function of wavelength for MIM and surface SPP modes for samples with 50 nm or 30 nm silica layer and a control sample. Symbols are calculated using a vectorial finite-difference mode solver, drawn lines are calculated from a analytical solution of the dispersion relation.*

mercial computation package [78]. We have also plotted the propagation length for the MIM modes calculated using the analytical solution for the dispersion relation [72]. The propagation length for the top SPP modes varies only slightly depending on the underlying layer stack. For the longest wavelengths it is by a factor of 3 lower than the propagation length for the MIM modes.

First, we analyze the measurements of the control sample. The oscillations close to the grooves are attributed to interference of scattered SPPs with transition radiation. The fact that only one oscillation is observed (rather than the extensive pattern in Chapter 3) is due to the fact that the propagation length of the surface SPPs is less than 1 μm. Due to the strong damping no standing SPP waves can form on the plateau as observed in chapter 5.

The MIM sample with the 50 nm SiO_2 layer also shows these oscillations near the edges, but in addition clear oscillations with a period much shorter than half the free-space wavelength. We attribute these to Fabry-Perot modes of MIM plasmons that are reflected between the grooves.

To analyze the data, we have determined the period of the observed oscillations by fitting the CL intensity as a function of position x for each band with a function $\propto \sin^2(k_{MIM}x)$ with $k_{MIM} = 2\pi/\lambda_{MIM}$ the MIM plasmon wavevector. We find plasmon wavelengths of 330, 350, 370, and 430 nm for the wavelength bands at 730, 780,

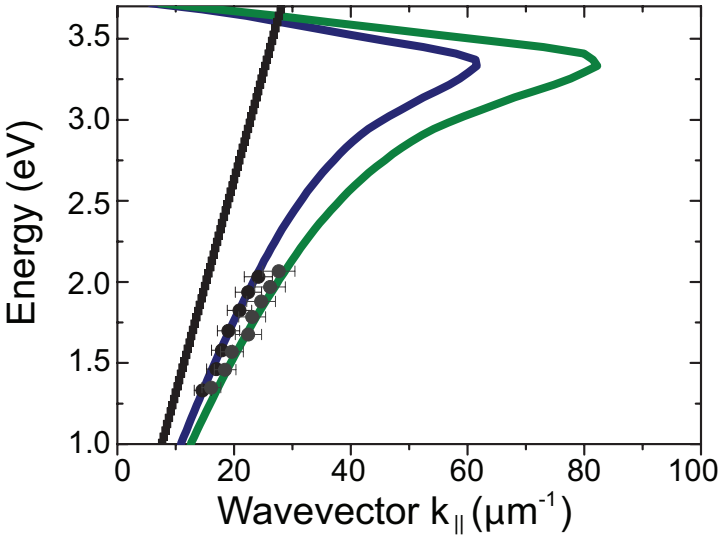

Figure 8.5: *Dispersion relation for symmetric $Ag/SiO_2/Ag$ MIM plasmons with 30 nm (green line) and 50 nm silica layer (blue line). The dots are derived from the cathodoluminescence line scans. The drawn lines are analytical calculations based on measured dielectric constants. The light line in silica is drawn in black.*

850, and 920 nm, respectively. For the bands at shorter wavelengths the oscillations are damped out too strongly to fit the period. However, we can still derive the MIM plasmon wavelength for these bands from their mode number.

Each band of high emission in the CL scans corresponds to a cavity mode with a successive mode number n given by $2dk_{MIM} + \phi = 2n\pi$ where d is the resonator width and ϕ is the phase change upon reflection (we assume $\phi = 0$). For the above identified bands we find mode numbers of $n = 9$ (920 nm), $n = 10$ (850 nm), $n = 11$ (780 nm), and $n = 12$ (730 nm). Therefore, the subsequent lower-wavelength bands should have the mode numbers $n = 13$ (680 nm), $n = 14$ (640 nm), and $n = 15$ (610 nm). Given the resonator width we can then derive the corresponding MIM plasmons wavelength of 305, 285, and 266 nm.

The MIM sample with 30 nm silica layer shows eight bands of high emission corresponding to eight modes of the Fabry-Perot resonator. The bands are more closely spaced, corresponding to a smaller free-spectral range which is in agreement with the shorter plasmon wavelengths expected for this sample. The stronger damping of the plasmons in this sample compared to the 50 nm silica sample leads to a smaller oscillation amplitude. Due to the stronger damping only the oscillation period of the three longest-wavelength bands can be fitted for this sample. We find plasmon wavelengths of 320 nm (780 nm), 340 nm (850 nm), and 390 nm (920 nm) equivalent to mode numbers of $n = 12$, $n = 11$, and $n = 10$, respectively. From the mode number

the plasmon wavelengths for the other bands are derived to be 227 nm (600 nm), 240 nm (630 nm), 255 nm (660 nm), 272 nm (695 nm), and 280 nm (740 nm).

Figure 8.5 shows the dispersion relation for the MIM modes for the 30 nm and 50 nm thick SiO_2 layers, with data points as derived above. The analytical dispersion relation is also plotted, calculated based on the optical constants for the layer stack measured using spectroscopic ellipsometry. The experimental data agree very well with the calculation and lie far to the right of the light line in silica demonstrating the strongly dispersive character of the MIM modes.

8.4 Disc resonators

Next, we measured the CL emission along a line scan across the center of a plasmonic MIM disc cavity as shown in Fig. 8.1(b). The plateau of the disc had a diameter of 2000 nm and was bounded by a 1000 nm wide groove. The measured CL signal for the control sample and the MIM samples with 30 nm, and 50 nm silica layer are shown in Fig. 8.6(a-c).

Similar to the Fabry-Perot resonator measurements we observe only a weak interference pattern for the control sample with a period of approximately half the free-space wavelength, which we attribute to the far-field interference of transition radiation and scattering from SPPs propagating on the top of the Ag film.

For the sample with the 50 nm silica layer we observe several bright bands with short oscillation period similar to the Fabry-Perot resonators. These oscillations are a sign of plasmonic MIM disc modes. MIM plasmons are reflected from the boundaries of the disc and interfere constructively or destructively depending on phase.

The sample with 30 nm silica layer shows oscillations with a smaller period and the observed bands are narrower. This is again in good agreement with the larger expected free spectral range due to the smaller plasmon wavelength for the smaller silica layer thickness.

Due to the very small dielectric layer thickness, the mode volume of plasmons confined in these cavities is extremely small. To investigate this, we have characterized a disc with a diameter of 1000 nm and observed a bright wavelength band at 840 nm for the 30 nm silica layer. At this wavelength the MIM plasmon wavelength is 337 nm. The mode volume of the plasmon cavity expressed in free-space wavelength is $V = 0.04\lambda_0^3$; when expressed in units of plasmon wavelengths it is $V = 0.61\lambda^3$.

The mode volumes for the measured disc resonators are similar to mode volumes observed for the smallest photonic crystal or dielectric Fabry-Perot cavities [79]. Smaller cavities can be designed to sustain only the lowest order mode for the shortest plasmon wavelength observed in the 30 nm Fabry-Perot resonator. The mode volume in this cavity will be $V_{min} = 0.026\lambda^3$ in units of plasmon wavelengths (227 nm) or $V_{min} = 0.0014\lambda_0^3$ in units of the free-space wavelength (600 nm), which is much smaller than for any classical dielectric cavity.

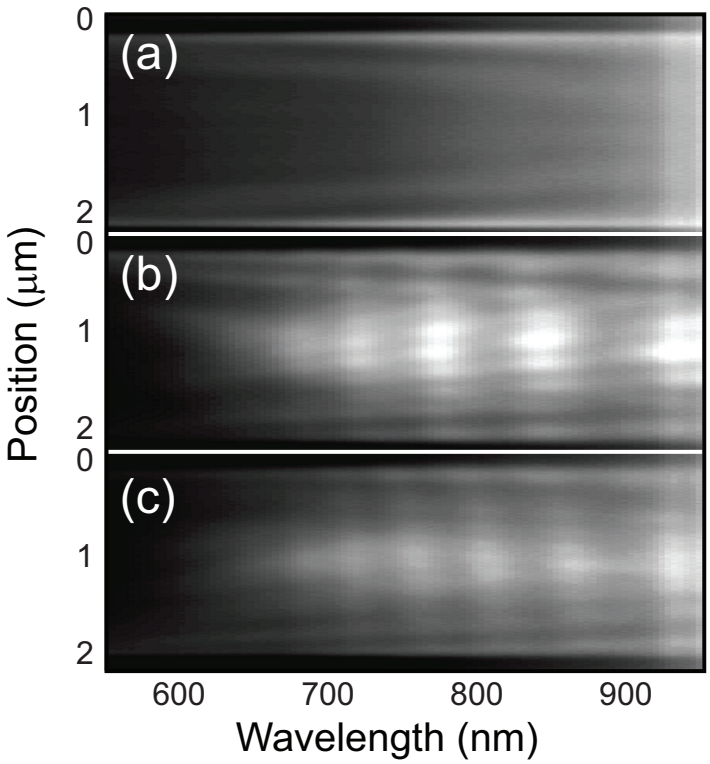

Figure 8.6: *Cathodoluminescence intensity as a function of position and wavelength for line scans across the center of $Ag/SiO_2/Ag$ MIM disc resonators with 2000 nm diameter. The discs were bounded by 1000 nm wide grooves. (a) control sample without silica layer, (b) MIM disk with 50 nm silica layer, and (c) MIM disk with 30 nm silica layer.*

8.5 Exitation probabilities of MIM modes

For the studied MIM cavities the incident electron crosses the boundary between the metal and silica twice, generating excitations at both metal-dielectric interfaces. Due to the finite velocity of the electrons, the plasmon fields excited at the two interfaces will have a phase difference $\Delta\phi$ depending on the thickness d of the silica core and the electron velocity v:

$$\Delta\phi = 2\pi \frac{d}{v} \frac{c}{\lambda} + \phi_0, \tag{8.1}$$

with λ the free-space wavelength. The phase factor ϕ_0 accounts for the phase difference between the plasmon fields generated at the electron transition from metal to dielectric and vice versa; for the MIM structure $\phi_0 = \pi$.

Figure 8.7 shows the calculated phase difference as a function of electron velocity at a free-space wavelength of 800 nm for three different silica layer thicknesses of 30, 50, and 100 nm. The phase difference increases inversely with decreasing electron velocity and linearly with layer thickness. The inset of Fig. 8.7 shows the schematic magnetic field profiles for the symmetric and antisymmetric MIM modes.

The phase difference leads to constructive or destructive interference between excitations on the two interfaces. The experimentally observed MIM modes are of symmetric character and have the highest field intensity in the dielectric core as shown in the inset of Fig. 8.7(a). Therefore, we expect a decrease in emission probability for symmetric MIM plasmon at phase difference of $\Delta\phi = (2n + 1)\pi$, with integer n (indicated by dashed lines in Fig. 8.7(a)).

At the marked positions, as well as in the limit of large v and small dielectric thickness a plasmon mode with antisymmetric magnetic field distribution (see inset Fig. 8.7) will be preferentially excited. We attribute the fact that this modes is not observed in our measurements to the fact that the propagation length for this mode is extremely short [72].

Similar to the calculations for the generation rate in chapter 2, the emission probability for the symmetric plasmon mode in an MIM cavity was calculated [80]. The results are shown in Fig. 8.7(b) as a function of electron velocity for silica layer thicknesses of 30, 50, and 100 nm. We observe a decrease in the excitation rate with decreasing electron velocity in agreement with higher localization of the external field of the electron. Superimposed on this decrease we observe dips in the emission probability for electron velocities at which the phase difference equals an odd number times π. Moreover, the number of the dips increases with layer thickness in agreement with Eqn. (8.1).

These calculations indicate that by varying the beam energy it is possible to selectively excite a plasmon mode with desired symmetry. For the studied samples the highest energy dips with reduced emission of symmetric MIM modes are found at very low beam energies: 0.37 keV for the 30 nm silica layer (blue curves) and 1.01 keV for the 50 nm silica layer (red curves). For these energies the inelastic mean free path in silver is very short (9 and 15 nm, respectively [81]) and the electron transmission through the upper silver layer is thus extremely low. For a silica layer thickness of 100 nm, a dip of reduced emission is found for an energy of 4 keV. In this case the inelastic mean free path for the electron is 43 nm.

Due to the constraint of reduced electron transmission through the silver layer at low energies it will be difficult to experimentally demonstrate selective excitation of certain plasmon symmetry. Another possibility is to tilt the sample with respect to the electron beam and thus increase the path length d through the silica layer. The fact that the excitation is generated at different lateral positions leads to an additional phase difference. The tilt required to achieve a minimum in symmetric mode excitation such as in Fig. 8.7(b) for electrons incident on a MIM structure with a 100 nm silica layer at 10 keV is 35° for a wavelength of 800 nm. For 30 keV electrons the sample has to be tilted to 51°.

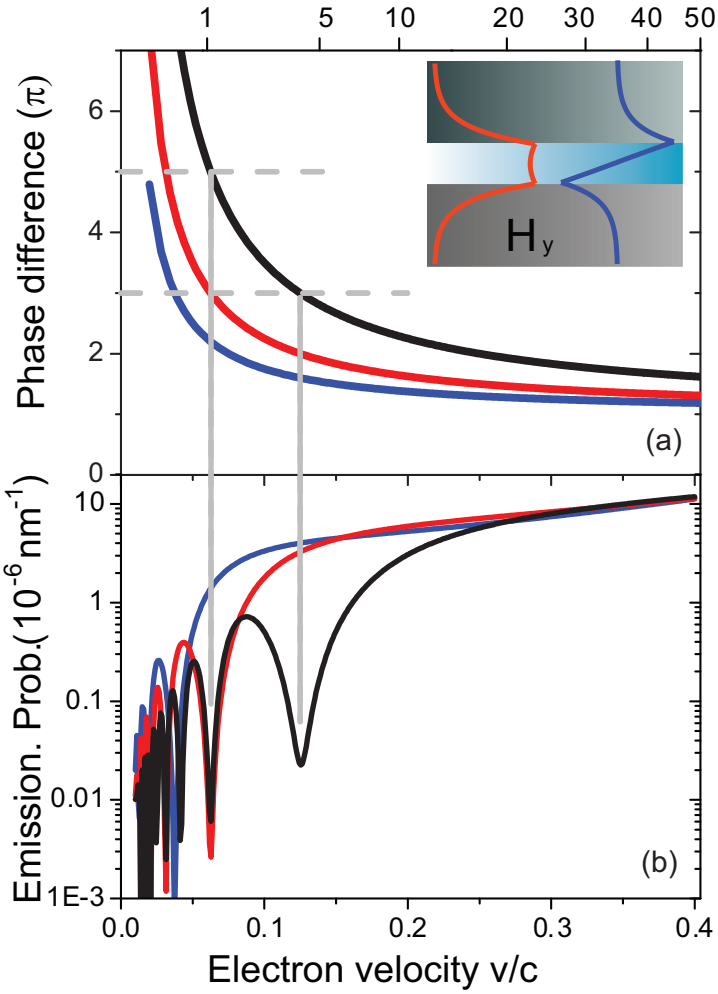

Figure 8.7: *(a) Phase difference for plasmon excitation (free-space wavelength 800 nm) by an electron passing through a metal-insulator-metal structure as a function of electron velocity. The phase difference was calculated for an insulator thickness of 30 nm (blue), 50 nm (red), and 100 nm (black line). The gray horizontal dashed lines denote phase differences of* $(2n+1)\pi$ *with integer* n*. Inset: H field profile for the symmetric (red) and antisymmetric (blue) MIM mode. (b) Plasmon emission probability as function of electron velocity for the symmetric MIM mode.*

8.6 Conclusions

We have shown that cathodoluminescence imaging can be used to excite and map plasmonic modes in $Ag/SiO_2/Ag$ MIM structures. The generated MIM plasmons were confined in Fabry-Perot and disc resonators. From the spatially resolved mode profile of the Fabry-Perot resonators the dispersion relation of the MIM plasmons was derived, and found to be in good agreement with theory. We have confined the light in plasmonic MIM disk resonators to mode volumes as small as $0.58\lambda^3$ when expressed in units of plasmon wavelength or equivalently $0.04\lambda_0^3$ when expressed in free-space wavelength. The smallest achievable cavity mode volume for a 30 nm SiO_2 MIM cavity is $0.0014\lambda_0^3$, much smaller than for any classical dielectric cavity. Finally, we have shown that excitation probability of resonant excitation of MIM plasmons depends strongly on the electron energy due to phase retardation effects resulting from the finite electron velocity.

Bibliography

[1] Raether, H. *Surface Plasmons on Smooth and Rough Surfaces and on Gratings.* Springer, (1988).

[2] Kretschmann, E. and Raether, H. *Radiative decay of nonradiative surface plasmons excited by light.* Z. Naturforsch. A **23**, 2135 (1968).

[3] Otto, A. *Excitation of nonradiative surface plasma waves in silver by the method of frustrated total reflection.* Z. Physik **216**, 398 (1968).

[4] Ritchie, R. H. *Plasma losses by fast electrons in thin films.* Phys. Rev. **106**, 874 (1957).

[5] Heitmann, D. *Radiative decay of surface plasmons excited by fast electrons on periodically modulated silver surfaces.* J. Phys. C **10**, 397 (1977).

[6] Kuttge, M., Vesseur, E. J. R., Verhoeven, J., Lezec, H. J., Atwater, H. A., and Polman, A. *Loss mechanisms of surface plasmon polaritons on gold probed by cathodoluminescence imaging spectroscopy.* Appl. Phys. Lett. **93**, 113110 (2008).

[7] Kano, H. and Kawata, S. *Surface-plasmon sensor for absorption-sensitivity enhancement.* Appl. Opt. **33**, 5166 (1994).

[8] Homola, J., Yee, S., and Gauglitz, G. *Surface plasmon resonance sensors: review.* Sens. Actuat. B **54**, 3 (1999).

[9] Homola, J. *Surface Plasmon Resonance Based Sensors.* Springer, (2006).

[10] Ferry, V. E., Sweatlock, L. A., Pacifici, D., and Atwater, H. A. *Plasmonic nanostructure design for efficient light coupling into solar cells.* Nano Lett. **8**, 4391 (2008).

[11] Berini, P. *Plasmon-polariton waves guided by thin lossy metal films of finite width: Bound modes of asymmetric structures.* Phys. Rev. B **63**, 125417 (2001).

[12] Bozhevolnyi, S. I., Volkov, V. S., Devaux, E., Laluet, J.-Y., and Ebbesen, T. W. *Channel plasmon subwavelength waveguide components including interferometers and ring resonators.* Nature **440**, 508 (2006).

[13] Charbonneau, R., Lahoud, N., Mattiussi, G., and Berini, P. *Demonstration of integrated optics elements based on long-ranging surface plasmon polaritons.* Opt. Express **13**, 977 (2005).

[14] Sandtke, M. and Kuipers, L. *Slow guided surface plasmons at telecom frequencies.* Nat. Photon. **1**, 573 (2007).

[15] Stockman, M. I. *Nanofocusing of optical energy in tapered plasmonic waveguides.* Phys. Rev. Lett. **93**, 137404 (2004).

[16] Verhagen, E., Polman, A., and Kuipers, L. *Nanofocusing in laterally tapered plasmonic waveguides.* Opt. Express **16**, 45 (2008).

[17] Miyazaki, H. T. and Kurokawa, Y. *Squeezing visible light waves into a 3-nm-thick and 55-nm-long plasmon cavity.* Phys. Rev. Lett. **96**, 097401 (2006).

[18] Lezec, H. J., Dionne, J. A., and Atwater, H. A. *Negative refraction at visible frequencies.* Science **316**, 430 (2007).

[19] Dionne, J., Verhagen, E., A.Polman, and Atwater, H. *Are negative index materials achievable with surface plasmon waveguides? a case study of three plasmonic geometries.* Optics Express **16**, 19001 (2008).

[20] Julley, J. V. *Cherenkov Radiation and its Application.* Pergamon, New York, (1958).

[21] Ginzburg, V. L. and Frank, I. M. J. Phys. USSR **9**, 353 (1946).

[22] Goldsmith, P. and Jelley, J. V. *Optical transition radiation from protons entering metal surfaces.* Philos. Mag. **4**, 836 (1959).

[23] Schieber, J., Krinsley, D., and Riciputi, L. *Diagenetic origin of quartz silt in mudstones and implications for silica cycling.* Nature **406**, 981 (2000).

[24] Teng, Y.-Y. and Stern, E. A. *Plasma radiation from metal grating surfaces.* Phys. Rev. Lett. **19**, 511 (1967).

[25] Yamamoto, N., Araya, K., and García de Abajo, F. J. *Photon emission from silver particles induced by a high-energy electron beam.* Phys. Rev. B **64**, Phys. Rev. B (2001).

[26] Vesseur, E., de Waele, R., Kuttge, M., and Polman, A. *Direct observation of plasmonic modes in au nanowires using high-resolution cathodoluminescence spectroscopy.* Nano Lett. **7**, 2843 (2007).

[27] van Wijngaarden, J., Verhagen, E., Polman, A., Ross, C., Lezec, H., and Atwater, H. *Direct imaging of propagation and damping of near-resonance surface plasmon polaritons using cathodoluminescence spectroscopy.* Appl. Phys. Lett. **88**, 221111 (2006).

[28] Bashevoy, M. V., Jonsson, F., Krasavin, A. V., Zheludev, N. I., Chen, Y., and Stockman, M. I. *Generation of traveling surface plasmon waves by free-electron impact.* Nano Lett. **6**, 1113 (2006).

[29] Ter-Mikaelian, M. L. *High-Energy Electromagnetic Processes in Condensed Media.* Wiley, New York, (1972).

[30] Landau, L. D., Lifshitz, E. M., and Pitaevskii, L. P. *Electrodynamics of Continuous Media.* Pergamon Press, (1984).

[31] Jackson, J. D. *Classical Electrodynamics.* Wiley, New York, (1999).

[32] Ford, G. W. and Weber, W. H. *Electromagnetic interactions of molecules with metal surfaces.* Phys. Rep. **113**, 195 (1984).

[33] Cao, J., Gao, Y., Elsayed-Ali, H. E., Miller, R. J. D., and Mantell, D. A. *Femtosecond photoemission study of ultrafast electron dynamics in single-crystal au(111) films.* Phys. Rev. B **58**, 10948 (1998).

[34] Yamamoto, N., Sugiyama, H., and Toda, A. *Cherenkov and transition radiation from thin plate crystals detected in the transmission electron microscope.* Proc. R. Soc. London, Ser. A **452**, 2279 (1996).

[35] Fuchs, R., Barrera, R. G., and Carillo, J. L. *Spectral representations of the electron energy loss in composite media.* Phys. Rev. B. **54**, 12824 (1975).

[36] Lu, J. Q. and Maradudin, A. A. *Channel plasmons.* Phys. Rev. B **42**, 11159 (1990).

[37] Nelayah, J., Kociak, M., Stephan, O., García de Abajo, F. J., Tencé, M., Henrad, L., Taverna, D., Pastoriza-Santos, I., Liz-Marzán, L., and Colliex, C. *Mapping surface plasmons on a single metallic nanoparticle.* Nature Phys. **3**, 348 (2007).

[38] García de Abajo, F. J. and Howie, A. *Relativistic electron energy loss and electron-induced photon emission in inhomogeneous dielectrics.* Phys. Rev. Lett. **80**, 5180 (1998).

[39] García de Abajo, F. J. and Howie, A. *Retarded field calculation of electron energy loss in inhomogeneous dielectrics.* Phys. Rev. B **65**, 115418 (2002).

[40] García de Abajo, F. J. and Kociak, M. *Probing the photonic local density of states with electron energy loss spectroscopy.* Phys. Rev. Lett. **100**, 106804 (2008).

[41] García de Abajo, F. J. *Colloquium: Light scattering by particle and hole arrays.* Rev. Mod. Phys. **79**, 1267 (2007).

[42] García de Abajo, F. J. *to be published.*

[43] Pacifici, D., Lezec, H. J., Atwater, H. A., and Weiner, J. *Quantitative determination of optical transmission through subwavelength slit arrays in ag films: Role of surface wave interference and local coupling between adjacent slits.* Phys. Rev. B **77**, 115411 (2008).

[44] Drexhage, K. H. *Influence of a dielectric interface on fluorescence decay time.* Journ. Lumin. **1**, 693 (1970).

[45] Fussell, D. P., McPhedran, R. C., and de Sterke, C. M. *Three-dimensional green's tensor, local density of states, and spontaneous emission in finite two-dimensional photonic crystals composed of cylinders.* Phys. Rev. E **70**, 066608 (2004).

[46] Blanco, L. A. and García de Abajo, F. J. *Spontaneous light emission in complex nanostructures.* Phys. Rev. B **69**, 205414 (2004).

[47] Schmidlin, E. M. and Simon, H. J. *Observation of long range surface plasmon decay length by optical second harmonic generation.* Appl. Opt. **28**, 3323 (1989).

[48] Bashevoy, M. V., Jonsson, F., MacDonald, K. F., Chen, Y., and Zheludev, N. I. *Hyperspectral imaging of plasmonic nanostructures with nanoscale resolution.* Opt. Express **15**, 11313 (2007).

[49] Puik, E. J., van der Wiel, M. J., Zeijlemaker, H., and Verhoeven, J. *Ion bombardment of thin layers: The effect on the interface roughness and its x-ray reflectivity.* Rev. Sci. Instrum. **63**, 1415 (1992).

[50] Aspnes, D. E., Kinsbron, E., and Bacon, D. D. *Optical properties of au: Sample effects.* Phys. Rev. B **21**, 3290 (1980).

[51] Mills, D. L. *Attenuation of surface polaritons by surface roughness.* Phys. Rev. B **12**, 4036 (1975).

[52] Dawson, P., Alexander, K. B., Thompson, J. R., Haas, J. W., and Ferell, T. L. *Influence of metal grain size on surface-enhanced raman scattering.* Phys. Rev. B **44**, 6372 (1991).

[53] Krishan, V. and Ritchie, R. H. *Anomalous damping of volume plasmons in polycrystalline metals.* Phys. Rev. Lett. **24**, 1117 (1970).

[54] Krenn, J., Ditlbacher, H., Schider, G., Hohenau, A., Leitner, A., and Aussenegg, F. *Surface plasmon micro-and nano-optics.* J. Microsc. **209**, 167 (2003).

[55] Drezet, A., Stepanov, A., Ditlbacher, H., Hohenau, A., Steinberger, B., Aussenegg, F., Leitner, A., and Krenn, J. *Surface plasmon propagation in an elliptical corral.* Appl. Phys. Lett. **86**, 074104 (2005).

[56] Weeber, J.-C., Bouhelier, A., des Francs, G. C., Markey, L., and Dereux, A. *Submicrometer in-plane integrated surface plasmon cavities.* Nano Lett. **7**, 1352 (2007).

[57] Kuzmin, N. V., Alkemade, P. F., 't Hooft, G. W., , and Eliel, E. R. *Bouncing surface plasmons.* Opt. Expr. **15**, 13757 (2007).

[58] Malinowski, E. R. *Factor Analysis in Chemistry.* Wiley, New York, (1991).

[59] Kuttge, M. *to be published.*

[60] Weeber, J.-C., Lacroute, Y., Dereux, A., Devaux, E., Ebbesen, T., Girard, C., Gonzlez, M. U., and Baudrion, A.-L. *Near-field characterization of bragg mirrors engraved in surface plasmon waveguides.* Phys. Rev. B **70**, 235406 (2004).

[61] Gonzalez, M. U., Weeber, J.-C., Baudrion, A.-L., Dereux, A., Stepanov, A. L., Krenn, J. R., Devaux, E., and Ebbesen, T. W. *Design, near-field characterization, and modeling of 45 surface-plasmon bragg mirrors.* Phys. Rev. B **73**, 155416 (2006).

[62] Sanchez-Gil, J. A. and Maradudin, A. A. *Surface-plasmon polariton scattering from a finite array of nanogrooves/ridges: Efficient mirrors.* Appl. Phys. Lett. **86**, 251106 (2005).

[63] Kretschmann, M. and Maradudin, A. A. *Band structures of two-dimensional surface-plasmon polaritonic crystals.* Phys. Rev. B **66**, 245408 (2002).

[64] Pincemin, F. and Greffet, J.-J. *Propagation and localization of a surface plasmon polariton on a finite grating.* J. Opt. Soc. B' **13**, 1499 (1996).

[65] Nikitin, A. Y., Lopez-Tejeira, F., and Martin-Moreno, L. *Scattering of surface plasmon polaritons by one-dimensional inhomogeneities.* Phys. Rev. B **75**, 035129 (2007).

[66] Tan, W.-C., Preist, T. W., Sambles, J. R., and Wanstall, N. P. *Flat surface-plasmon-polariton bands and resonant optical absorption on short-pitch metal gratings.* Phys. Rev. B **59**, 12661 (1999).

[67] Popov, E. K., Bonod, N., and Enoch, S. *Comparison of plasmon surface waves on shallow and deep metallic 1d and 2d gratings.* Opt. Commun. **15**, 4224 (2007).

[68] Perchec, J. L., Quemerais, P., Barbara, A., and Lopez-Rios, T. *Why metallic surfaces with grooves a few nanometers deep and wide may strongly absorb visible light.* Phys. Rev. Lett. **100**, 066408 (2008).

[69] Palik, E. D. *Handbook of Optical Constants.* Academic Press, (1985).

[70] Vahala, K. *Optical Microcavities.* World Scientific, (2004).

[71] Garcia-Vidal, F. J., Rodrigo, S. G., Martin-Moreno, L., and Bozhevolnyi, S. I. *Channel plasmon-polaritons: modal shape, dispersion, and losses.* Optics Letters **31**, 3447 (2006).

[72] Dionne, J., Sweatlock, L., Atwater, H., and Polman, A. *Planar metal plasmon waveguides: frequency-dependent dispersion, propagation, localization, and loss beyond the free electron model.* Phys. Rev. B **72**, 075405 (2005).

[73] Crommie, M. F., Lutz, C. P., and Eigler, D. M. *Confinement of electrons to quantum corrals on a metal surface.* Science **262**, 218 (1993).

[74] des Francs, G. C., Girard, C., Weeber, J.-C., Chicane, C., David, T., Dereux, A., and Peyrade, D. *Optical analogy to electronic quantum corrals.* Phys. Rev. Lett. **86**, 4950 (2001).

[75] Chicanne, C., David, T., Quidant, R., Weeber, J., Lacroute, Y., Bourillot, E., Dereux, A., des Francs, G. C., and Girard, C. *Imaging the local density of states of optical corrals.* Phys. Rev. Lett. **88**, 097402 (2002).

[76] Dionne, J. A., Lezec, H. J., and Atwater, H. A. *Highly confined photon transport in subwavelength metallic slot waveguides.* Nano Lett. **6**, 1928 (2006).

[77] Verhagen, E., Dionne, J., Kuipers, L., Atwater, H., and Polman, A. *Are negative index materials achievable with surface plasmon waveguides? a case study of three plasmonic geometries.* Nano Lett. **8**, 2925 (2008).

[78] Zhu, Z. and Brown, T. G. *Full-vectorial finite-difference analysis of microstructured optical fibers.* Opt. Express **10**, 853 (2002).

[79] Vahala, K. J. *Optical microcavities.* Nature **424**, 839 (2003).

[80] Cai, W., Sainidou, R., Xu, J., Polman, A., and García de Abajo, F. J. Nano Lett. , in press (2009).

[81] Penn, D. R. *Electron mean-free-path calculations using a model dielectric function.* Phys. Rev. B **35**, 482 (1987).

Summary

Plasmonics is a rapidly growing research field. Initially conceived as a fundamentally interesting topic, attention has increased due to the promises that plasmonics holds for future applications. Telecommunication, biological sensing, optoelectronics and photovoltaics are all topics of great public interest which can benefit from of improvements made by plasmonics. To fulfill those promises a thorough knowledge of plasmon properties is of utmost importance and has to be established by studies of basic plasmon principles.

In this thesis we present studies of the generation and confinement of surface plasmon polaritons (SPPs) on metal surfaces. SPPs are generated using the focused electron beam of a scanning electron microscope (SEM). The resulting emission is detected using a cathodoluminescence (CL) spectroscopy setup. The electron beam acts as SPP point source with circular SPP waves propagating radially in all directions. To confine the SPPs we structure the surface and use grooves as reflectors for SPPs.

In chapter 2 we give an introduction to CL and explain the basic mechanisms behind CL. We show that an electron incident onto a metal surface perturbs the conduction electrons at the surface of the metal due to its external field. The generated polarization charge emits transition radiation and excites SPPs. The emission probabilities for transition radiation and SPPs are derived from Maxwell's equations and are presented in chapter 2. Throughout this thesis we use a boundary-element-method (BEM) to calculate the electromagnetic fields arising from the electron impact. The basic concepts of this method are presented in chapter 2.

In chapter 3, the coherent interaction of transition radiation and SPPs is discussed, which leads to interference in the far-field. We present spatially resolved CL measurements that show oscillations in CL emission with distance from a grating patterned in an otherwise planar gold surface. These oscillations are ascribed to the interference between outcoupled SPPs and transition radiation. We present a detailed theoretical analysis that successfully explains the measured CL signal based upon interference of transition radiation directly generated by electron impact and SPPs launched by the electron and outcoupled by the grating. The measured spectral dependence of

the SPP yield per incoming electron is found to be in good agreement with rigorous electromagnetic calculations. We show that the CL emission is similar to that of a dipole oriented perpendicular to the surface and situated at the point of electron impact. This allows us to establish a solid connection between the CL signal and the photonic local density of states associated to SPPs.

In chapter 4 we present the application of CL measurements to determine the SPP damping. By measuring the decay of the CL intensity on a line scan perpendicular to gratings fabricated into the surface we are able to extract the SPP propagation length. We find that the propagation length for single-crystalline gold is in agreement with calculations based on dielectric constants and propagation lengths up to 80 μm are found. For poly-crystalline films the propagation length is reduced. Scattering of SPPs at grain boundaries is identified as additional loss mechanism. The propagation lengths found for these samples can be fitted using a grain boundary scattering coefficient of $S_G = 0.2\%$.

In chapter 5 we use two parallel grooves structured into a single-crystalline gold surface by focused ion beam milling as SPP Fabry-Perot resonators. SPPs excited between the grooves are reflected and form standing waves. The plasmonic cavity modes are spatially and spectrally resolved using CL measurements. The resonators show a broad spectrum of modes with mode numbers up to $n = 10$. Additionally, we determine the resonator quality factor Q. The observed cavity quality factor Q depends strongly on groove depth and the highest $Q = 21$ was found for groove depth of 100-120 nm for a mode at $\lambda = 690\ nm$. We have explained this behavior with a depth dependent reflectivity of the grooves which is confirmed using finite-difference time domain (FDTD) calculations.

Chapter 6 focuses on understanding the reflection of SPPs from a single groove. FDTD calculations show that the wavelength of maximum reflectivity is strongly correlated to groove depth. The resonances of maximum reflectivity are related to localized groove modes. The groove reflectivity is the result of coupling of the incident plasmon wave to the localized modes, that then reradiate to cause a reflected plasmon wave. Groove reflectivities as high as 29 % are found and may be increased by engineering a critical coupling geometry.

Measurements of SPPs on single-crystalline gold which are confined to rectangular plateaus bounded by grooves are presented in chapter 7. We use CL spectroscopy to image the SPP modes of the plateaus. The observed modes show two-dimensional confinement with pronounced maxima. The positions of high emission depends on wavelength and plateau size. The measurements are reproduced using a two-dimensional image source model for the local density of states.

While the previous chapters concentrated on single-interface SPPs, in chapter 8 we use CL spectroscopy to excite metal-insulator-metal (MIM) plasmons. Similar to chapter 5 we have structured two parallel slits into the MIM stack which act Fabry-Perot resonators for MIM plasmons. CL measurements show that the excited MIM plasmon modes form standing waves in the cavities. From the observed spatial mode pattern we derive the MIM plasmon wavevector which agrees well with expected values from analytical dispersion relation calculations. We also present measurements of disc

resonators bounded by circular slits. The observed MIM plasmon modes are confined to mode volumes as small as $0.58\lambda^3$ in units of plasmon wavelength or $0.04\lambda_0^3$ in terms of the free-space wavelength. By using smaller disks, mode volumes as small as $0.0014\lambda_0^3$ are achievable, smaller than any dielectric cavity. The condition of resonant excitation of MIM plasmons is found to depend strongly on the electron energy due to phase retardation effects resulting from the finite electron velocity.

The results presented in this thesis are of twofold interest. First, we show that in cathodoluminescence imaging spectroscopy an electron beam can be used as a point source of SPPs to study basic SPP properties. Second, by using this technique, we determine the fundamental loss mechanisms of SPPs, the nature of groove reflectors, and study the confinement of SPPs in one-, two-, and three-dimensional plasmonic cavities. Using these results, applications in sensing, nanoscale optical integrated circuits, opto-electronic integration and photovoltaics may be pursued.

Samenvatting

Plasmonica is een snel groeiend vakgebied. Het werd in eerste instantie als interessant beschouwd vanuit fundamenteel oogpunt; het uitzicht op veelbelovende toepassingen leidde daarna tot steeds meer belangstelling. Telecommunicatie, biologische sensoren, opto-elektronica en zonnecellen zijn alle onderwerpen met grote maatschappelijke relevantie waar verbeteringen vanuit plasmonica in het verschiet liggen. Om zulke beloften waar te maken is het van groot belang om de grondbeginselen van plasmonen te bestuderen en te begrijpen.

In dit proefschrift presenteren we een studie van het aanslaan en opsluiten van oppervlakteplasmonpolaritonen (SPP's) op metaaloppervlakken. SPP's worden aangeslagen door middel van de gefocusseerde elektronenbundel van een rasterelektronenmicroscoop (SEM). De lichtemissie die hier het gevolg van is, detecteren we in een kathodeluminescentiespectroscopie-opstelling. De elektronenbundel fungeert hier als een puntbron van SPP's, waarbij cirkelvormige SPP-golven op een metaaloppervlak in radiële richting worden uitgezonden. Om de SPP's op te sluiten bewerken we het oppervlak: groeven worden gebruikt als SPP-reflector.

In hoofdstuk 2 geven we een inleiding op kathodeluminescentie (CL) en een verklaring van de principes die aan deze techniek ten grondslag liggen. We laten zien dat een elektron dat invalt op een metaaloppervlak de vrije elektronen aan het oppervlak verstoort als gevolg van zijn uitwendige veld. De polarisatielading die hierdoor onstaat, zendt overgangsstraling uit en slaat SPP's aan. De emissiewaarschijnlijkheid voor deze overgangsstraling en SPP's wordt afgeleid uit de Maxwellvergelijkingen en word in dit hoofdstuk beschreven. In het gehele proefschrift gebruiken we de grensvlakelementenmethode (BEM) om de elektromagnetische velden die veroorzaakt worden door de inval van een elektron te berekenen. De grondbeginselen van deze methode worden ook in hoofdstuk 2 gepresenteerd.

In hoofdstuk 3 bespreken we de coherente interactie tussen overgangsstraling en SPP's, welke leidt tot interferentie in het verre veld. We laten ruimtelijk opgeloste CL-metingen zien, die oscillaties in de CL-emissie vertonen als functie van de afstand tot een tralie die is aangebracht op een verder vlakke goudfilm. Deze oscillaties worden

toegeschreven aan de interferentie tussen uitgekoppelde SPP's en overgangsstraling. We geven een gedetailleerde theoretische analyse die er het mogelijk maakt het gemeten CL-signaal te verklaren vanuit de interferentie tussen overgangsstraling die direct door de elektronenbundel wordt aangeslagen, en SPP's, die eerst worden aangeslagen en dan door de tralie worden uitgekoppeld. De gemeten spectraal opgeloste SPP-opbrengst per invallend elektron is in goede overeenstemming met elektromagnetische berekeningen. We laten zien dat de CL-emissie vergelijkbaar is met de straling van een dipool loodrecht op het oppervlak, op de plek waar het elektron binnenvalt. Op deze wijze demonstreren we de sterke relatie tussen de uitgezonden CL-straling en de lokale optische toestandsdichtheid als gevolg van SPP's.

In hoofdstuk 4 beschrijven we hoe CL-metingen gebruikt kunnen worden om de mate van demping van SPP's te bepalen. Uit het verval van de CL-intensiteit langs een lijn loodrecht op een tralie vinden we de voortplantingslengte van SPP's. Op monokristallijn goud verkrijgen we een lengte die in overeenstemming is met berekeningen gebaseerd op diëlektrische constanten en vinden waarden tot $80\,\mu$m. Deze voortplantingslengte is korter voor polykristallijn goud. We hebben hier verstrooiing van SPP's aan kristalgrensvlakken geïdentificeerd als extra verliesmechanisme. Uit de voortplantingslengten die voor deze monsters gevonden zijn, vinden we een kristalgrensvlak-verstrooiingscoëfficiënt $S_G = 0.2\%$.

In hoofdstuk 5 gebruiken we twee parallelle groeven die met een gefocusseerde ionenbundel zijn aangebracht in een monokristallijn goud oppervlak, als Fabry-Perot-resonatoren voor SPP's. SPP's die tussen de groeven worden aangeslagen worden gereflecteerd en vormen staande golven. We lossen de plasmonische resonanties van deze trilholte zowel spectraal als ruimtelijk op met CL-metingen. De resonatoren laten een breed spectrum van resonanties zien met orde oplopend tot $n = 10$. Daarnaast bepalen we de kwaliteitsfactor Q. De geobserveerde Q is sterk afhankelijk van de groefdiepte; de hoogste $Q = 21$ werd gevonden voor een diepte van 100 – 200 nm voor een resonantie bij $\lambda = 690$ nm. We verkleeren dit uit als een groefdiepte-afhankelijkheid van de reflectiviteit die bevestigd wordt door numerieke berekeningen van de voortplanting van SPP's bij groeven.

Hoofdstuk 6 concentreert zich op het begrip van reflectie van SPPs aan een enkele groef. Numerieke berekeningen laten zien dat de golflengte waarbij de reflectiviteit maximal is sterk verband houdt met de groefdiepte. De maxima in reflectiviteit brengen we in verband met lokale resonanties in de groef. De reflectiviteit is het resultaat van koppeling van invallende plasmongolven aan lokale resonanties, die op hun beurt weer stralen en zo de plasmongolf reflecteren. Groefreflectiviteiten tot 29% zijn zo gevonden; deze zouden nog vergroot worden kunnen door het construeren van een geometrie met kritische koppeling.

Metingen van SPP's die opgesloten worden op rechthoekige plateaus omgeven door groeven in een monokristallijn goud oppervlak worden gepresenteerd in hoofdstuk 7. We gebruiken CL-spectroscopie om een afbeelding te maken van SPP-resonanties van de plateaus. De waargenomen resonanties laten een tweedimensionale opsluiting zien met uitgesproken maxima in het elektrisch veld. De positie waarbij de grootste CL-emissie optreedt hangt af van de detectiegolflengte en de grootte van het plateau.

Berekeningen met een tweedimensionaal beeldbronmodel voor de lokale toestandsdichtheid reproduceren de metingen.

De voorgaande hoofstukken concentreren zich op SPP's aan een enkel grensvlak; in hoofdstuk 8 gebruiken we CL-spectroscopie voor het aanslaan van metaal-isolator-metaal(MIM)-plasmonen. Analoog aan hoofdstuk 5 hebben we twee parallelle spleten aangebracht in een MIM-lagenstructuur, die fungeren als Fabry-Perot resonator voor MIM-plasmonen. CL-metingen laten zien dat de aangeslagen MIM-plasmonresonanties bestaan uit staande golven in de trilholte. Uit het geobserveerde ruimtelijke patroon van de MIM-plasmonresonanties leiden we de golfvector af, die in goede overeenstemming is met waarden die we verwachten aan de hand van analytische dispersieberekeningen. We laten ook metingen zien aan schijfresonatoren die begrensd worden door rondlopende spleten. De waargenomen MIM-plasmonresonanties zijn opgesloten in volumina tot $0.58\,\lambda^3$ in eenheden van plasmongolflengte, of $0.04\,\lambda_0^3$ in termen van vacuumgolflengte. Door gebruik van een nog kleinere schijf, kunnen volumina van slechts $0.0014\,\lambda_0^3$ bereikt worden, wat kleiner is dan enige diëlektrische trilholte. De voorwaarde voor resonante excitatie van MIM-plasmonen blijkt sterk af te hangen van de energie van het binnenvallend elektron, als gevolg van fasevertragingseffecten door de eindige elektronsnelheid.

De resultaten beschreven in dit proefschrift hebben een tweeledige relevantie. Ten eerste laten we zien dat in afbeeldende kathodeluminescentie-spectroscopie de elektronenbundel gebruikt kan worden als een puntbron voor SPP's om de grondprincipes hiervan te onderzoeken. Ten tweede gebruiken we deze techniek voor het onderzoeken van de fundamentele verliesmechanismen van SPP's, de aard van groefreflectoren en de opsluiting van SPP's in een-, twee- en driedimensionale plasmonische trilholten. Deze resultaten kunnen gebruikt worden voor het realiseren van toepassingen in sensoren, geïntegreerde circuits op de nanoschaal, opto-elektronische integratie en zonnecellen.

About the author

Martin Kuttge was born on October, 27th 1978 in Hamm, Germany. He received his high school degree at the 'Galilei Gymnasium' in Hamm in 1998. After a year of civilian service he started his studies in experimental physics at the 'RWTH Aachen'. In the last year of his studies, he worked for his final diploma project at the 'Institut fuer Halbleitertechnik' under the supervision of Prof. H. Kurz. The scope of this work was the 'Propagation of Surface Plasmon Polaritons on Semiconductor Gratings'. After receiving his diploma degree, he started working as a PhD student in 2005 at the FOM-Institute for Atomic and Molecular Physics (AMOLF) in the 'Photonic Materials Group' under the supervision of Prof. A. Polman. The work in this group is the topic of this thesis.

This thesis is based on the following publications

- *Local density of states, spectrum, and far-field interference of surface plasmon polaritons probed by cathodoluminescence,* M. Kuttge, E. J. R. Vesseur, A. F. Koenderink, H. J. Lezec, H. A. Atwater, F. J. García de Abajo, and A. Polman, Phys. Rev. B. **79**, *in press* (2009). (Chapter 3)
- *Loss mechanisms of surface plasmon polaritons on gold probed by cathodoluminescence imaging spectroscopy,* M. Kuttge, E.J.R. Vesseur, J. Verhoeven, H.J. Lezec, H.A. Atwater, and A. Polman, Appl. Phys. Lett. **93**, 113110 (2008). (Chapter 4)
- *Fabry-Perot resonators for surface plasmon polaritons probed by cathodoluminescence,* M. Kuttge, E. J. R. Vesseur, F. J. García de Abajo, and A. Polman, submitted. (Chapter 5)
- *How grooves reflect and absorb surface plasmon polaritons,* M. Kuttge, F. J. García de Abajo, and A. Polman, in preparation. (Chapter 6)
- *Cathodoluminescence imaging spectroscopy of plasmonic metal-insulator-metal modes,* M. Kuttge, F. J. García de Abajo, and A. Polman, in preparation. (Chapter 8)
- *Surface plasmon in a box,* M. Kuttge, F. J. García de Abajo, and A. Polman, in preparation. (Chapter 7)

Acknowledgments

You don't work on your research on your own for four years: this thesis would not have been possible without the support of several people.

First of all, I would like to thank my supervisor Albert Polman. Thank you for giving me the opportunity to conduct my promotion in your group and for all the advice and guidance that you gave me in the last four years. The discussions at our weekly meetings were always very inspiring and they were the breeding ground to develop many new ideas.

I would like to thank Javier García de Abajo for the successful collaboration that we started two years ago. It was a pleasure to work with you on theory but also to discuss together our experiments.

My colleagues at AMOLF contributed to an enjoyable and inspiring atmosphere over the years.

I would like to thank my current and former office mates Ewold Verhagen, Erwin Kroekenstoel, Rene de Waele, Hans Mertens, Ernst Jan Vesseur, Kylie Catchpole, Femius Koenderink, and Jeroen Kalkman. Thanks also to my other colleagues Rob van Loon, Robb Walters, and Sebastian Bidault with whom I enjoyed discussions over coffee or after work.

The collaboration with the other members of the Center for Nanophotonics was a pleasure as well as a challenge. Although I faced a much more critical audience at the nanophotonics colloquia than at any conference I presented at, I think that this was a great education and I learned a lot from it.

An important part of AMOLF is the great help from the support departments. I would like to thank Hans Zeijlemaker for all the help with the evaporators and FIB and his patience whenever I came with a new problem regarding the SEM or CL. Thanks also go to Chris Retif who gave a lot of advice on all the issues related to the Nanocenter. I would also like to thank the members of the workshop for quick solutions to the mechanical problems, E& I for their support in everything related to

computers or electronics, and the design department for their help in design questions.

I would like to thank my family for their support and their encouragement throughout the years. I had a good time in Amsterdam also because of the friends I met here and with whom I had a lot of fun. Finally, I would like to thank Elena as she supported and endured me through the stressful times. We will now make our next step together.

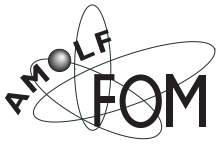

The work described in this thesis was performed at the FOM-Institute for Atomic and Molecular Physics, Kruislaan 407, 1098 SJ Amsterdam, The Netherlands.